

Field Line Resonance in Two and a Half Dimensions

DRAFT VERSION CREATED ON APRIL 11, 2016

1

© Charles A. McEachern 2016

2



3

The text of this work is licensed under a Creative Commons

Attribution-ShareAlike 4.0 International license.

4

⁵ Acknowledgements

⁶ Acknowledgement placeholder.

⁷ MSI.

⁸ Aaron, Scott, Sheng.

⁹ Bob.

¹⁰ John.

¹¹ Lei.

¹² Ian.

¹³ Dedication

¹⁴ Dedication placeholder.

Abstract

¹⁶ Abstract placeholder.

¹⁷ Contents

¹⁸ Acknowledgements	i
¹⁹ Dedication	ii
²⁰ Abstract	iii
²¹ List of Tables	vii
²² List of Figures	viii
²³ 1 Introduction	1
24 1.1 Structure of the Present Work	2
²⁵ 2 The Near-Earth Environment	4
26 2.1 The Outer Magnetosphere	5
27 2.2 The Inner Magnetosphere	7
28 2.3 The Ionosphere	8
29 2.4 Geomagnetic Storms and Substorms	9
³⁰ 3 Field Line Resonance	12
31 3.1 Harmonic Structure	16
32 3.2 Azimuthal Modenumber	18
33 3.3 Poloidal and Toroidal Polarizations	20
34 3.4 Giant Pulsations	22
35 3.5 Motivations for the Present Work	23

36	4 Waves in Cold Resistive Plasma	25
37	4.1 Guided Propagation	27
38	4.2 Compressional Propagation	28
39	4.3 High Altitude Limit	30
40	4.4 Implications to the Present Work	31
41	5 “Tuna Half” Dimensional Model	33
42	5.1 Coordinate System	34
43	5.2 Physical Parameter Profiles	38
44	5.3 Driving	41
45	5.4 Maxwell’s Equations	44
46	5.5 Boundary Conditions	48
47	6 Electron Inertial Effects	53
48	6.1 The Boris Factor	54
49	6.2 Parallel Currents and Electric Fields	56
50	6.3 Inertial Length Scales	61
51	6.4 Discussion	63
52	7 Numerical Results	65
53	7.1 Modenumber and Compression	65
54	7.2 Resonance and Rotation on the Dayside	71
55	7.3 Resonance and Rotation on the Nightside	78
56	7.4 Ground Signatures and Giant Pulsations	82
57	7.5 Discussion	86
58	8 Van Allen Probe Observations	88
59	8.1 Sampling Bias and Event Selection	89
60	8.2 Events by Mode	92
61	8.3 Events by Amplitude	98
62	8.4 Events by Frequency	103
63	8.5 Events by Phase	107
64	8.6 Discussion	112

65	9 Conclusion	113
66	9.1 Summary of Results	113
67	9.2 Future Work	113
68	References	115

⁶⁹ List of Tables

⁷⁰	3.1 IAGA Magnetic Pulsation Frequency Bands	14
⁷¹	5.1 Typical Parameters for the Tuna Density Profile	39
⁷²	5.2 Integrated Atmospheric Conductivity	49

List of Figures

74 2.1	Outer Magnetosphere Cutaway	5
75 2.2	Inner Magnetosphere Cutaway	7
76 3.1	Alfvén Bounce Frequencies	15
77 3.2	First and Second Harmonic Resonances	17
78 3.3	Large and Small Azimuthal Modenumbers	19
79 3.4	Poloidal Mode Structure	21
80 3.5	Toroidal Mode Structure	22
81 4.1	Compressional Alfvén Wave Cutoff Frequencies	32
82 5.1	Nonorthogonal Dipole Grid	38
83 5.2	Alfvén Speed Profiles	40
84 5.3	Ionospheric Conductivity Profiles	41
85 5.4	Decreasing Penetration with Increasing Modenumber	43
86 5.5	Sym-H for June 2013 Storm	44
87 6.1	Plasma Frequency Profile	55
88 6.2	Electric Field Snapshots	57
89 6.3	Current and Poynting Flux at 100 km	58
90 6.4	Current and Poynting Flux at 1000 km	60
91 6.5	Power Density at the Ionosphere	61
92 6.6	Parallel Electric Fields by Perpendicular Grid Resolution	62
93 7.1	Magnetic Field Snapshots from a Small- m Run	68
94 7.2	Magnetic Field Snapshots from a Large- m Run	69
95 7.3	Compressional Coupling to the Poloidal Mode	70
96 7.4	Dayside Poloidal and Toroidal Energy	75

97	7.5 Dayside Poloidal Energy Distribution	76
98	7.6 Dayside Toroidal Energy Distribution	77
99	7.7 Nightside Poloidal and Toroidal Energy	79
100	7.8 Nightside Poloidal Energy Distribution	80
101	7.9 Nightside Toroidal Energy Distribution	81
102	7.10 Dayside Ground Magnetic Fields	84
103	7.11 Nightside Ground Magnetic Fields	85
104	8.1 Distribution of Usable Van Allen Probe Data	90
105	8.2 Rate of Pc4 Events	93
106	8.3 Rate of Pc4 Events by Mode	94
107	8.4 Rate of Double Pc4 Events by Parity and Storm Index	97
108	8.5 Amplitude Distribution of Pc4 Events by Mode	99
109	8.6 Waveforms and Spectra for a Strong Pc4 Event	101
110	8.7 Rate of Pc4 Events by Mode and Amplitude	102
111	8.8 Rate of Pc4 Events by Mode and Frequency	105
112	8.9 Frequency Distribution of Pc4 Events by Mode	106
113	8.10 Waveforms and Spectra for a Pc4 Event	109
114	8.11 Phase Distribution of Pc4 Events by Mode	110
115	8.12 Rate of Pc4 Events by Mode and Phase	111

¹¹⁶ **Chapter 1**

¹¹⁷ **Introduction**

¹¹⁸ 1859 was a pivotal year in human history. The United States moved steadily toward
¹¹⁹ the American Civil War, which would abolish slavery and consolidate the power of
¹²⁰ the federal government. A slew of conflicts in Southern Europe, such as the Austro-
¹²¹ Sardinian War, set the stage for the unification of Italy. The Taiping Civil War — one
¹²² of the bloodiest conflicts of all time — is considered by many to mark the beginning
¹²³ of modern Chinese history. *Origin of Species* was published. The first transatlantic
¹²⁴ telegraph cable was laid.

¹²⁵ Meanwhile, ambivalent to humanity, the Sun belched an intense burst of charged parti-
¹²⁶ cles and magnetic energy directly at Earth. The resulting geomagnetic storm¹ caused
¹²⁷ telegraph systems to fail across the Western hemisphere, electrocuting operators and
¹²⁸ starting fires[36, 99]. Displays of the northern lights were visible as far south as Cuba.

¹²⁹ The Solar Storm of 1859 was perhaps the most powerful in recorded history, but by no
¹³⁰ means was it a one-time event. The Sun discharges hundreds of coronal mass ejections
¹³¹ (CMEs) per year, of all sizes, in all directions. In fact, a comparably large CME narrowly
¹³² missed Earth in 2012[75]. Had it not, it's estimated it would have caused widespread,
¹³³ long-term electrical outages, with a damage toll on the order of 10^{12} dollars[69].

¹The Solar Storm of 1859 is also called the Carrington Event, after English astronomer Richard Carrington. He drew a connection between the storm's geomagnetic activity and the sunspots he had observed the day before.

134 The Sun’s extreme — and temperamental — effect on Earth’s magnetic environment
135 makes a compelling case for the ongoing study of space weather. Such research has
136 evolved over the past century from sunspot counts and compass readings to multi-
137 satellite missions and supercomputer simulations. Modern methods have dramatically
138 increased humanity’s understanding of the relationship between the Sun and the Earth;
139 however, significant uncertainty continues to surround geomagnetic storms, substorms,
140 and the various energy transport mechanisms that make them up.

141 The present work focuses in particular on the phenomenon of field line resonance: Alfvén
142 waves bouncing between the northern and southern hemispheres. Such waves play an
143 important part in the energization of magnetospheric particles, the transport of energy
144 from high to low altitude, and the driving of currents at the top of the atmosphere.

145 **TODO:** More is needed before we can jump into a description of the present work.
146 Introduce what we’re working on a bit ore specifically. Talk about how space is a
147 laboratory that teaches us about plasma in a way that’s relevant to both astrophysics
148 and fusion reactors, which are hard to measure. Fishbone instability.

149 1.1 Structure of the Present Work

150 Chapter 2 surveys the near-Earth environment. Prominent features of the magneto-
151 sphere are defined. The response of the magnetosphere to transient solar wind events
152 is summarized.

153 Chapter 3 introduces the field line resonance phenomenon, in terms of both the under-
154 lying physics and notable work on the topic. Jargon is introduced to clarify important
155 elements of wave structure. Several open questions about field line resonances (FLRs)
156 are offered as motivations for the present work.

157 Chapter 4 lays the groundwork for a numerical model by exploring the fundamental
158 equations of waves in a cold, resistive plasma — such as Earth’s magnetosphere. Char-
159 acteristic scales are gleaned from the resulting dispersion relations.

160 Chapter 5 presents Tuna, a new two and a half dimensional simulation designed specifically
161 for the realistic modeling of FLRs. Tuna’s non-orthogonal geometry, height-resolved ionosphere,
162 novel driving mechanism, and coupling to the atmosphere are explained.
163

164 Chapter 6 considers the addition of electron inertial effects to Tuna, touches on what
165 can be learned from them, and shows that they incur an unreasonable computational
166 cost. (Electron inertia is neglected in the results presented in other chapters.) **TODO:**
167 Previous work has looked at inertial effects for localized models. The exciting part is
168 that we’re looking at a global model.

169 Chapter 7 describes the core numerical results of the work, unifying several of the
170 questions posed in Chapter 3. Significant depth is added to past work on finite poloidal
171 lifetimes[67, 81]. Interplay between poloidal-toroidal coupling, shear-compressional cou-
172 pling, and Joule dissipation is considered from several angles.

173 Chapter 8 puts the numerical results in physical context through the analysis of data
174 from the Van Allen Probes mission. FLR occurrence rates are considered in terms of
175 location, mode structure, and polarization – parameters which have been only partially
176 addressed by other recent FLR surveys[18, 73].

177 Chapter 9 briefly summarizes the results shown in the above chapters — the code
178 development, analysis of numerical results, and satellite observation — and suggests
179 further directions.

¹⁸⁰ **Chapter 2**

¹⁸¹ **The Near-Earth Environment**

¹⁸² From Earth’s surface to a height of a hundred kilometers or so, the atmosphere is a
¹⁸³ well-behaved fluid: a collisional ensemble of neutral atoms. Higher up, its behavior
¹⁸⁴ changes dramatically. As altitude increases, solar ultraviolet radiation becomes more
¹⁸⁵ intense, which ionizes atmospheric atoms and molecules. Density also decreases, slow-
¹⁸⁶ ing collisional recombination. Whereas the neutral atmosphere is held against Earth’s
¹⁸⁷ surface by gravity, the motion of charged particles is dominated by Earth’s geomagnetic
¹⁸⁸ field, as well as the electromagnetic disturbances created as that field is hammered by
¹⁸⁹ the solar wind.

¹⁹⁰ Before discussing specific interactions, it’s appropriate to introduce the so-called “frozen-
¹⁹¹ in condition.” In a collisionless plasma, magnetic field lines are equipotential contours.
¹⁹² Charged particles move freely along the contours, but cannot move across them. Com-
¹⁹³ pression of the magnetic field is synonymous with compression of the ambient plasma,
¹⁹⁴ and any magnetic field lines that thread a moving plasma are dragged along with it.
¹⁹⁵ This assumption is valid throughout most of the magnetosphere — that is, the region of
¹⁹⁶ space primarily governed by Earth’s magnetic field — and provides an invaluable tool
¹⁹⁷ for understanding the large-scale motions of plasmas and fields.

198 **2.1 The Outer Magnetosphere**

199 Plasma behavior within Earth's magnetosphere is ultimately driven by the solar wind:
200 a hot (~ 100 eV), fast-moving (~ 100 km/s) plasma threaded by the interplanetary mag-
201 netic field (~ 10 nT)¹. The density of the solar wind is on the order of 10^6 /cm³; in a
202 laboratory setting, this would constitute an ultra-high vacuum (atmospheric density at
203 sea level is $\sim 10^{19}$ /cm³), but compared to much of the magnetopause it's quite dense.



Figure 2.1: TODO: The outer magnetosphere...

204 The magnetosphere's outer boundary represents a balance between the solar wind dy-
205 namic pressure and the magnetic pressure of Earth's dipole field. On the dayside, the
206 dipole is compressed, pushing this boundary to within about $10 R_E$ of Earth². The
207 nightside magnetosphere is stretched into a long tail which may exceed $50 R_E$ in width
208 and $100 R_E$ in length.

¹Listed values correspond to the solar wind at Earth's orbit.

²Distances in the magnetosphere are typically measured in units of Earth radii: $1 R_E \equiv 6378$ km.

209 When the interplanetary magnetic field opposes the geomagnetic field at the nose of
210 the magnetosphere, magnetic reconnection occurs. Closed magnetospheric field lines
211 “break,” opening up to the interplanetary magnetic field³. They then move tailward
212 across the poles, dragging their frozen-in plasma with them. Reconnection in the tail
213 allows magnetic field lines to convect back to the day side, across the flanks. This
214 process is called the Dungey cycle[23].

Viewed from the north, the Dungey cycle involves a clockwise flow of flux and plasma on
the dusk side and a counterclockwise flow on the dawn side. The motion is accompanied
by a convection electric field, per Ohm’s law in an ideal plasma:

$$\underline{E} + \underline{U} \times \underline{B} = 0 \quad (2.1)$$

215 **TODO: Jets from magnetic reconnection... release of magnetic tension!**

216 Consistent with Ampère’s law, the interplanetary magnetic field is separated from the
217 magnetosphere by a current sheet: the magnetopause. On the dayside, the magne-
218 topause current flows duskward; on the nightside, it flows downward around the mag-
219 netail.

220 Earth’s dipole is significantly deformed in the magnetotail; field lines in the northern
221 lobe of the tail points more or less Earthward, and vice versa. Plasma within the lobes
222 is cool (~ 100 eV) and rarefied ($\sim 10^{-2}$ /cm³). The two lobes are divided by the plasma
223 sheet, which is comparably hot ($\sim 10^3$ eV) and dense (~ 1 /cm³). The plasma sheet
224 carries a duskward current which connects to the magnetopause current.

³Closed field lines are more or less dipolar; one end connects to the north pole of Earth’s magnetic core, and the other end to the south pole. Open field lines are tethered to Earth at one end. In principle, the other end eventually doubles back to Earth, but for practical purposes it is lost to the solar wind. The distinction is important because charged particle motion is guided by magnetic field lines, as discussed in Chapter 3.

225 **2.2 The Inner Magnetosphere**

226 Within about $L \sim 8$ (where L is the McIlwain parameter⁴), the dipole magnetic field
227 is not appreciably deformed by the solar wind. As a result, the structures in the inner
228 magnetosphere follow closely from the motion of charged particles in an ideal dipole
229 field.

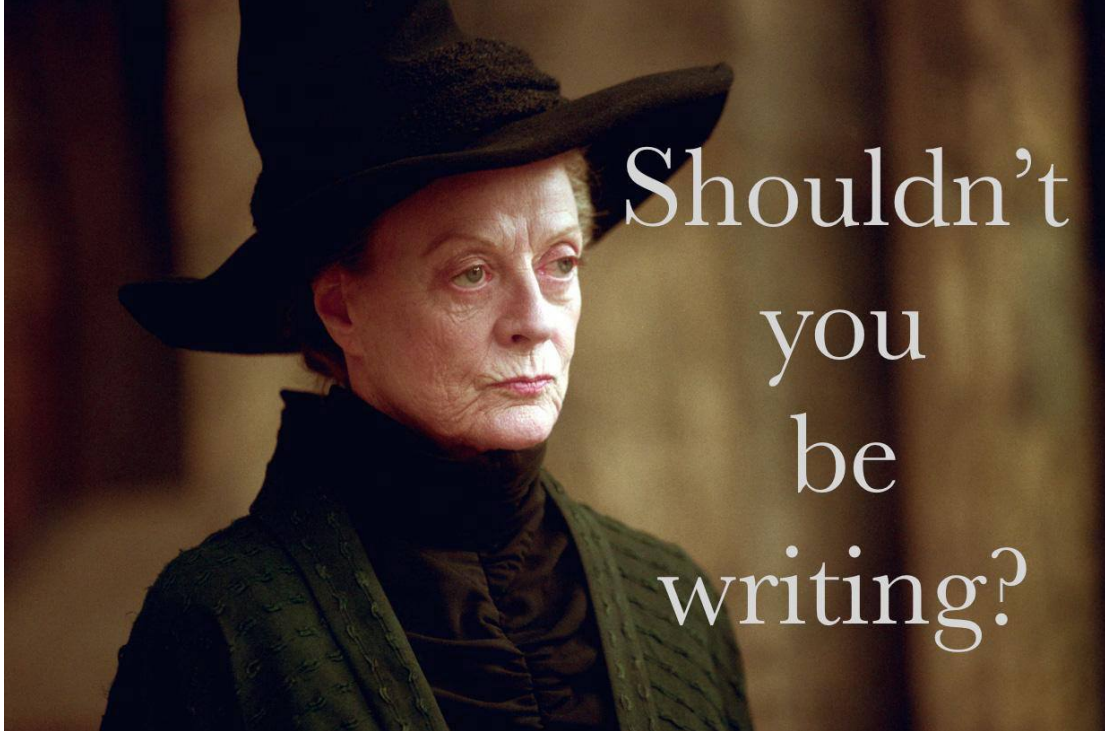


Figure 2.2: TODO: The inner magnetosphere...

230 The plasmasphere — a cold (~ 1 eV), dense ($10^2 / \text{cm}^3$ to $10^4 / \text{cm}^3$) torus of corotating
231 plasma — is formed by the outward drift of atmospheric ions along magnetic closed
232 field lines. Its outer boundary is thought to represent a balance between the corotation
233 electric field (per the rotation of Earth's magnetic dipole) and the convection electric

⁴The McIlwain parameter L is used to index field lines in Earth's dipole geometry: $L \equiv \frac{r}{\sin^2 \theta}$ for colatitude θ and radius r in Earth radii. For example, the $L = 5$ field line passes through the equatorial plane at a geocentric radius of $5 R_E$, then meets the Earth at a colatitude of $\arcsin \sqrt{\frac{1}{5}} \sim 27^\circ$ (equally, a latitude of $\arccos \sqrt{\frac{1}{5}} \sim 63^\circ$).

234 field (associated with the convection of magnetic flux during the Dungey cycle). Particle
235 density drops sharply at the edge of the plasmasphere; the boundary is called the
236 plasmapause. The plasmapause typically falls around $L = 4$, though during prolonged
237 quiet times it can extend to $L = 6$ or larger.

238 Energetic particles trapped within the inner magnetosphere are divided into two popu-
239 lations.

240 The Van Allen radiation belts are made up of particles with energy above 10^5 eV or
241 so. The inner belt ($L \lesssim 2$) is primarily composed of protons, the decay remnants of
242 neutrons freed from the atmosphere by cosmic rays. The outer belt ($L \gtrsim 4$) is primarily
243 composed of high-energy electrons. The density of radiation belt particles is significantly
244 affected by geomagnetic storms and substorms; a typical value is $10 / \text{cm}^3$.

245 Particles with energies of 10^3 eV to 10^5 eV make up the ring current, which extends
246 from $L \sim 3$ to $L \sim 5$. Gradient-curvature drift carries ions and electrons in opposite
247 directions; the net result is a westward current. During quiet times, the ring current
248 causes magnetic a southward magnetic field on the order of 1 nT at Earth's equator,
249 while during geomagnetically active times (discussed in Section 2.4) the effect may
250 100 nT or more⁵.

251 2.3 The Ionosphere

252 Earth's neutral atmosphere is an excellent insulator. Collisions are so frequent that
253 charged particles quickly thermalize and recombine. The breakdown of air molecules
254 into a conductive plasma (as happens during a lightning strike, for example) requires
255 electric fields on the order of 10^9 mV/m.

256 Cold particles in the magnetosphere are likewise not conducive to currents. In the
257 absence of collisions, electrons and ions drift alongside one another in response to an
258 electric field, creating no net current perpendicular to the magnetic field⁶.

⁵For comparison, Earth's dipole field points north at the equator with a magnitude over 10^4 nT.

⁶The so-called E -cross- B drift is associated with a velocity of $\underline{U} = \frac{1}{B^2} \underline{E} \times \underline{B}$, independent of a charged particle's mass or sign.

259 The ionosphere is a sweet spot between the two regimes. Collisions are frequent enough
260 to disrupt the drift of ions, but not frequent enough to immobilize the electrons. The
261 result is nonzero Pedersen and Hall conductivity, corresponding to current along the
262 electric field and in the $\underline{B} \times \underline{E}$ direction respectively. It is these currents — particularly
263 the Hall current — which give rise to magnetic fields at the ground. Collisions in the
264 ionosphere also give rise to a finite parallel conductivity, allowing for the formation of
265 potential structures along the magnetic field line.

266 The convection electric field (associated with the Dungey cycle, Section 2.1) drives
267 Pedersen currents in the ionosphere. Pedersen currents flow downward on the flanks
268 and duskward across the poles. The currents remain divergence-free by connecting
269 to field-aligned currents at the edges of the polar cap. The field-aligned currents, in
270 turn, connect to the magnetopause current, the cross-tail current, and the (partial) ring
271 current.

272 When electron density is low, thermal velocities may be unable to carry enough current
273 to satisfy $\nabla \cdot \underline{J} = 0$. This leads to the formation of potential structures along geomagnetic
274 field lines in the ionosphere. Such structures accelerate particles along magnetic field
275 lines, leading to the precipitation of energetic particles into the atmosphere. As the
276 particles thermalize, they excite atmospheric atoms. The resulting spontaneous emission
277 is often in the visible spectrum, giving rise to the aurora.

278 2.4 Geomagnetic Storms and Substorms

279 The quiet geomagnetic behavior described above is periodically disturbed by transient
280 solar phenomena such as corotating interaction regions (CIRs) and coronal mass ejections
281 (CMEs). CMEs, as noted in Chapter 1, are bursts of unusually dense solar wind
282 which are ejected from regions of high magnetic activity on the Sun; they are most
283 common at the height of the eleven-year solar cycle. CIRs, on the other hand, occur
284 when a relatively fast region of the solar wind catches up to an earlier and slower-moving
285 pocket of solar wind, resulting in a pair of shockwaves.

286 During a storm, increased solar wind intensity results in enhanced magnetic reconnection
287 on the dayside. As the newly-opened field lines are swept tailward, the convection
288 electric field is strengthened. The plasmasphere — the outer boundary of which is
289 set by a balance between the convection electric field and the (more or less constant)
290 corotation electric field — sheds its outer layers. A large number of energetic particles
291 are also injected into the ring current[71].

292 The strength of the storm is gauged by the size of the magnetic perturbation created
293 by the ring current⁷. A small storm has a magnitude of 50 nT to 100 nT. Large storms
294 may reach 250 nT to 500 nT. The Carrington Event, mentioned in Chapter 1, is thought
295 to have exceeded 1700 nT[99].

296 The main phase of a storm typically lasts for several hours. Storm recovery — the
297 gradual return of the storm index to zero, and the refilling of the plasmasphere —
298 typically lasts several days. Geomagnetic storms occur tens of times per year at the
299 height of the solar cycle, and just a few times per year otherwise.

300 Whereas storms are prompted by large solar wind events on the dayside, geomagnetic
301 substorms are primarily a nightside occurrence. As flux accumulates in the tail, mag-
302 netic tension builds in the stretched field lines. A substorm is an impulsive release of
303 that tension.

304 **TODO: Phases of a substorm. Definition of a substorm comes from [1]. Revised by [72].**

305

306 At substorm onset, a burst of reconnection occurs in the tail. A jet of plasma is launched
307 Earthward from the reconnection site (and another is launched tailward, and lost to the
308 solar wind). The Earthward plasma injection injects particles into the ring current.
309 The outer radiation belt is depleted, then repopulated. Energetic particles precipitate
310 into the atmosphere, giving rise to a distinctive sequence of auroral signatures over the
311 course of about an hour.

⁷The most commonly used storm index is DST, which is computed hourly using measurements from several ground magnetometers near the equator. The Sym-H index, used in Section 5.3, is computed once per minute.

- 312 Concurrent with substorm onset, impulsive Alfvén waves are observed with periods of
313 a minute or two. The precise ordering of events — whether reconnection causes the
314 waves, or vice versa, or if they share a common cause — remains controversial.
- 315 Each substorm lasts several hours, including the time it takes for the ring current to
316 return to pre-substorm levels. Several substorms may occur per day during quiet times.
317 During a storm, substorms become far more frequent; by the time one has ended,
318 another may have already begun.

³¹⁹ **Chapter 3**

³²⁰ **Field Line Resonance**

- ³²¹ The motion of a charged particle in a dipole field can be described in terms of three
³²² fundamental motions. The first is cyclotron motion. Given a uniform magnetic field
³²³ line, a particle follows a helical path. It moves in a circular path in a plane normal to
³²⁴ the magnetic field line, and keeps a constant velocity along the direction of the field.
- ³²⁵ The second fundamental motion is bounce motion. As it moves along the magnetic field
³²⁶ line like a bead on a wire, the particle experiences a change in magnetic field magnitude.
³²⁷ In order to conserve its magnetic moment (also called the first adiabatic invariant), the
³²⁸ particle's perpendicular kinetic energy increases in proportion with the magnetic field.
³²⁹ When the perpendicular kinetic energy can no longer increase — that is, when all of the
³³⁰ particle's kinetic energy is perpendicular — the particle bounces back. (If the particle's
³³¹ parallel kinetic energy is sufficiently large, it doesn't bounce, and instead precipitates
³³² into the atmosphere.) Particles undergoing bounce motion continuously move back and
³³³ forth between the northern and southern hemispheres.
- ³³⁴ The third fundamental motion is drift motion. Over the course of a particle's cyclotron
³³⁵ motion, the Earthward half of the orbit experiences a slightly stronger magnetic field
³³⁶ (and thus a slightly smaller orbit radius). The net effect, called the gradient-curvature
³³⁷ drift, is an azimuthal motion around Earth.

338 Characteristic timescales for each of the above motions depend on particle energy. Elec-
339 tron cyclotron motion is on the order of **TODO: ...** in the ionosphere, and closer to
340 **TODO: ...** in the tail; ions gyrate slower by three orders of magnitude due to their
341 larger mass. **TODO: Bounce... Drift...**

342 Wave-particle resonance arises when a particle's periodic motion matches with the fre-
343 quency of a coincident electromagnetic wave[25, 66, 77, 88]. In the particle's rest frame,
344 the wave then appears as a net electric field. This allows a net movement of energy
345 between the wave and the particle. The interaction is analogous to a surfer moving
346 along with — and being accelerated by — a wave in the ocean. Such resonance can
347 arise for any of the three fundamental motions, or even for a combination of them.

348 In the present work, the waves in question are field line resonances (FLRs). An FLR
349 is a standing harmonic on a geomagnetic field line. It can also be envisioned as a
350 superposition of traveling waves, reflecting back and forth between its northern and
351 southern foot points at the conducting ionosphere.

These waves travel at the Alfvén speed, v_A , defined per

$$v_A^2 \equiv \frac{B^2}{\mu_0 \rho} \quad \text{or, equally,} \quad v_A^2 \equiv \frac{1}{\mu_0 \epsilon_{\perp}} \quad (3.1)$$

352 Where B is the magnetic field magnitude, ρ is the mass density, and μ_0 is the magnetic
353 constant. The perpendicular electric constant ϵ_{\perp} is analogous to the electric constant
354 ϵ_0 , and arises in cases (such as the magnetosphere) where a dielectric medium exhibits
355 a preferred direction. In the magnetosphere, mass density and magnetic field strength
356 depend strongly on position. As a result, the Alfvén speed may vary by several orders
357 of magnitude over the length of a field line.

358 The fundamental equations of field line resonance were presented by Dungey in 1954[22];
359 since then, they have remained a topic of active study.

360 **TODO: ...in no small part because they are not just relevant to space!** Alfvén waves
361 also show up in laboratory plasmas, which are hard to measure directly, and in all sorts
362 of astrophysical contexts.

363 So-called ultra low frequency waves — of which FLRs are a subset — are categorized
 364 by morphology. Continuous (long-lived) pulsations are termed Pc, while irregular pul-
 365 sations are called Pi. Within each are a number of frequency bands; see Table 3.1[46].

Table 3.1: IAGA Magnetic Pulsation Frequency Bands

	Pc1	Pc2	Pc3	Pc4	Pc5	Pi1	Pi2
Period (s)	0.2–5	5–10	10–45	45–150	150–600	1–40	40–150
Frequency (mHz)	200–5000	100–200	22–100	7–22	2–7	25–1000	7–25

366 TODO: Boundaries between wave bands are, in practice, not strict. They are sometimes
 367 fudged to better match phenomenological boundaries.

368 FLRs fall into the Pc3, Pc4, and Pc5 ranges. The present work focuses specifically
 369 on the Pc4 band: waves with periods of a minute or two. Frequencies in the Pc4
 370 range typically coincide with Alfvén bounce times¹ near the plasmapause: $L \sim 4$ to
 371 $L \sim 6$ [3, 18, 26, 58]². In fact, the large radial gradients in the Alfvén speed near the
 372 plasmapause act as an effective potential well, trapping FLRs[17, 51, 55, 56, 65, 91].

373 In addition to being radially localized, FLRs in the Pc4 frequency band (also called Pc4
 374 pulsations, or just Pc4s) are localized in magnetic local time (MLT³). They have also
 375 been shown to occur preferentially on the dayside, during storms or storm recovery[3,
 376 18, 26, 54, 58, 100].

377 In the inner magnetosphere, the Alfvén frequency — and thus the frequency of FLRs
 378 — often coincides with integer or half-integer⁴ multiples of particle drift frequencies[19].
 379 The resulting wave-particle interactions can give rise to significant energization and
 380 radial diffusion of the particles. In some cases, the waves also include an electric field

¹The Alfvén frequency is the inverse of the Alfvén bounce time: $\frac{2\pi}{\omega_A} \equiv \oint \frac{dz}{v_A}$.

²Not coincidentally, these are the same L -shells where the Van Allen Probes spend most of their time; see Chapter 8.

³Noon points toward the Sun and midnight away from it, with 06:00 and 18:00 at the respective dawn and dusk flanks.

⁴See Section 3.1.

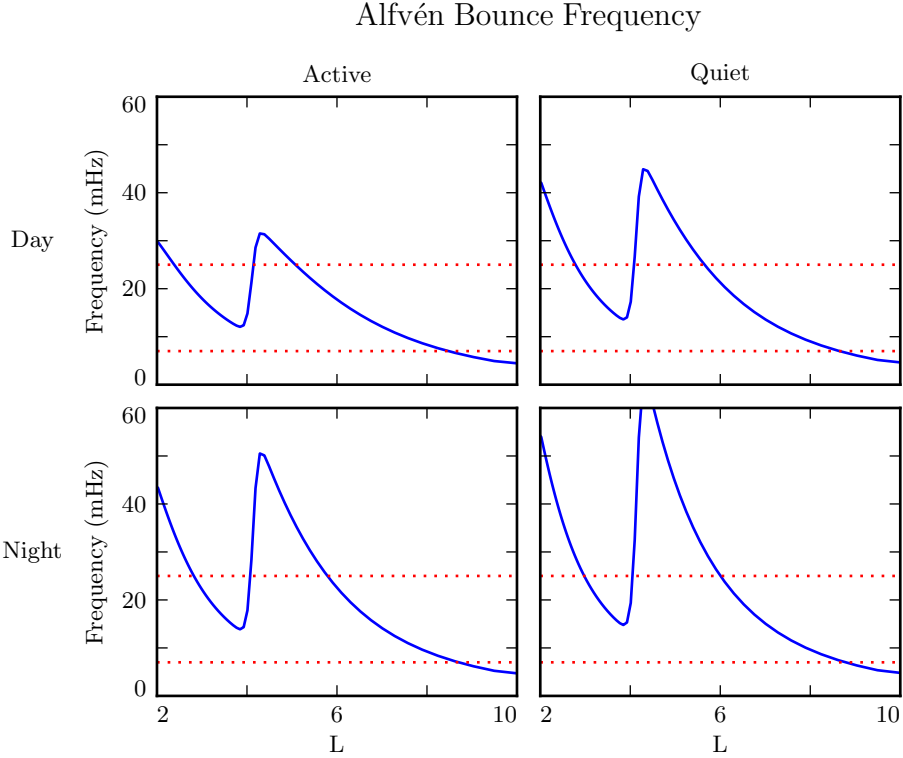


Figure 3.1: The above are bounce frequencies for an Alfvén wave moving back and forth along a geomagnetic field line. Alfvén speeds are computed based on profiles from Kelley[49], as discussed in Section 5.2. Notably, the bounce frequency depends significantly on the position of the plasmasphere, taken here to be at $L = 4$. Dotted lines indicate the Pc4 frequency range: 7 mHz to 25 mHz.

381 parallel to the background magnetic field, contributing to the precipitation of energetic
 382 particles into the neutral atmosphere[33, 34, 97, 107].

383 The present chapter introduces the structural characteristics of FLRs, how those charac-
 384 teristics affect wave behavior, and several unresolved questions related to that behavior.

385 **TODO:** The polarization of long-period Alfvén waves is rotated by $\sim 90^\circ$ when passing
 386 through the ionosphere[42]. A wave that is azimuthally polarized in space is polarized
 387 north-south on the ground, and vice versa. It has been noted specifically that Pgs
 388 exhibit east-west polarized ground signatures[96].

389 **3.1 Harmonic Structure**

390 Wave structure along a geomagnetic field line is indicated by harmonic number. The
391 first (or fundamental) harmonic has a wavelength twice as long as the field line. The
392 electric field perturbation is zero at the ionospheric foot points of the field line, due
393 to the conductivity of the ionosphere. For the first harmonic, this puts an electric
394 field antinode at the equator, along with a node in the perpendicular⁵ perturbation
395 to the magnetic field. For the second harmonic, the electric field has a third node at
396 the equator, which is accompanied by an antinode in the perpendicular magnetic field
397 perturbation. Figure 3.2 shows a qualitative sketch of the first and second harmonics:
398 a series of snapshots in time, in the rest frame of the wave. Perpendicular electric and
399 magnetic field perturbations are shown in blue and red respectively.

400 A first-harmonic FLR that is periodic or localized in the azimuthal direction is conducive
401 to drift-resonant wave-particle interactions[19, 78]. The particle is like a child on a swing:
402 whenever the path of the particle (or child) gets close to the wave (parent), it gets a
403 push, and always in the same direction. The wave fields spend half its time pointing
404 the other direction, just as the parent must shift their weight backward to get ready for
405 the next push, but at that point the particle (child) is far away.

406 Second-harmonic FLRs interact with particles through the drift-bounce resonance, which
407 is slightly more complicated. As the particle drifts azimuthally, it also zig-zags north-
408 south. The combination of those two periodic motions must align with the phase of
409 the wave electric field. An example path is shown by the purple line in Figure 3.2: the
410 particle experiences a rightward electric field throughout the wave's oscillation.

The drift and drift-bounce resonance conditions is written, respectively[92]:

$$\omega - m\omega_D = 0 \quad \text{and} \quad \omega - m\omega_D = \omega_B \quad (3.2)$$

⁵The parallel, or compressional, magnetic field exhibits the same nodes and antinodes as the perpendicular electric field[81].

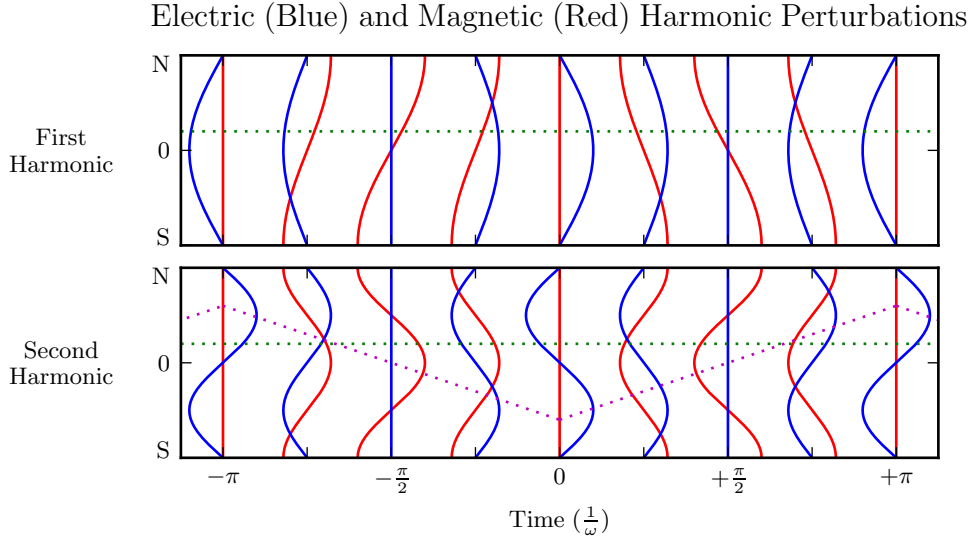


Figure 3.2: The first (or fundamental) harmonic has an antinode in its perpendicular electric field (blue) at the equator, along with a node in its perpendicular magnetic field perturbation (red). A single satellite can identify the first harmonic by the relative phase of the electric and magnetic field perturbations: an observer north of the equator (green) will see the magnetic field perturbation lead the electric field by $\pm 90^\circ$. The second harmonic is the opposite: it has an electric field node at the equator, and an observer north of the equator will see the magnetic field perturbation lag the electric field by $\mp 90^\circ$. Top and bottom signs correspond to the poloidal (shown) and toroidal polarizations respectively. The purple line sketches the path of a particle in drift-bounce resonance; in the particle’s rest frame, the electric field is always to the right.

- 411 Where ω is the frequency of the wave, ω_D and ω_B are the particle’s drift and bounce
- 412 frequencies respectively, and m is the wave’s azimuthal modenumber, as discussed in
- 413 Section 3.2.
- 414 In principle, the first and second harmonics can be distinguished by their frequencies,
- 415 even from a single-point observation[16, 35]. In practice, however, this is not a reliable
- 416 approach[93]. There are significant uncertainties surrounding the mass density profile
- 417 — and thus the Alfvén speed profile — along a geomagnetic field line.
- 418 Harmonic structure can also be deduced by noting the phase offset between the wave
- 419 magnetic field and its electric field (or the plasma velocity)[18, 96]. In Figure 3.2, the
- 420 green line indicates an observer just north of the magnetic equator. For a wave polarized

421 in the poloidal direction (see Section 3.3), the observer sees the electric field waveform
422 offset from the magnetic field by a phase of $\pm 90^\circ$, where the top sign is for odd modes
423 and the bottom sign is for even modes. The signs are flipped for toroidally-polarized
424 waves, and again for waves observed south of the equator.

425 **TODO:** Talk about imaginary Poynting flux? Standing waves don't move energy. Traveling waves do. In practice, everything is a superposition of the two.

427 Notably, the measurement of wave phase has only become viable with the advent of
428 satellites carrying both electric and magnetic field instrumentation, such as THEMIS
429 in 2007[4] and the Van Allen Probes⁶ in 2012[89].

430 Strictly speaking, the the phase offset of the electric and magnetic fields does not provide
431 the harmonic number — only its parity. It's reasonably safe to assume that an even mode
432 is the second harmonic; the second harmonic is by far the most commonly observed[45,
433 86, 94], due in part to its excitement by the antisymmetric balloon instability[10, 12,
434 14, 88]. However, the distinction between the first and third harmonics is not always
435 clear[15, 35]; this issue is discussed further in Chapter 8. Higher harmonics than that
436 are not expected in the Pc4 frequency band.

437 **TODO:** Second-harmonic FLRs are unlikely to cause ground signatures[96].

438 3.2 Azimuthal Modenumber

439 The wavelength of an FLR in the azimuthal direction is indicated by its azimuthal
440 modenumber. A wave with modenumber m has an azimuthal wavelength that spans $\frac{24}{m}$
441 hours in MLT.

442 Waves with small azimuthal modenumbers ($0 < m < 10$) are typically driven by broad-
443 band energy sources at the magnetosphere's boundary, such as variations in the so-
444 lar wind pressure[20, 39, 50, 110, 111], sporadic magnetic reconnection[43], or Kelvin-
445 Helmholtz waves on the magnetopause[11, 59, 87]. In the low- m regime, the shear and
446 compressional Alfvén waves are coupled, which allows energy to move across field lines

⁶The Van Allen Probes were previously called RBSP, for Radiation Belt Storm Probes.

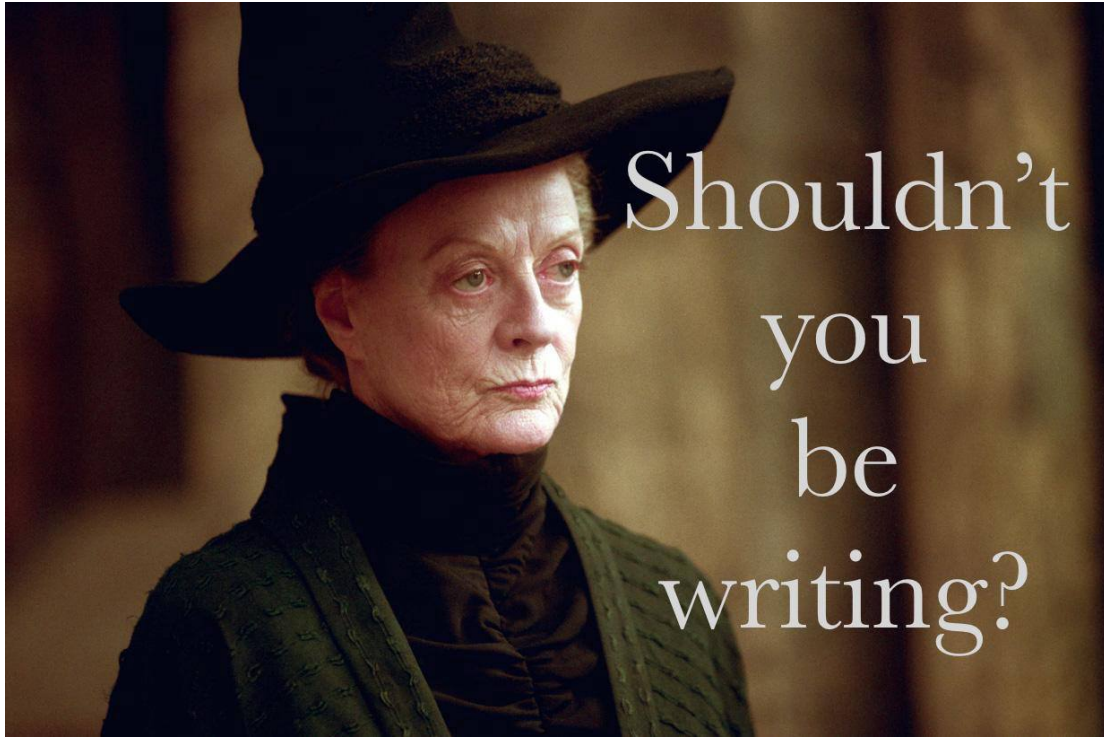


Figure 3.3: TODO: Large and small azimuthal modenumber.

447 until the driving frequency lines up with the local Alfvén frequency[61]. Because of their
448 broadband energy source, low- m FLRs often have a mishmash of frequencies present in
449 their spectra[18], though the spectra are coherent in terms of harmonic[27].

450 When the azimuthal modenumber is large (or, equally, when the azimuthal wavelength
451 is small), compressional propagation of Alfvén waves becomes evanescent, so the move-
452 ment of energy is guided by magnetic field lines[16, 81]⁷. As a result, FLRs must be
453 driven from within the magnetosphere. Proposed energy sources include phase space
454 gradients near the plasmapause[19], particularly as the plasmasphere refills after a storm
455 or substorm[26, 57].

456 The atmosphere is known to attenuate waves with small spatial extent in the perpendic-
457 ular direction[44, 105, 109]. As a result, FLRs may create no signature on the ground if

⁷Equally, the strength of a wave's parallel component hint at its modenumber, a point which is revisited in Chapter 8.

458 their azimuthal modenumber is large. For example, a recent paper by Takahashi shows
459 a strong (2 nT at $L \sim 10$), clear resonance with $|m| \gtrsim 70$ and no corresponding ground
460 signature[93].

Southwood[88] and Glassmeier[31] show that a low frequency wave passing through the ionosphere on its way to Earth will be attenuated per

$$\frac{B_E}{B_I} = \frac{\Sigma_H}{\Sigma_P} \exp\left(-m \frac{R_I - R_E}{R_E \sin \theta}\right) \quad (3.3)$$

461 Where B_E and B_I are the magnetic field strengths at R_E (Earth's surface, 6783 km
462 geocentric) and R_I (the ionosphere, $\sim 6900 \text{ km}$ geocentric) respectively. The integrated
463 ionospheric Pedersen and Hall conductivities, Σ_P and Σ_H , are typically within a factor
464 of two of one another. Field lines near the plasmapause can be traced to Earth at
465 $\sin \theta \sim 0.4$. That is, by the time it reaches the ground, the magnetic field from an FLR
466 with $m = 10$ is weaker by a factor of two; at $m = 100$, the factor is closer to 100.

467 3.3 Poloidal and Toroidal Polarizations

468 Based on polarization, each FLR can be classified as either poloidal or toroidal. The
469 poloidal mode is a field line displacement in the meridional plane, as shown in Figure 3.4,
470 with an accompanying electric field in the azimuthal direction. The toroidal mode's
471 magnetic displacement is azimuthal, per Figure 3.5; the associated electric field is in the
472 meridional plane.

473 Both poloidal and toroidal waves are noted for their ability to contribute to the energiza-
474 tion and radial diffusion of trapped particles. The poloidal mode interacts more strongly,
475 since its electric field is aligned with the trapped particles' drift motion. Poloidally-
476 polarized waves are also more prone to creating magnetic signatures on the ground, due
477 to ducting in the ionosphere[29, 37].

478 Toroidal modes have been shown to far outnumber poloidal modes[3]. Perhaps not
479 coincidentally, poloidally-polarized waves rotate asymptotically to the toroidal mode[67,
480 68, 81]. Poloidal waves with low azimuthal modenumber — such as those driven by

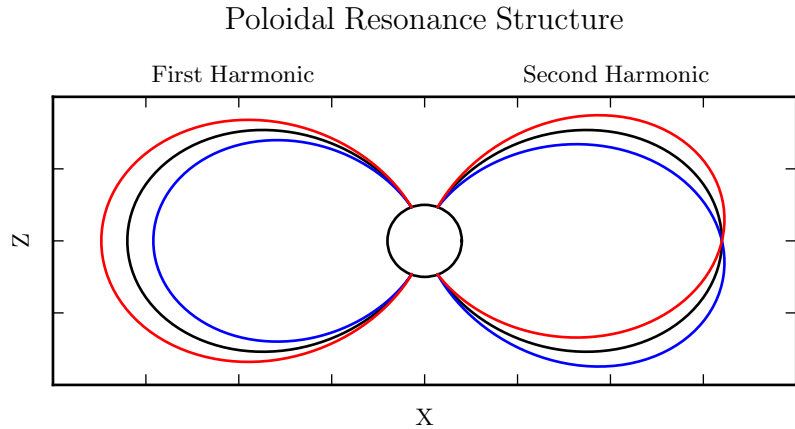


Figure 3.4: The poloidal resonance is a magnetic field in the meridional plane. The displacement is radial near the equator, and can be accompanied by enhancement in the parallel magnetic field near the ionosphere. The first harmonic is shown on the left, and the second harmonic on the right. Lines are colored red and blue only to contrast with the unperturbed black field line.

481 broadband sources at the magnetopause — rotate on timescales comparable to their
 482 oscillation periods.

483 **TODO:** Fishbone instability[13, 70]. Like the poloidal mode, but for lab plasmas.

484 **TODO:** Poloidal and toroidal modes are coupled by the ionospheric Hall conductivity[48].
 485 The Hall conductivity also increases the “ringtime” of these resonances, allowing them
 486 to oscillate through the inductive process rather than be dissipated as Joule heating[103].

487

488 **TODO:** Toroidal modes show a clear frequency dependence with L . Poloidal modes less
 489 so. Citation... [27]?

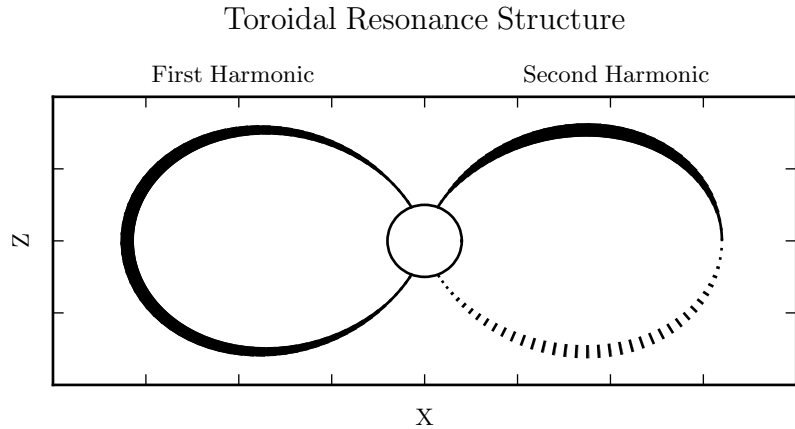


Figure 3.5: A toroidally-polarized FLR has a magnetic perturbation in the azimuthal direction, as shown. Bold lines are taken to be above the page, and dotted lines below the page, with the displacement indicated by the line’s width. The first harmonic — where the entire field line oscillates in and out of the page — is shown on the left. The second harmonic is on the right, with northern and southern halves perturbed in opposite directions.

490 3.4 Giant Pulsations

491 The study of geomagnetic pulsations long predates satellites, sounding rockets, or even
 492 the word “magnetohydrodynamics”⁸. Large, regular oscillations in the magnetic field
 493 were noted as early as 1901[6]. Eventually, the term “giant pulsation,” or Pg, arose to
 494 describe such pulsations.

495 On the ground, Pgs are notable for their strikingly sinusoidal waveforms, their eastward
 496 drifts, and their specific occurrence pattern: Pgs are typically seen pre-dawn, at latitudes
 497 of 60° to 70° . Pgs generally fall into the Pc4 frequency band⁹. Their harmonic structure
 498 was a source of controversy for decades, but recent multisatellite observations seem to be
 499 in agreement that they are odd harmonics, probably fundamental[32, 41, 53, 54, 92, 96].
 500 They are poloidally polarized, with modenumbers $10 \lesssim m \lesssim 40$ [30, 41, 78, 84, 96].

⁸The term was first used by Alfvén in the 1940s[2].

⁹The Pc4 range is periods of 45 s to 140 s, while Pgs are often said to range from 60 s to 200 s[8].

501 Whereas FLRs are waves in space which may produce ground signatures, “giant pulsation” refers to the ground signature specifically¹⁰. That is, Takahashi’s satellite observation of a sinusoidal, morningside, high- m , fundamental poloidal resonance was not
502
503
504 classified as a Pg because it did not produce a signal on the ground[93].

505 **TODO:** Pgs are localized to within 2° to 5° in latitude[73, 92, 101].

506 Due to their remarkably clear waveforms, Pgs are typically found by “visual inspection
507 of magnetometer data”[73]. Over the course of the past century, a number of multi-year
508 (sometimes multi-decade[8]) surveys have totaled nearly one thousand Pg events. On
509 average, a ground magnetometer near 66° magnetic latitude observes \sim 10 Pg events per
510 year[8, 40, 83, 90]. Observations are not distributed uniformly; rather, giant pulsations
511 become more common near the equinox and during times of low solar activity.

512 Unlike Pc4 pulsations in general, Pgs show no particular correlation with storm phase[73].
513 However, they do often occur as the magnetosphere recovers from a substorn[73, 84].

514 3.5 Motivations for the Present Work

515 A great deal has been learned — and continues to be learned — through observations of
516 field line resonance. However, the cost-to-benefit ratio is climbing. As summarized in the
517 sections above, FLR behavior depends significantly on harmonic structure, azimuthal
518 modenumber, and polarization — not to mention frequency, spectral width, and so
519 on. With each degree of freedom comes the necessity for an additional simultaneous
520 observation.

521 Similarly, as FLRs have been shown to depend on ever-more-specific magnetospheric
522 conditions, analytical techniques have fallen out of favor. The height-resolved iono-
523 sphere, the multidimensional Alfvén speed profile, and the inconvenient geometry com-
524 bine to create a problem beyond the reasonable purview of pencil and paper.

525 That is, the topic of field line resonance is ripe for numerical modeling.

¹⁰Historically, the wave designations shown in Table 3.1 all referred to ground phenomena. Over time, they have come to describe satellite observations as well, including those without corresponding signatures on the ground.

526 Past models of the magnetosphere have been limited in their consideration of FLRs.
527 Reasons include overly-simplified treatment of the ionospheric boundary, no consider-
528 ation of the plasmapause, limited range in m , and the inability to compute ground
529 signatures. Chapter 5 presents a model which addresses these issues, allowing the com-
530 putation of field line resonance with unparalleled attention to realism.

531 The model allows a bird's-eye view of the structure and evolution of FLRs. As such,
532 not only can several open questions be addressed, but their answers serve to unify a
533 number of seemingly-disparate properties described in the sections above.

534 The rotation of poloidally-polarized waves to the toroidal mode is investigated. Par-
535 ticular attention is paid to the importance of azimuthal modenumber and ionospheric
536 conductivity. The interplay between said rotation and the transport of energy across
537 field lines — which also depends on azimuthal modenumber — is considered as well.

538 By their nature, drifting particles have the potential to spur wave-particle interactions
539 at all MLT. However, Pc4 observations are strongly peaked on the dayside. In a 2015
540 paper, Dai notes, “It is not clear why noncompressional [high- m] Pc4 poloidal waves,
541 which are presumably driven by instability within the magnetosphere, preferentially
542 occur on the dayside”[18]. Motoba, later that year, echoes, “It is unclear whether other
543 generation mechanisms of fundamental standing waves ... can explain the localization
544 of Pgs in local time”[73]. This, too, is considered numerically: to what degree is field
545 line resonance affected by the (day-night asymmetric) conditions of the ionosphere?

546 **TODO: Transition... With the above in mind, what data would be super helpful?**

547 It's been shown that a ground magnetometer 66° north of the magnetic equator observes
548 ~10 Pg events per year. It's also been shown that poloidal Pc4s are rare compared to
549 toroidal ones, and that most poloidal Pc4s are even harmonics. However, little attention
550 has been paid to how these rates line up with one another. Given the relative occurrence
551 rate of poloidal and toroidal waves, of odd and even harmonics, and of diffuse and sharp
552 spectral peaks, just how unusual are giant pulsations?

553 **Chapter 4**

554 **Waves in Cold Resistive Plasma**

555 Before delving into the implementation of the numerical model, it's instructive to con-
556 sider the fundamental equations of waves in a cold, resistive plasma. Specifically, the
557 present chapter is concerned with waves much slower than the electron cyclotron fre-
558 quency. High-frequency waves such as the L and R modes are beyond the scope of the
559 present work — and, in fact, beyond the limits of the model described in Chapter 5.

The evolution of electric and magnetic fields is governed by Ampère's law and Faraday's law. Notably, the present work takes the linearized versions of Maxwell's equations; the vectors \underline{E} and \underline{B} indicate perturbations above the zeroth-order magnetic field.

$$\underline{\epsilon} \cdot \frac{\partial}{\partial t} \underline{E} = \frac{1}{\mu_0} \nabla \times \underline{B} - \underline{J} \quad \frac{\partial}{\partial t} \underline{B} = -\nabla \times \underline{E} \quad (4.1)$$

Current follows Ohm's law. For currents perpendicular to the background magnetic field, Kirchhoff's formulation is sufficient. Conductivity is much higher along the magnetic field lines¹, so it's appropriate to also include the electron inertial term².

$$0 = \underline{\sigma}_{\perp} \cdot \underline{E}_{\perp} - \underline{J}_{\perp} \quad \frac{1}{\nu} \frac{\partial}{\partial t} J_z = \sigma_0 E_z - J_z \quad (4.2)$$

¹The dipole coordinate system is defined rigorously in Section 5.1; at present, it's sufficient to take \hat{z} parallel to the zeroth-order magnetic field, and \hat{x} and \hat{y} perpendicular to \hat{z} (and to each other).

²Electron inertial effects are not included in the model described in Chapter 5, or in the results in Chapter 7; however, their implementation and impact are explored in Chapter 6.

Derivatives in Equations (4.1) and (4.2) can be evaluated by performing a Fourier transform. They can then be combined, eliminating the magnetic field and current terms.

$$\begin{aligned} 0 &= \underline{\underline{E}}_{\perp} + \frac{v_A^2}{\omega^2} (\underline{k} \times \underline{k} \times \underline{E})_{\perp} + \frac{i}{\epsilon_{\perp}\omega} \underline{\sigma}_{\perp} \cdot \underline{\underline{E}}_{\perp} \\ 0 &= E_z + \frac{c^2}{\omega^2} (\underline{k} \times \underline{k} \times \underline{E})_z + \frac{i\omega_P^2}{\omega(\nu - i\omega)} E_z \end{aligned} \quad (4.3)$$

The speed of light, Alfvén speed (including the displacement current correction), plasma frequency, and parallel conductivity are defined in the usual way:

$$c^2 \equiv \frac{1}{\mu_0\epsilon_0} \quad v_A^2 \equiv \frac{1}{\mu_0\epsilon_{\perp}} \quad \omega_P^2 \equiv \frac{ne^2}{m_e\epsilon_0} \quad \sigma_0 \equiv \frac{ne^2}{m_e\nu} \quad (4.4)$$

Where the perpendicular dielectric constant ϵ_{\perp} is analogous to the electric constant ϵ_0 , but for electric fields which are perpendicular to the preferred direction of the dielectric medium. As noted in Equation (3.1), $\epsilon_{\perp} \equiv \frac{\rho}{B^2}$ where ρ is the mass density and B is the magnitude of the (zeroth-order) magnetic field.

Using the vector identity $\underline{k} \times \underline{k} \times \underline{E} = \underline{k} \underline{k} \cdot \underline{E} - k^2 \underline{E}$, Equation (4.3) can be reassembled into a single expression,

$$0 = \left(\underline{\underline{\mathbb{I}}} + \frac{1}{\omega^2} \underline{\underline{V}}^2 \cdot \underline{k} \underline{k} - \frac{k^2}{\omega^2} \underline{\underline{V}}^2 + \frac{i}{\omega} \underline{\underline{\Omega}} \right) \cdot \underline{E} \quad (4.5)$$

Where $\underline{\underline{\mathbb{I}}}$ is the identity tensor and in x - y - z coordinates,

$$\underline{\underline{V}}^2 \equiv \begin{bmatrix} v_A^2 & 0 & 0 \\ 0 & v_A^2 & 0 \\ 0 & 0 & c^2 \end{bmatrix} \quad \text{and} \quad \underline{\underline{\Omega}} \equiv \begin{bmatrix} \frac{\sigma_P}{\epsilon_{\perp}} & \frac{-\sigma_H}{\epsilon_{\perp}} & 0 \\ \frac{\sigma_H}{\epsilon_{\perp}} & \frac{\sigma_P}{\epsilon_{\perp}} & 0 \\ 0 & 0 & \frac{\omega_P^2}{(\nu - i\omega)} \end{bmatrix} \quad (4.6)$$

In Equation (4.5), the expression in parentheses is the dispersion tensor. Nontrivial solutions exist only when its determinant is zero. This gives rise to a seventh-order polynomial in ω , so rather than a direct solution it's necessary to consider limits of specific interest.

568 Without loss of generality, the wave vector \underline{k} may be taken to lie in the x - z plane — that
 569 is, with $k_y = 0$. The distinction between the two perpendicular directions is discussed
 570 in Section 4.4.

571 4.1 Guided Propagation

572 The wave vector of a field line resonance aligns closely to the background magnetic
 573 field. By supposing that the two align exactly (that is, taking $k_x = 0$), the parallel and
 574 perpendicular components of the dispersion relation are decoupled.

The parallel-polarized component — that is, the solution when $E_x = E_y = 0$ — is quadratic, and thus can be solved directly.

$$0 = \omega^2 + i\nu\omega - \omega_P^2 \quad \text{so} \quad \omega = -\frac{i\nu}{2} \pm \sqrt{\omega_P^2 - \frac{\nu^2}{4}} \quad (4.7)$$

575 It bears noting that the plasma frequency is large — not just compared to Pc4 frequencies,
 576 but even compared to the collision frequencies in the ionosphere³.

Expanding Equation (4.7) with respect to large ω_P , the dispersion relation becomes

$$\omega^2 = \omega_P^2 \pm i\nu\omega_P + \dots \quad (4.8)$$

577 Equation (4.8) can hardly be called a wave, as it does not depend on the wave vector
 578 \underline{k} . Rather, it is the plasma oscillation⁴: electrons vibrating in response to a charge
 579 separation along the background magnetic field.

580 The plasma oscillation is not specifically relevant to the study of field line resonance.
 581 The two phenomena are separated by six orders of magnitude in frequency. The topic

³The collision frequency may match or exceed the plasma frequency for a thin slice at the bottom of the ionosphere, where the density of neutral atoms is large; however, it falls off quickly. Above an altitude of 200 km, conservatively[76], the plasma frequency exceeds the collision frequency by an order of magnitude or more.

⁴The plasma oscillation is also called the Langmuir wave, after Irving Langmuir.

582 is revisited in Chapter 6 insomuch as it is inseparable from the electron inertial effects
583 in Ohm's law.

The perpendicular ($E_z = 0$) components of the dispersion relation give an expression quartic in ω .

$$0 = \omega^4 + 2i\frac{\sigma_P}{\epsilon_\perp}\omega^3 - \left(2k_z^2v_A^2 + \frac{\sigma_P^2 + \sigma_H^2}{\epsilon_\perp^2}\right)\omega^2 - 2ik_z^2v_A^2\frac{\sigma_P}{\epsilon_\perp}\omega + k_z^4v_A^4 \quad (4.9)$$

Like the parallel-polarized component above, Equation (4.9) can be solved directly. Noting that \pm and \oplus are independent,

$$\omega = \left(\frac{\pm\sigma_H - i\sigma_P}{2\epsilon_\perp}\right) \oplus \sqrt{k_z^2v_A^2 + \left(\frac{\pm\sigma_H - i\sigma_P}{2\epsilon_\perp}\right)^2} \quad (4.10)$$

Also like the parallel-polarized component, the exact solution is less useful than its Taylor expansion. The Pedersen and Hall conductivities are large near the ionospheric boundary, but fall off quickly; for the vast majority of the field line, the ratios $\frac{\sigma_P}{\epsilon_\perp}$ and $\frac{\sigma_H}{\epsilon_\perp}$ are small compared to field line resonance frequencies. Expanding with respect to small conductivity gives

$$\omega^2 = k_z^2v_A^2 \oplus k_zv_A\frac{\sigma_H \pm i\sigma_P}{\epsilon_\perp} + \dots \quad (4.11)$$

584 This is the shear Alfvén wave, with a shift to its frequency due to the conductivity of
585 the ionosphere. It travels along the background magnetic field like a bead on a string,
586 with electric and magnetic field perturbations perpendicular to the magnetic field line
587 (and to one another).

588 4.2 Compressional Propagation

589 The partner to guided motion is compressional motion; in order for energy to move
590 across field lines, the wave vector must have a component perpendicular to \hat{z} . If the

591 wave vector is completely perpendicular to the magnetic field line ($k_z = 0$), the parallel
592 and perpendicular components of the dispersion relation decouple, as in Section 4.1.

The parallel-polarized ($E_x = E_y = 0$) component of the dispersion relation is

$$0 = \omega^3 + i\nu\omega^2 - (k_x^2 c^2 + \omega_P^2) \omega - ik_x^2 c^2 \nu \quad (4.12)$$

Equation (4.12) can be solved directly, though its solution (as a cubic) is far too long to be useful. Expanding with respect to the large plasma frequency, gives

$$\omega^2 = k^2 c^2 + \omega_P^2 - i\nu\omega_P + \dots \quad (4.13)$$

593 This is the O mode, a compressional wave with an electric field perturbation along
594 the background magnetic field. Like the plasma oscillation discussed in Section 4.1, its
595 frequency is very large compared to that of a field line resonance.

The perpendicular-polarized ($E_z = 0$) component of the compressional dispersion relation is also cubic.

$$0 = \omega^3 + 2i\frac{\sigma_P}{\epsilon_\perp}\omega^2 - \left(2k_x^2 v_A^2 + \frac{\sigma_P^2 + \sigma_H^2}{\epsilon_\perp^2}\right) \omega - ik_x^2 v_A^2 \frac{\sigma_P}{\epsilon_\perp} \quad (4.14)$$

A wave moving across magnetic field lines near the ionospheric boundary will encounter large $\frac{\sigma_P}{\epsilon_\perp}$ and $\frac{\sigma_H}{\epsilon_\perp}$, while at moderate to high altitudes those ratios will be small. Solving Equation (4.14) in those two limits respectively gives:

$$\omega^2 = k_x^2 v_A^2 \pm ik_x v_A \frac{\sigma_P}{\epsilon_\perp} + \dots \quad \text{and} \quad \omega^2 = k_x^2 v_A^2 + \left(\frac{\sigma_H \pm i\sigma_P}{\epsilon_\perp}\right)^2 + \dots \quad (4.15)$$

596 At first glance, both limits of Equation (4.15) appear to describe a compressional Alfvén
597 wave. The magnetic perturbation is along the background magnetic field — indicating
598 compression of the frozen-in plasma — while the electric field perturbation is perpen-
599 dicular to both the magnetic field and the wave vector.

600 However, in the high-conductivity limit, the parenthetical term actually dominates the
 601 Alfvén term, taking values as large as $\sim 10^6$ Hz. Waves at such frequencies are beyond
 602 the scope of the present work. As a matter of curiosity, however, it bears noting that
 603 (as long as $\nu \ll 10^6$ Hz) $\frac{\sigma_H}{\epsilon_{\perp}}$ reduces to the electron cyclotron frequency, $\frac{eB}{m_e}$.

604 4.3 High Altitude Limit

605 In the limit of large radial distance, it's reasonable to take the collision frequency to
 606 zero; doing so also neglects the Pedersen and Hall conductivities.

Whereas in Sections 4.1 and 4.2 it was the parallel-polarized component of the dispersion relation that factored out from the other two, the high altitude limit decouples the component polarized out of the x - z plane. The y -polarized dispersion ($E_x = E_z = 0$) is simply:

$$\omega^2 = k^2 v_A^2 \quad (4.16)$$

607 Equation (4.16) describes an Alfvén wave with an arbitrary angle of propagation. De-
 608 pending on the angle between the wave vector and the background magnetic field, it
 609 could be guided, compressional, or somewhere in between. Regardless of propagation
 610 angle, the electric field perturbation is perpendicular to both the direction of propaga-
 611 tion and the magnetic field perturbation.

The other two components (from $E_y = 0$) of the high altitude dispersion tensor give an expression quadratic in ω^2 :

$$0 = \omega^4 - (k_x^2 c^2 + k_z^2 v_A^2 + \omega_P^2) \omega^2 + k_z^2 v_A^2 \omega_P^2 \quad (4.17)$$

Which can be solved for

$$\omega^2 = \frac{1}{2} (k_x^2 c^2 + k_z^2 v_A^2 + \omega_P^2) \pm \sqrt{\frac{1}{4} (k_x^2 c^2 + k_z^2 v_A^2 + \omega_P^2)^2 - k_z^2 v_A^2 \omega_P^2} \quad (4.18)$$

Noting again that ω_P is very large, the two roots can be expanded to

$$\omega^2 = k_z^2 v_A^2 \left(1 - \frac{k_x^2 c^2 + k_z^2 v_A^2}{\omega_P^2} \right) + \dots \quad \text{and} \quad \omega^2 = k_x^2 c^2 + k_z^2 v_A^2 + \omega_P^2 + \dots \quad (4.19)$$

- 612 The first solution of Equation (4.19) is a shear Alfvén wave, as in Equation (4.11).
- 613 Notably, this form arises only when the parenthetical quantity is close to unity — as it
- 614 is for FLRs. The inertial limit, where frequencies are close to the plasma frequency, is
- 615 beyond the scope of the present work. For that same reason, the second solution (which
- 616 describes an oscillation faster than the plasma frequency) is not further considered.

617 4.4 Implications to the Present Work

- 618 The present section's findings carry three significant implications for the present work.
- 619 First — with the exception of the plasma oscillation and similar modes, which are
- 620 revisited in Chapter 6 — waves propagate at the Alfvén speed. This, in combination
- 621 with the grid configuration, will constrain the time step that can be used to model them
- 622 numerically. The time step must be sufficiently small that information traveling at the
- 623 Alfvén speed cannot “skip over” entire grid cells⁵.

Second, the results of the present section allow an estimate of the magnitude of parallel electric field that might be expected from a field line resonance compared to its perpendicular electric field. Between the full dispersion tenfor form in Equation (4.5) and the Alfvén wave described by Equation (4.19),

$$\left| \frac{E_z}{E_x} \right| = \frac{k_x k_z c^2}{\omega^2 - k_x^2 c^2 - \omega_P^2} \sim \frac{k^2 c^2}{\omega_P^2} \quad (4.20)$$

- 624 In essence, the relative magnitudes of the parallel and perpendicular electric fields should
- 625 be in proportion to the square of the relative magnitudes of the electron inertial length

⁵As is the convention, the time step is scaled down from the smallest Alfvén zone crossing time by a Courant factor, typically 0.1, meaning that it takes at least ten time steps to cross a grid cell.

626 (1 km to 100 km) and the wavelength ($\sim 10^5$ km). That is, parallel electric fields should
 627 be smaller than the perpendicular electric fields by six or more orders of magnitude.

628 Finally, the dispersion relations shown above indicate how the behavior of a field line
 629 resonance should behave as the azimuthal modenumber becomes large.

630 Whereas the shear Alfvén wave's dispersion relation depends only on the parallel com-
 631 ponent of the wave vector, the compressional Alfvén wave depends on its magnitude:
 632 $\omega^2 = k^2 v_A^2$. If the frequency is smaller than $k v_A$, the wave will become evanescent. The
 633 wave vector's magnitude can be no smaller than its smallest component, however, and
 634 the azimuthal component scales with the azimuthal modenumber: $k_y \sim \frac{m}{2\pi r}$.

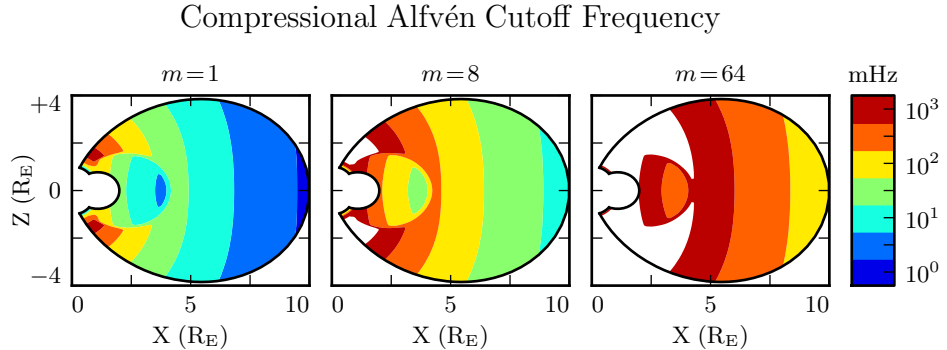


Figure 4.1: Taking $k_y \sim \frac{m}{2\pi r}$ as a lower bound for the magnitude of the wave vector, the above figure demonstrates the lowest frequency at which compressional Alfvén waves may propagate as a function of position and m . Regions shown in white are off the color scale — they have a lower bound on the order of 10^4 mHz or more. The above Alfvén frequency profile is from Kelley[49], for quiet dayside conditions, as discussed in Section 5.2.

635 This imposes a frequency cutoff on compressional Alfvén waves which scales with the
 636 azimuthal modenumber, as shown in Figure 4.1. At small values of m , most of the mag-
 637 netosphere is conducive to compressional Alfvén waves in the Pc4 frequency range. As
 638 m increases, and the wave vector with it, the inner magnetosphere becomes increasingly
 639 inaccessible to them.

640 **Chapter 5**

641 **“Tuna Half” Dimensional Model**

642 The present section describes the implementation of Tuna, a new two and a half dimensional
643 Alfvén wave code based largely on work by Lysak[60, 64].

644 The half-integer dimensionality refers to the fact that Tuna’s spatial grid resolves a
645 two-dimensional slice of the magnetosphere, but that electric and magnetic fields —
646 as well as their curls — are three-dimensional vectors. This apparent contradiction is
647 reconciled by the use of a fixed azimuthal modenumber, m . Electric and magnetic fields
648 are taken to be complex-valued, varying azimuthally per $\exp(im\phi)$; derivatives with
649 respect to ϕ are then replaced by a factor of im .

650 Unlike a fully three-dimensional code, Tuna cannot resolve the evolution of wave structures in the azimuthal direction. Furthermore, the model does not allow coupling between the dayside and nightside magnetospheres. What Tuna does offer is efficiency.
653 The model’s economical geometry allows it to include a realistic Earthward boundary:
654 grid spacing on the order of 10 km, a height-resolved ionospheric conductivity tensor,
655 and even the computation of magnetic field signatures at the ground. Such features are
656 computationally infeasible for a large global code.

657 Tuna was developed with field line resonance in mind. As discussed in Chapter 3,
658 such waves are azimuthally localized, minimizing the importance of Tuna’s missing half dimension. Moreover, because field line resonances are known to be affected by both

660 the ionosphere and the plasmasphere, a faithful treatment of the inner magnetosphere
661 is a crucial part of studying them numerically.

662 Perhaps the most exciting feature of Tuna is its novel driving mechanism: ring current
663 perturbation. Codes similar to Tuna have traditionally been driven using compressional
664 pulses at the outer boundary[60, 64, 103, 104]. This has precluded the investigation of
665 waves with large azimuthal modenumber — such as giant pulsations — which are guided,
666 and thus must be driven from within the magnetosphere.

667 TODO: The dipole geometry isn't super new, but it's not widely used. The height-
668 resolved ionosphere is new and exciting! Ground signatures are new and exciting!

669 TODO: The support software — the driver and the plotter — are also significant. Do
670 they get mentioned here? Does the Git repository where the code can be accessed get
671 mentioned here?

672 5.1 Coordinate System

Field line resonance has traditionally been modeled by straightening the field lines into a rectangular configuration[22, 67], by unrolling the azimuthal coordinate into a cylindrical coordinate system[81], or through the use of dipole coordinates[80]¹:

$$x \equiv -\frac{\sin^2 \theta}{r} \quad y \equiv \phi \quad z \equiv \frac{\cos \theta}{r^2} \quad (5.1)$$

673 Where r , θ , and ϕ take on their usual spherical meanings of radial distance, colatitude,
674 and azimuthal angle respectively.

675 The dipole coordinate x is constant over each equipotential shell², y is azimuthal angle,
676 and z indexes each field line from south to north. The unit vectors \hat{x} , \hat{y} , and \hat{z} point

¹The dipole coordinates x , y and z are perhaps more commonly named μ , ϕ , and ν respectively; however, in the present work, μ and ν take other meanings.

²In fact, x is inversely proportional to the McIlwain parameter L .

677 in the crosswise³ (radially outward at the equator), azimuthal (eastward), and parallel
 678 (northward at the equator) directions respectively.

Notably, the dipole coordinates in Equation (5.1) are normal to one another. While mathematically convenient, they do not readily accommodate a fixed-altitude boundary at the ionosphere, nor do they allow the dipole magnetic field to intersect the boundary at an oblique angle, as Earth's field does. As a solution, a nonorthogonal set of dipole coordinates was developed numerically by Proehl[79], then formalized analytically by Lysak[60] in terms of their contravariant components:

$$u^1 = -\frac{R_I}{r} \sin^2 \theta \quad u^2 = \phi \quad u^3 = \frac{R_I^2}{r^2} \frac{\cos \theta}{\cos \theta_0} \quad (5.2)$$

679 Above, R_I is the position of the ionosphere relative to Earth's center; it's typically taken
 680 to be $1 R_E + 100 \text{ km}$.

681 Like the dipole coordinates x , y , and z , Lysak's coordinates u^1 , u^2 , and u^3 correspond to
 682 L -shell, azimuthal angle, and position along a field line respectively. However, compared
 683 to z , u^3 has been renormalized using the invariant colatitude⁴ θ_0 . As a result, u^3 takes
 684 the value $+1$ at the northern ionospheric boundary and -1 at the southern ionospheric
 685 boundary for all field lines.

Because Lysak's coordinate system is not orthogonal⁵, it's necessary to consider covariant and contravariant basis vectors separately.

$$\hat{e}_i \equiv \frac{\partial}{\partial u^i} \underline{x} \quad \hat{e}^i \equiv \frac{\partial}{\partial \underline{x}} u^i \quad (5.3)$$

Covariant basis vectors \hat{e}_i are normal to the curve defined by constant u^i , while contravariant basis vectors \hat{e}^i are tangent to the coordinate curve (equivalently, \hat{e}^i is normal

³In the context of in situ measurements taken near the equatorial plane, \hat{x} is referred to as the radial direction; however, the present work extends the dipole grid to low altitudes, where \hat{x} can be more horizontal than vertical. The term "crosswise" is meant to indicate that \hat{x} is defined by the cross product of \hat{y} and \hat{z} .

⁴The invariant colatitude is the colatitude θ at which a field line intersects the ionosphere. It is related to the McIlwain parameter by $\cos \theta_0 \equiv \sqrt{1 - \frac{R_I}{L}}$.

⁵Curves of constant u^1 and curves of constant u^3 can intersect at non-right angles.

to the plane defined by constant u^j for all $j \neq i$). These vectors are reciprocal⁶ to one another, and can be combined to give components of the metric tensor $\underline{\underline{g}}$ [21].

$$\hat{e}^i \cdot \hat{e}_j = \delta_j^i \quad g_{ij} \equiv \hat{e}_i \cdot \hat{e}_j \quad g^{ij} \equiv \hat{e}^i \cdot \hat{e}^j \quad (5.4)$$

The metric tensor allows rotation between covariant and contravariant representations of vectors.

$$A_i = g_{ij} A^j \quad \text{and} \quad A^i = g^{ij} A_j \quad \text{where} \quad A_i \equiv \underline{A} \cdot \hat{e}_i \quad \text{and} \quad A^i \equiv \underline{A} \cdot \hat{e}^i \quad (5.5)$$

In addition, the determinant of the metric tensor is used to define cross products and curls⁷.

$$(\underline{A} \times \underline{B})^i = \frac{\varepsilon^{ijk}}{\sqrt{g}} A_j B_k \quad \text{and} \quad (\nabla \times \underline{A})^i = \frac{\varepsilon^{ijk}}{\sqrt{g}} \frac{\partial}{\partial u^j} A_k \quad \text{where} \quad g \equiv \det \underline{\underline{g}} \quad (5.6)$$

Explicit forms of the basis vectors and metric tensor can be found in the appendix of Lysak's 2004 paper[60]. At present, it's sufficient to note the mapping between Lysak's basis vectors and the usual dipole unit vectors.

$$\hat{x} = \frac{1}{\sqrt{g^{11}}} \hat{e}^1 \quad \hat{y} = \frac{1}{\sqrt{g^{22}}} \hat{e}^2 \quad \hat{z} = \frac{1}{\sqrt{g^{33}}} \hat{e}^3 \quad (5.7)$$

686 TODO: Do these need to be written out? Referring people to the code, which will be
687 in a public Git repository, is also a possibility.

The basis vectors can also be mapped to the spherical unit vectors, though Equation (5.8) is valid only at the ionospheric boundary.

$$\hat{\theta} = \frac{1}{\sqrt{g_{11}}} \hat{e}_1 \quad \hat{\phi} = \frac{1}{\sqrt{g_{22}}} \hat{e}_2 \quad \hat{r} = \frac{1}{\sqrt{g_{33}}} \hat{e}_3 \quad (5.8)$$

⁶The symbol δ_j^i is the Kronecker delta; the present work also makes use of the Levi-Civita symbol ε^{ijk} and Einstein's convention of implied summation over repeated indeces[24].

⁷The square root of the determinant of the metric tensor is called the Jacobian. It's sometimes denoted using the letter J , which is reserved for current in the present work.

688 The coordinates converge at the equatorial ionosphere, so an inner boundary is necessary
689 to maintain finite grid spacing. It's typically placed at $L = 2$. The outer boundary is
690 at $L = 10$. The dipole approximation of Earth's magnetic field is tenuous at the outer
691 boundary (particularly on the dayside); however, in practice, wave activity is localized
692 inside $L \sim 7$. The grid is spaced uniformly in u^1 , which gives finer resolution close to
693 Earth and coarser resolution at large distances.

694 Spacing in u^3 is set by placing grid points along the outermost field line. The points are
695 closest together at the ionosphere, and grow towards the equator. The spacing increases
696 in a geometric fashion, typically by 3%.

697 Typically, Tuna uses a grid 150 points in u^1 by 350 points in u^3 . The result is a resolution
698 on the order of 10 km at the ionosphere, which increases to the order of 10³ km at the
699 midpoint of the outermost field line.

700 There are no grid points in u^2 due to the two-and-a-half-dimensional nature of the
701 model. Fields are assumed to vary as $\exp(imu^2)$ — equally, $\exp(im\phi)$ — so derivatives
702 with respect to u^2 are equivalent to a factor of im . In effect, the real component of
703 each field is azimuthally in phase with the (purely real) driving, while imaginary values
704 represent behavior that is azimuthally offset.

705 The simulation's time step is set based on the grid spacing. As is the convention, δt is
706 set to match the smallest Alfvén zone crossing time, scaled down by a Courant factor
707 (typically 0.1). It bears noting that the smallest crossing time need not correspond to
708 the smallest zone; the Alfvén speed peaks several thousand kilometers above Earth's
709 surface, in the so-called Ionospheric Alfvén Resonator[64]. A typical time step is on the
710 order of 10⁻⁵ s.

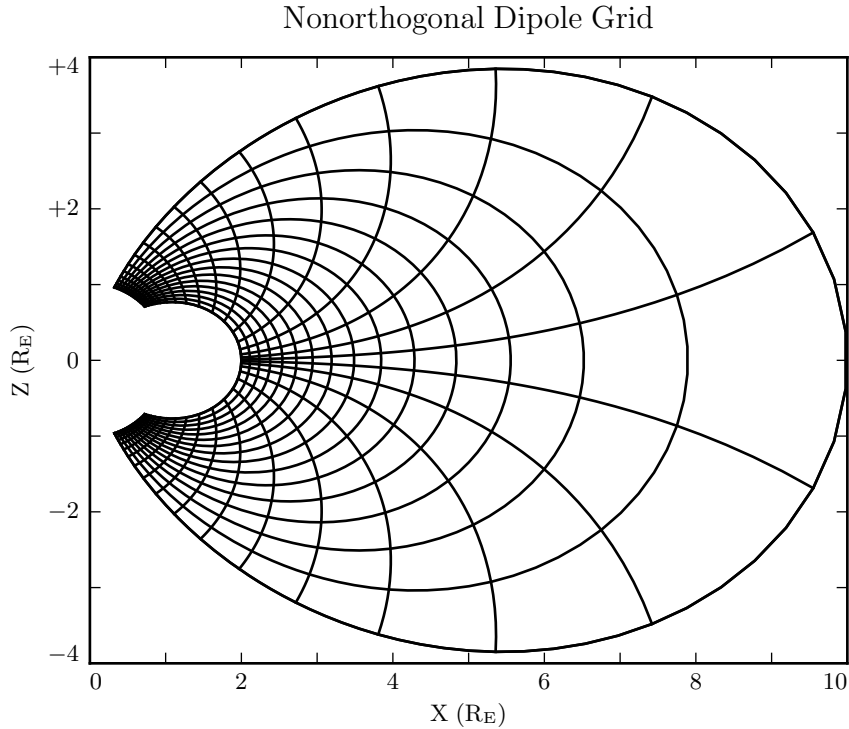


Figure 5.1: The model’s nonorthogonal dipole grid. Every fifth point is shown in each direction. The high concentration of grid points near Earth’s equator is a consequence of the coordinate system, which converges at the equatorial ionosphere. Earth (not shown) is centered at the origin with unit radius.

711 5.2 Physical Parameter Profiles

Tuna models Earth’s magnetic field to be an ideal dipole, so the zeroth-order field strength is written in the usual form:

$$\underline{B}_0 = 3.1 \times 10^4 \text{ nT} \left(\frac{R_E}{r} \right)^3 \left(2 \cos \theta \hat{r} - \sin \theta \hat{\theta} \right) \quad (5.9)$$

Number density is taken to be the sum of an inverse-radial-dependent auroral profile and a plasmaspheric profile dependent on the L -shell[64]:

$$n = n_{AZ} \frac{r_{AZ}}{r} + n_{PS} \exp\left(\frac{-L}{L_{PS}}\right) \left(\frac{1}{2} - \frac{1}{2} \tanh \frac{L - L_{PP}}{\delta L_{PP}} \right) \quad (5.10)$$

712 Where typical values are shown in Table 5.1.

Table 5.1: Typical Parameters for the Tuna Density Profile

Variable	Value	Description
L_{PS}	1.1	Scale L of the plasmasphere.
L_{PP}	4.0	Location of the plasmapause.
δL_{PP}	0.1	Thickness of the plasmapause.
n_{AZ}	$10 / \text{cm}^3$	Number density at the base of the auroral zone.
n_{PS}	$10^4 / \text{cm}^3$	Number density at the base of the plasmasphere.
r_{AZ}	1 R_E	Scale height of the auroral density distribution.

The perpendicular component of the electric tensor, ϵ_{\perp} , is computed based on Kelley's[49] tabulated low-density values, ϵ_K , which are adjusted to take into account the effects of high density in the plasmapause.

$$\epsilon_{\perp} = \epsilon_K + \frac{Mn}{B_0^2} \quad (5.11)$$

713 Where M is the mean molecular mass, which is large ($\sim 28 \text{ u}$) at 100 km altitude, then
714 drops quickly (down to 1 u by $\sim 1000 \text{ km}$)[64].

715 The Alfvén speed profile is computed from the perpendicular electric constant in the
716 usual way, $v_A^2 \equiv \frac{1}{\mu_0 \epsilon_{\perp}}$. This form takes into account the effect of the displacement
717 current, which becomes important in regions where the Alfvén speed approaches the
718 speed of light.

719 While the density profile is held constant for all runs discussed in the present work,
720 the Alfvén speed profile is not. Four different profiles are used for the low-density

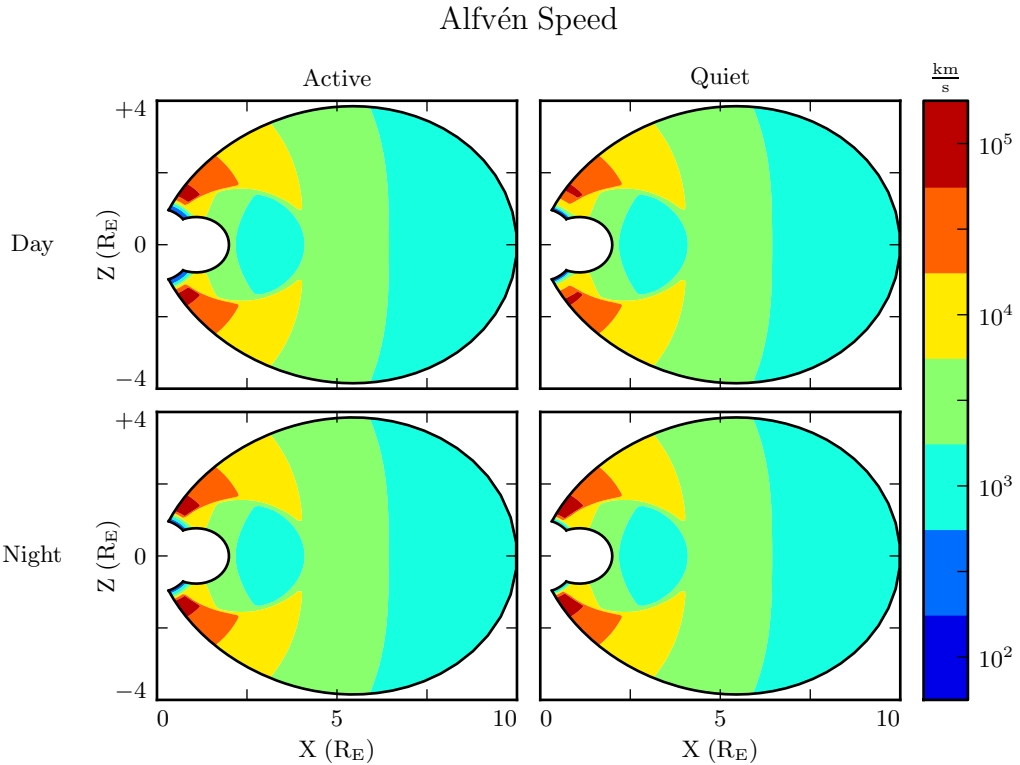


Figure 5.2: Alfvén speed profiles are based on low-density values tabulated by Kelley[49]. They are adjusted to take into account the density of the plasmapause and mass loading near the Earthward boundary.

721 perpendicular electric constant ϵ_K , corresponding to the differing ionospheric conditions
 722 between the dayside and the nightside, and between the high and low points in the
 723 solar cycle. These differences are visible in Figure 5.2, particularly in the size of the
 724 ionospheric Alfvén resonator (the peak in Alfvén speed in the high-latitude ionosphere).

725 **TODO:** Runs are only carried out for day and night... is it even worth showing the
 726 flank profile?

727 Ionospheric conductivity profiles are also based on values tabulated by Kelley, adjusted
 728 by Lysak[64] to take into account the abundance of heavy ions near the Earthward
 729 boundary. Pedersen, Hall, and parallel conductivities are each resolved by altitude, as
 730 shown in Figure 5.3.

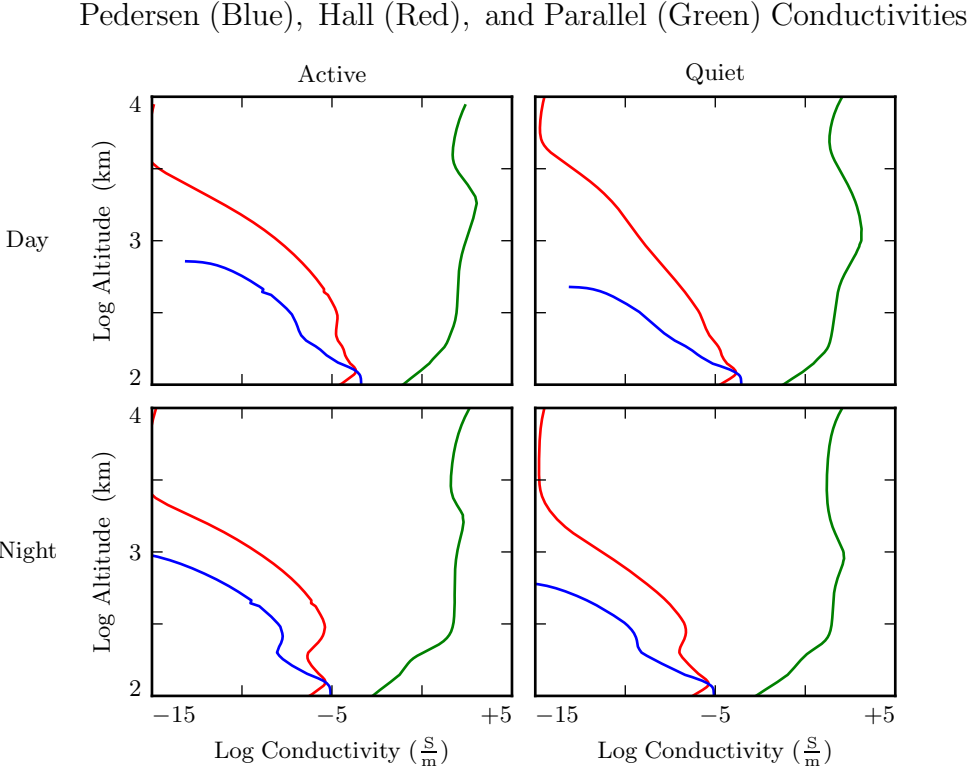


Figure 5.3: Ionospheric conductivity profiles are adapted by Lysak[64] from Kelley's tabulated values[49]. These profiles allow Tuna to simulate magnetosphere-ionosphere coupling under a variety of conditions.

731 Tuna's physical parameter profiles are static over the course of each run. Even so-called
 732 ultra low frequency waves like Pc4 pulsations are fast compared to convective timescales
 733 in the magnetosphere.

734 5.3 Driving

735 Models similar to Tuna have traditionally been driven using compression at the outer
 736 boundary[60, 64, 103, 104]. Such driving acts as a proxy for solar wind compression,
 737 Kelvin-Helmholtz effects at the magnetopause, and so on. However, because of the

738 constraints imposed by the dispersion relation for Alfvén waves⁸, simulations driven from
739 the outer boundary are constrained to the consideration of waves with low azimuthal
740 modenumber (equivalently, large azimuthal wavelength).

741 This issue is demonstrated in Figure 5.4. At low modenumber, energy delivered at
742 the outer boundary propagates across field lines in order to stimulate resonances in
743 the inner magnetosphere. However, as modenumber increases, Alfvén waves become
744 increasingly guided, and the inner magnetosphere is unaffected by perturbations at the
745 outer boundary.

746 In order to simulate high-modenumber Alfvén waves in the inner magnetosphere — such
747 as giant pulsations — a new driving mechanism is necessary. Perturbation of the ring
748 current is a natural choice, as Alfvén waves in the Pc4 range are known to interact with
749 ring current particles through drift and drift-bounce resonances. The ring current is a
750 dynamic region, particularly during and after geomagnetic storms; it's easy to imagine
751 the formation of localized inhomogeneities.

752 In order to estimate an appropriate magnitude for perturbations of the ring current,
753 the Sym-H storm index is used. The index is measured once per minute, and so cannot
754 directly detect ring current modulations in the Pc4 frequency range. Instead, the index
755 is transformed into the frequency domain, allowing a fit of its pink noise⁹.

756 **TODO:** Sym-H is basically the same as DST [102].

757 As shown in Figure 5.5, a Fourier transform of the Sym-H index (taken here from the
758 June 2013 storm) suggests that magnetic field perturbations at Earth's surface due to
759 ring current activity in the Pc4 frequency range could be up to the order of 10^{-2} nT.
760 Supposing that the ring current is centered around $5 R_E$ geocentric, that corresponds to
761 a current on the order of 0.1 MA. Tuna's driving is spread using a Gaussian profile in
762 u^1 (typically centered at $L = 5$) and u^3 (typically centered just off the equator), with a
763 characteristic area of $1 R_E^2$; this gives a current density on the order of $10^{-4} \mu\text{A}/\text{m}^2$.

⁸See Section 4.4.

⁹Pink noise, also called $\frac{1}{f}$ noise, refers to the power law decay present in the Fourier transforms of all manner of physical signals.

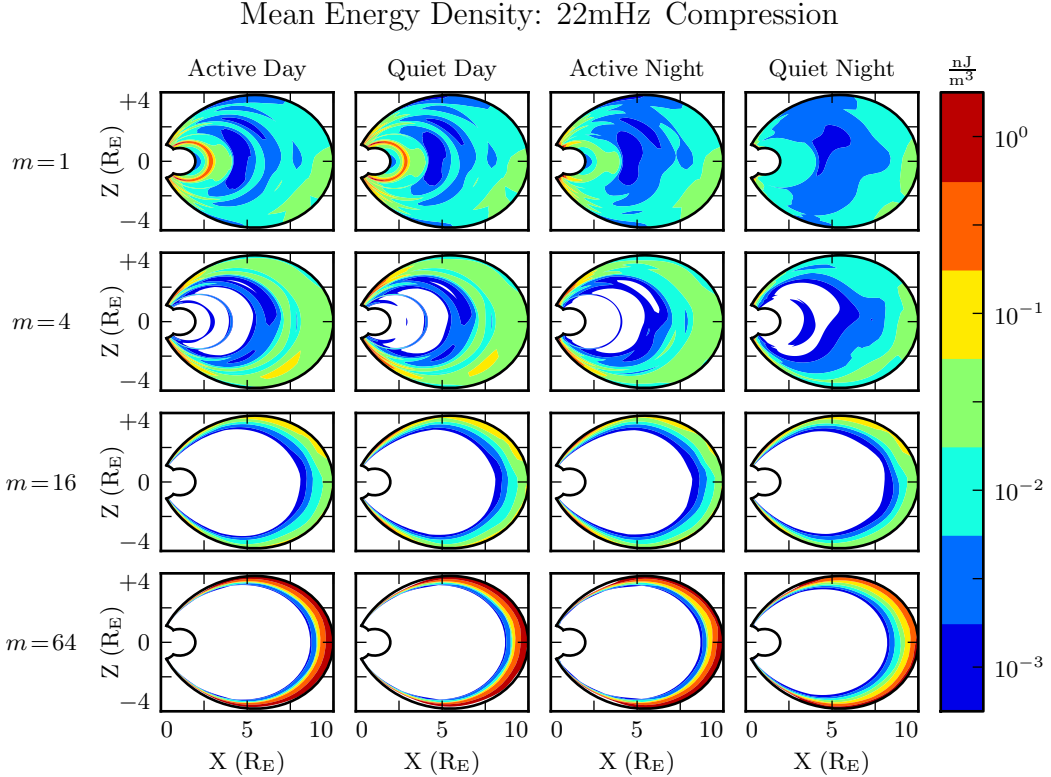


Figure 5.4: Each cell presents the mean energy density over the course of a 300s run, as a function of position, due to compressional driving at the outer boundary. Azimuthal modenumber varies by row, and ionospheric conditions vary by column. For runs with small azimuthal modenumber, it's clear that energy is able to propagate across field lines and stimulate wave activity in the inner magnetosphere. When the modenumber is large, energy is unable to penetrate to the inner magnetosphere. Notably, the large values on the bottom row should be taken with a grain of salt; it's not clear that the model's results are reliable when waves are continuously forced against the boundary.

764 TODO: Admittedly, estimating the strength of localized perturbations using Sym-H —
 765 an index averaged over the entire globe — is a bit of a kludge.

766 In situ observations of Pc4 pulsations and giant pulsations have shown waves with
 767 modenumbers across the range $1 \lesssim m \lesssim 100$ [18, 19, 93]. Simulations are carried out
 768 across that range, corresponding to ring current perturbations with azimuthal extent as
 769 small as $0.5 R_E$.

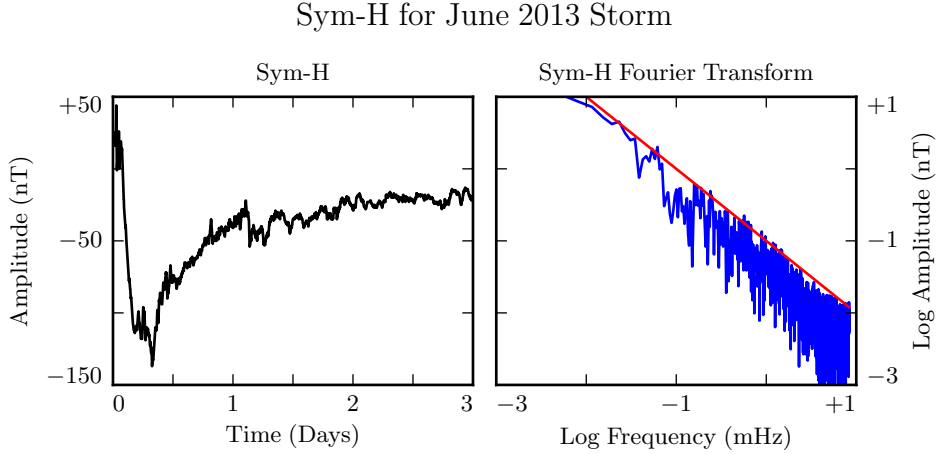


Figure 5.5: The Sym-H storm index[74] measures magnetic perturbations on Earth’s surface due to ring current activity. The amplitude of oscillations in the Pc4 range is estimated by fitting the pink noise in its Fourier transform.

- ⁷⁷⁰ TODO: Driving is delivered in the azimuthal component of the current only.
- ⁷⁷¹ TODO: Driving is sinusoidal.
- ⁷⁷² TODO: In case it’s not clear: Chapter 7 discusses ONLY simulations using ring current driving.
- ⁷⁷³ The only compressional driving we look at is Figure 5.4.

⁷⁷⁴ 5.4 Maxwell’s Equations

- ⁷⁷⁵ Tuna simulates the evolution of electromagnetic waves in accordance with Ampère’s law and Faraday’s law. Computation is carried out on a Yee grid[108]: electric fields and magnetic fields are offset by half a time step, and each field component is defined on either odd or even grid points in each dimension to ensure that curls are computed using centered differences.

The Ohmic current in Ampère’s law is replaced with $\underline{\sigma} \cdot \underline{E}$ per Kirchhoff’s formulation of Ohm’s law. Then, taking \underline{J} to represent the driving current discussed in Section 5.3,

Maxwell's equations can be written

$$\frac{\partial}{\partial t} \underline{B} = -\nabla \times \underline{E} \quad \underline{\epsilon} \cdot \frac{\partial}{\partial t} \underline{E} = \frac{1}{\mu_0} \nabla \times \underline{B} - \underline{J} - \underline{\sigma} \cdot \underline{E} \quad (5.12)$$

It is convenient to introduce shorthand for the curl of each field: $\underline{C} \equiv \nabla \times \underline{E}$ and $\underline{F} \equiv \nabla \times \underline{B} - \mu_0 \underline{J}$. Or, recalling Equation (5.6),

$$C^i = \frac{\varepsilon^{ijk}}{\sqrt{g}} \frac{\partial}{\partial u^j} E_k \quad F^i = \frac{\varepsilon^{ijk}}{\sqrt{g}} \frac{\partial}{\partial u^j} B_k - J^i \quad (5.13)$$

In these terms, Faraday's law can simply be written:

$$\frac{\partial}{\partial t} B^i = -C^i \quad (5.14)$$

Writing each component out explicitly, and using the metric tensor (per Equation (5.5)) to eliminate contravariant magnetic field components¹⁰, Equation (5.14) becomes:

$$\begin{aligned} B_1 &\leftarrow B_1 - g_{11} \delta t C^1 - g_{13} \delta t C^3 \\ B_2 &\leftarrow B_2 - g_{22} \delta t C^2 \\ B_3 &\leftarrow B_3 - g_{31} \delta t C^1 - g_{33} \delta t C^3 \end{aligned} \quad (5.15)$$

⁷⁸⁰Note that the \leftarrow operator is used in Equation (5.15) to indicate assignment, rather than equality. Terms on the left are new, while those on the right are old.

Unlike Faraday's law, Ampère's law cannot be trivially solved. Not only does the derivative of \underline{E} depend on its own future value, but the crosswise and azimuthal components of the equation are coupled by the Hall terms in the conductivity tensor. Fortunately,

¹⁰Fields are stored only in terms of their covariant components, and curls in terms of their contravariant components. This reduces Tuna's memory footprint (since each field need not be stored twice) as well as its computational cost (since time need not be spent rotating between bases). As a result, Tuna's solutions to Maxwell's equations are linear expressions whose coefficients are a mishmash of physical constants and geometric factors. To save time, each coefficient is computed once and stored, rather than being multiplied out from scratch with each time step.

the electric tensor can be inverted, allowing a solution by integrating factors:

$$\underline{\epsilon} \cdot \frac{\partial}{\partial t} \underline{E} = \frac{1}{\mu_0} \underline{F} - \underline{\sigma} \cdot \underline{E} \quad \text{becomes} \quad \left(\underline{\Omega} + \underline{\mathbb{I}} \frac{\partial}{\partial t} \right) \cdot \underline{E} = \underline{V}^2 \cdot \underline{F} \quad (5.16)$$

Where $\underline{\mathbb{I}}$ is the identity tensor and in x - y - z coordinates¹¹,

$$\underline{V}^2 \equiv \frac{1}{\mu_0} \underline{\epsilon}^{-1} = \begin{bmatrix} v_A^2 & 0 & 0 \\ 0 & v_A^2 & 0 \\ 0 & 0 & c^2 \end{bmatrix} \quad \text{and} \quad \underline{\Omega} \equiv \underline{\epsilon}^{-1} \cdot \underline{\sigma} = \begin{bmatrix} \frac{\sigma_P}{\epsilon_{\perp}} & \frac{-\sigma_H}{\epsilon_{\perp}} & 0 \\ \frac{\sigma_H}{\epsilon_{\perp}} & \frac{\sigma_P}{\epsilon_{\perp}} & 0 \\ 0 & 0 & \frac{\sigma_0}{\epsilon_0} \end{bmatrix} \quad (5.17)$$

Multiplying through by $\exp(\underline{\Omega} t)$ and applying the product rule, Equation (5.16) becomes¹²

$$\frac{\partial}{\partial t} \left(\exp(\underline{\Omega} t) \cdot \underline{E} \right) = \exp(\underline{\Omega} t) \cdot \underline{V}^2 \cdot \underline{F} \quad (5.18)$$

Equation (5.18) can then be integrated over a small time step δt and expressed in terms of the assignment operator introduced in Equation (5.15).

$$\underline{E} \leftarrow \exp(-\underline{\Omega} \delta t) \cdot \underline{E} + \delta t \exp(-\underline{\Omega} \frac{\delta t}{2}) \cdot \underline{V}^2 \cdot \underline{F} \quad (5.19)$$

The tensor exponential can be evaluated by splitting $\underline{\Omega}$ into the sum of its diagonal and Hall components¹³. The Hall exponential condenses into sines and cosines, giving a rotation around the magnetic field line:

$$\underline{E} \leftarrow \exp(-\underline{\Omega}' \delta t) \cdot \underline{R}_z \left(\frac{-\sigma_H \delta t}{\epsilon_{\perp}} \right) \cdot \underline{E} + \delta t \underline{V}^2 \cdot \exp(-\underline{\Omega}' \frac{\delta t}{2}) \cdot \underline{R}_z \left(\frac{-\sigma_H \delta t}{2\epsilon_{\perp}} \right) \cdot \underline{F} \quad (5.20)$$

¹¹Note the parallel component of the present definition of $\underline{\Omega}$ differs slightly from that used in Chapter 4, due to the present neglect of inertial effects; see Chapter 6.

¹²Tensor exponentiation is analogous to scalar exponentiation[38]: $\exp(\underline{T}) \equiv \sum_n \frac{1}{n!} \underline{T}^n$.

¹³For tensors, $\exp(\underline{S} + \underline{T}) = \exp(\underline{S}) \exp(\underline{T})$ as long as $\underline{S} \cdot \underline{T} = \underline{T} \cdot \underline{S}$.

Where

$$\underline{\underline{R}}_z(\theta) = \begin{bmatrix} \cos \theta & -\sin \theta & 0 \\ \sin \theta & \cos \theta & 0 \\ 0 & 0 & 1 \end{bmatrix} \quad \text{and} \quad \underline{\underline{\Omega}}' \equiv \begin{bmatrix} \frac{\sigma_P}{\epsilon_{\perp}} & 0 & 0 \\ 0 & \frac{\sigma_P}{\epsilon_{\perp}} & 0 \\ 0 & 0 & \frac{\sigma_0}{\epsilon_0} \end{bmatrix} \quad (5.21)$$

The parallel component of term of Equation (5.20) is simply

$$E_z \leftarrow E_z \exp\left(\frac{-\sigma_0 \delta t}{\epsilon_0}\right) + c^2 \delta t F_z \exp\left(\frac{-\sigma_0 \delta t}{2\epsilon_0}\right) \quad (5.22)$$

Or, using Equation (5.7) to map to the covariant basis,

$$E_3 \leftarrow E_3 \exp\left(\frac{-\sigma_0 \delta t}{\epsilon_0}\right) + c^2 \delta t (g_{31} F^1 + g_{33} F^3) \exp\left(\frac{-\sigma_0 \delta t}{2\epsilon_0}\right) \quad (5.23)$$

782 Tuna's conductivity profile gives a minimum value of $\frac{\sigma_0 \delta t}{\epsilon_0}$ on the order of 10^3 , making
 783 $\exp\left(\frac{-\sigma_0 \delta t}{\epsilon_0}\right)$ far too small to be stored in a double precision variable¹⁴. That is, this
 784 model takes E_3 (and, proportionally, E_z) to be uniformly zero. This issue is revisited
 785 in Chapter 6.

The perpendicular components of Equation (5.20) give the expressions:

$$\begin{aligned} E_1 + \frac{g^{13}}{g^{11}} E_3 &\leftarrow E_1 \cos\left(\frac{-\sigma_H \delta t}{\epsilon_{\perp}}\right) \exp\left(\frac{-\sigma_P \delta t}{\epsilon_{\perp}}\right) \\ &\quad + E_2 \sin\left(\frac{-\sigma_H \delta t}{\epsilon_{\perp}}\right) \exp\left(\frac{-\sigma_P \delta t}{\epsilon_{\perp}}\right) \sqrt{\frac{g^{22}}{g^{11}}} \\ &\quad + E_3 \cos\left(\frac{-\sigma_H \delta t}{\epsilon_{\perp}}\right) \exp\left(\frac{-\sigma_P \delta t}{\epsilon_{\perp}}\right) \frac{g^{13}}{g^{11}} \\ &\quad + F^1 \cos\left(\frac{-\sigma_H \delta t}{2\epsilon_{\perp}}\right) \exp\left(\frac{-\sigma_P \delta t}{2\epsilon_{\perp}}\right) \frac{v_A^2 \delta t}{g^{11}} \\ &\quad + F^2 \sin\left(\frac{-\sigma_H \delta t}{2\epsilon_{\perp}}\right) \exp\left(\frac{-\sigma_P \delta t}{2\epsilon_{\perp}}\right) \frac{v_A^2 \delta t}{\sqrt{g^{11} g^{22}}} \end{aligned} \quad (5.24)$$

¹⁴Not coincidentally, $\frac{\sigma_0}{\epsilon_0}$ can also be written $\frac{\omega_P^2}{\nu}$. At the ionosphere, the collision frequency ν is fast compared to field line resonance timescales, but it's still slow compared to the plasma frequency.

and

$$\begin{aligned}
E_2 \leftarrow & -E_1 \sin\left(\frac{-\sigma_H \delta t}{\epsilon_{\perp}}\right) \exp\left(\frac{-\sigma_P \delta t}{\epsilon_{\perp}}\right) \sqrt{\frac{g^{11}}{g^{22}}} \\
& + E_2 \cos\left(\frac{-\sigma_H \delta t}{\epsilon_{\perp}}\right) \exp\left(\frac{-\sigma_P \delta t}{\epsilon_{\perp}}\right) \\
& - E_3 \sin\left(\frac{-\sigma_H \delta t}{\epsilon_{\perp}}\right) \exp\left(\frac{-\sigma_P \delta t}{\epsilon_{\perp}}\right) \frac{g^{13}}{\sqrt{g^{11} g^{22}}} \\
& - F^1 \sin\left(\frac{-\sigma_H \delta t}{2\epsilon_{\perp}}\right) \exp\left(\frac{-\sigma_P \delta t}{2\epsilon_{\perp}}\right) \frac{v_A^2 \delta t}{\sqrt{g^{11} g^{22}}} \\
& + F^2 \cos\left(\frac{-\sigma_H \delta t}{2\epsilon_{\perp}}\right) \exp\left(\frac{-\sigma_P \delta t}{2\epsilon_{\perp}}\right) \frac{v_A^2 \delta t}{g^{22}}
\end{aligned} \tag{5.25}$$

786 The E_3 terms in Equations (5.24) and (5.25) can be ignored at present. They are
787 revisited in Chapter 6.

788 It bears recalling that the driving current is defined as part of \underline{F} , per Equation (5.13).
789 When the driving current is purely azimuthal ($J^1 = J^3 = 0$), the driving is in principle
790 applied to both the poloidal and the toroidal electric fields through F^2 . However,
791 in practice, the driving applied to the toroidal electric field is vanishingly small. The
792 driving current J^2 is localized around $5 R_E$ geocentric, and $\exp\left(\frac{-\sigma_P \delta t}{2\epsilon_{\perp}}\right)$ drops off quickly
793 with altitude.

794 5.5 Boundary Conditions

795 Dirichlet and Neumann boundary conditions are applied to the electric field components
796 and magnetic field components respectively. That is, electric fields are forced to go to
797 zero at the inner and outer boundaries, and magnetic fields are forced to have a zero
798 derivative normal to the inner and outer boundaries.

799 These boundary conditions can in principle cause nonphysical reflections at the bound-
800 ary¹⁵. However, in practice, wave activity is concentrated well within the simulation
801 domain. Simulation results are robust under an exchange of Dirichlet and Neumann

¹⁵See, for example, the bottom row of Figure 5.4.

boundary conditions (though a self-inconsistent set of boundary conditions, such as applying Neumann boundary conditions to B_1 but Dirichlet boundary conditions to B_3 , quickly causes instability).

The Earthward boundary conditions are as follows.

Between the top of the neutral atmosphere and the bottom of the ionosphere, the model includes a thin, horizontal current sheet representing the ionosphere's E layer[60]. By integrating Ampère's law over the layer, it can be shown[29] that the horizontal electric field values at the edge of the grid are determined by the jump in the horizontal magnetic fields:

$$\underline{\underline{\Sigma}} \cdot \underline{E} = \frac{1}{\mu_0} \lim_{\delta r \rightarrow 0} \left[\hat{r} \times \underline{B} \right]_{R_I - \delta r}^{R_I + \delta r} \quad (5.26)$$

The integrated conductivity tensor $\underline{\underline{\Sigma}}$ can be written in θ - ϕ coordinates as[60]:

$$\underline{\underline{\Sigma}} \equiv \begin{bmatrix} \frac{\Sigma_0 \Sigma_P}{\Sigma_0 \cos^2 \alpha + \Sigma_P \sin^2 \alpha} & \frac{-\Sigma_0 \Sigma_H}{\Sigma_0 \cos^2 \alpha + \Sigma_P \sin^2 \alpha} \\ \frac{\Sigma_0 \Sigma_H}{\Sigma_0 \cos^2 \alpha + \Sigma_P \sin^2 \alpha} & \Sigma_P + \frac{\Sigma_H^2 \sin^2 \alpha}{\Sigma_0 \cos^2 \alpha + \Sigma_P \sin^2 \alpha} \end{bmatrix} \quad (5.27)$$

Where α is the angle between the magnetic field and the vertical direction, given by $\cos \alpha \equiv \frac{-2 \cos \theta}{\sqrt{1+3 \cos^2 \theta}}$, and Σ_P , Σ_H , and Σ_0 are the height-integrated Pedersen, Hall, and parallel conductivities respectively. Their values are determined by integrating Kelley's[49] conductivity profiles from Earth's surface to the ionospheric boundary; values are shown in Table 5.2.

Table 5.2: Integrated Atmospheric Conductivity (S)

	Σ_0	Σ_P	Σ_H
Active Day	424	0.65	6.03
Quiet Day	284	0.44	4.02
Active Night	9	0.01	0.12
Quiet Night	9	0.01	0.12

An expression for the horizontal electric fields at the boundary can be obtained by inverting Equation (5.26). After mapping to covariant coordinates per Equation (5.8), and taking $\Sigma \equiv \det \underline{\underline{\Sigma}}$,

$$\begin{aligned} E_1 &\leftarrow \frac{1}{\mu_0 \Sigma} \lim_{\delta r \rightarrow 0} \left[-\Sigma_{\theta\phi} B_1 - \sqrt{\frac{g_{11}}{g_{22}}} \Sigma_{\phi\phi} B_2 \right]_{R_I-\delta r}^{R_I+\delta r} \\ E_2 &\leftarrow \frac{1}{\mu_0 \Sigma} \lim_{\delta r \rightarrow 0} \left[\sqrt{\frac{g_{22}}{g_{11}}} \Sigma_{\theta\theta} B_1 + \Sigma_{\phi\theta} B_2 \right]_{R_I-\delta r}^{R_I+\delta r} \end{aligned} \quad (5.28)$$

811 In order to compute the atmospheric magnetic field, a scalar magnetic potential (Ψ
812 such that $\underline{B} = \nabla\Psi$) is computed as a linear combination of harmonics. The neutral
813 atmosphere is considered to be a perfect insulator, giving $\nabla \times \underline{B} = 0$. Combined with
814 $\nabla \cdot \underline{B} = 0$ (per Maxwell's equations), Ψ satisfies Laplace's equation, $\nabla^2\Psi = 0$.

Laplace's equation can be solved analytically; however, a numerical solution is preferable to ensure orthonormality on a discrete and incomplete¹⁶ grid. After separating out the radial and azimuthal dependence in the usual way, the latitudinal component of Laplace's equation can be written in terms of $s \equiv -\sin^2\theta$:

$$(4s^2 + 4s) \frac{d^2}{ds^2} Y_\ell + (4 + 6s) \frac{d}{ds} Y_\ell - \frac{m^2}{s} Y_\ell = \ell(\ell+1) Y_\ell \quad (5.29)$$

Using centered differences to linearize the derivatives, Equation (5.29) becomes a system of coupled linear equations, one per field line. It can be solved numerically for eigenvalues $\ell(\ell+1)$ and eigenfunctions Y_ℓ ¹⁷. In terms of the harmonics Y_ℓ , Ψ between the Earth's surface and the top of the atmosphere can be written using eigenweights a_ℓ and b_ℓ :

$$\Psi = \sum_\ell \left(a_\ell r^\ell + b_\ell r^{-\ell-1} \right) Y_\ell \quad (5.30)$$

¹⁶As discussed in Section 5.1, the grid is constrained to finite L , which excludes the equator as well as the poles.

¹⁷Solving Laplace's equation analytically results in spherical harmonics indexed by both ℓ and m , the separation constants for θ and ϕ respectively. In two and a half dimensions, ϕ is not explicitly resolved, so m is set manually.

As a boundary condition for Ψ , Earth is assumed to be a perfect conductor. This forces the magnetic field at Earth's surface to be horizontal; that is, $B_r = \frac{\partial}{\partial r}\Psi = 0$. Noting that solutions to Laplace's equation are orthonormal, each element of the sum in Equation (5.30) must be independently zero at R_E . This allows the coefficients a_ℓ and b_ℓ to be expressed in terms of one another.

$$b_\ell = \frac{\ell}{\ell+1} R_E^{2\ell+1} a_\ell \quad (5.31)$$

The current sheet at the top of the atmosphere is assumed to be horizontal, so the radial component of the magnetic field must be the same just above and just below it. Taking the radial derivative of Equation (5.30) at the top of the atmosphere, and eliminating b_ℓ with Equation (5.31), gives

$$B_r = \sum_\ell \ell a_\ell R_I^{\ell-1} \left(1 - \lambda^{2\ell+1}\right) Y_\ell \quad \text{where} \quad \lambda \equiv \frac{R_E}{R_I} \sim 0.975 \quad (5.32)$$

The summation can be collapsed by “integrating” over a harmonic¹⁸. Inverse harmonics can be obtained by inverting the eigenvector matrix. Then $Y_\ell \cdot Y_{\ell'}^{-1} = \delta_{\ell\ell'}$ by construction.

$$a_\ell = \frac{1}{\ell R_I^{\ell-1}} \frac{B_r \cdot Y_\ell^{-1}}{1 - \lambda^{2\ell+1}} \quad (5.33)$$

Combining Equations (5.30), (5.31), and (5.33) allows the expression of Ψ at the top and bottom of the atmosphere as a linear combination of radial magnetic field components at the bottom of the ionosphere.

$$\begin{aligned} \Psi_E &= \sum_\ell Y_\ell \frac{R_I}{\ell(\ell-1)} \frac{(2\ell-1)\lambda^\ell}{1-\lambda^{2\ell+1}} B_r \cdot Y_\ell^{-1} \\ \Psi_I &= \sum_\ell Y_\ell \frac{R_I}{\ell(\ell-1)} \frac{(\ell-1)+\ell\lambda^{2\ell+1}}{1-\lambda^{2\ell+1}} B_r \cdot Y_\ell^{-1} \end{aligned} \quad (5.34)$$

¹⁸Because the functions are defined on a discrete grid, their inner product is not an integral, but a sum: $B_r \cdot Y_\ell^{-1} \equiv \sum_i B_r[i] Y_\ell^{-1}[i]$.

Horizontal magnetic fields are obtained by taking derivatives of Ψ .

$$B_1 = \frac{\partial}{\partial u^1} \Psi \quad B_2 = \frac{\partial}{\partial u^2} \Psi \quad (5.35)$$

- 815 Horizontal magnetic field values at the top of the atmosphere are used to impose bound-
816 ary conditions on the electric fields at the bottom of the ionosphere, per Equation (5.28).
817 Those at Earth's surface are valuable because they allow a direct comparison between
818 model output and ground magnetometer data, after being mapped to physical coordi-
819 nates per Equation (5.8).

820 **Chapter 6**

821 **Electron Inertial Effects**

822 As laid out in Chapter 5, Tuna resolves neither parallel currents nor parallel electric
823 fields. This is unfortunate; parallel electric fields generated by kinetic and inertial Alfvén
824 waves (including fundamental field line resonances[82, 98]) are a topic of particular
825 interest in the study of auroral particle precipitation.

Parallel currents and electric fields can be added to Tuna through the consideration of electron inertial effects in Ohm's law:

$$0 = \sigma_0 E_z - J_z \quad \text{becomes} \quad \frac{1}{\nu} \frac{\partial}{\partial t} J_z = \sigma_0 E_z - J_z \quad (6.1)$$

With the addition of the electron inertial term, it is necessary to track the parallel current independent of the parallel electric field¹. Solving by integrating factors² gives

$$J_3 \leftarrow J_3 \exp(-\nu \delta t) + \delta t \frac{ne^2}{m_e} E_3 \exp\left(-\nu \frac{\delta t}{2}\right) \quad (6.2)$$

¹The parallel current J_z is defined on the same points of the Yee grid as E_z . It is offset in time by half of a time step.

²The integrating factors technique is laid out explicitly for Ampère's law in Section 5.4.

From there, the parallel electric field can be updated directly; Equation (5.23) is replaced by the following:

$$E_3 \leftarrow E_3 + c^2 \delta t (g_{31} F^1 + g_{33} F^3) - \frac{\delta t}{\epsilon_0} J_3 \quad (6.3)$$

- 826 The present section explores the complications that arise from the addition of the elec-
tron inertial term to Ohm's law, as well as a few results that may be gleaned despite
828 those complications. Notably — for reasons discussed in Section 6.3 — the results
829 presented in Chapter 7 do not make use of the electron inertial term.
- 830 Inertial effects have been considered in previous numerical work, such as by Lysak and
831 Song in 2001[62], but never at the global scale. Lysak and Song considered waves in
832 the ionospheric Alfvén resonator, with frequencies of hundreds of mHz. Their work did
833 not account for the effects of the dipolar geometry, such as differences that might arise
834 between poloidal and toroidal resonances. In fact, in that work, circular polarization
835 (essentially a superposition of poloidal and toroidal modes) was noted to be a promising
836 avenue for future work.

837 6.1 The Boris Factor

With the addition of the electron inertial term, a cyclical dependence appears between Ampère's law and Ohm's law:

$$\frac{\partial}{\partial t} E_z \sim -\frac{1}{\epsilon_0} J_z \quad \text{and} \quad \frac{\partial}{\partial t} J_z \sim \frac{n e^2}{m_e} E_z \quad \text{so} \quad \frac{\partial^2}{\partial t^2} E_z \sim -\omega_P^2 E_z \quad (6.4)$$

- 838 That is, electron inertial effects come hand in hand with the plasma oscillation.
- 839 As mentioned in Chapter 4 and shown in Figure 6.1, plasma oscillation is quite fast —
840 several orders of magnitude smaller than Tuna's time step as determined in Section 5.1
841 ($\sim 10 \mu\text{s}$). This poses a conundrum. At Tuna's usual time step, the plasma oscillation
842 becomes unstable within seconds³. On the other hand, reducing the time step by three

³For stability, $\omega_P \delta t < 1$ is necessary.

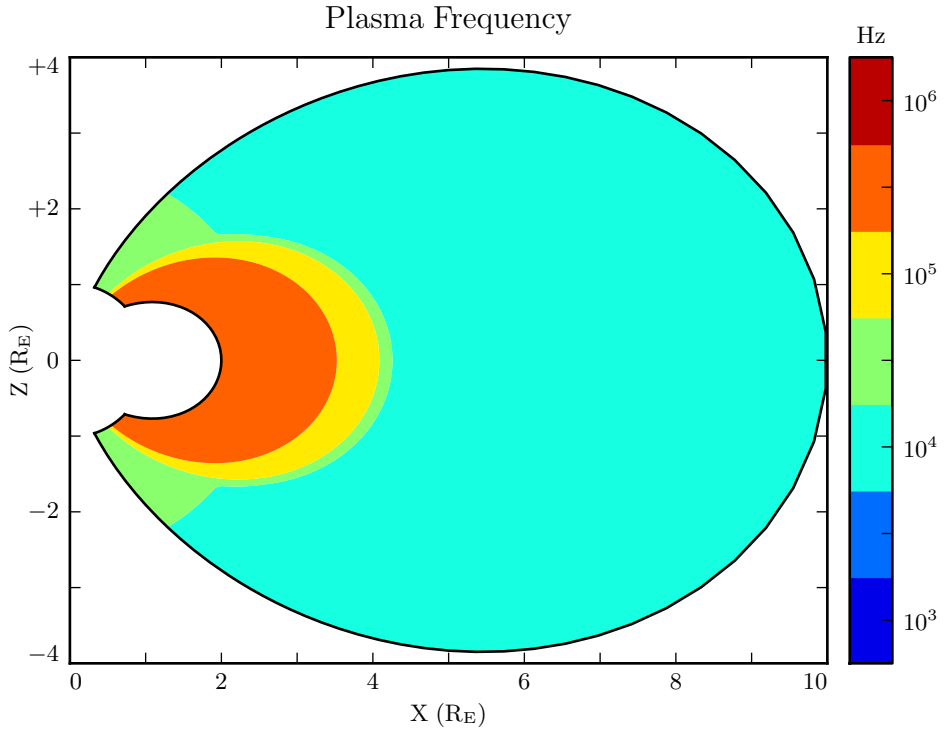


Figure 6.1: The plasma frequency reaches a peak value just under 10^6 Hz near the equator. Outside the plasmasphere, its value is closer to 10^4 Hz, which is still not well-resolved by Tuna's usual time step.

843 orders of magnitude to resolve the plasma oscillation is computationally infeasible; a
 844 run slated for an hour would require six weeks to complete.

845 As it happens, this problem can be solved by artificially increasing the parallel electric
 846 constant above its usual value of ϵ_0 . Doing so lowers both the speed of light and the
 847 plasma frequency within the simulation.

848 This technique — and others like it — has been widespread in numerical modeling since
 849 it was presented by Boris in 1970[7]. The following paraphrases an argument by Lysak
 850 and Song[62], outlining its validity specifically in the case of electron inertial effects.

Supposing that the current and electric field are oscillating at frequency ω , the parallel components of Ampère's law and Ohm's law can be written

$$-i\omega\epsilon_0 E_z = \frac{1}{\mu_0} (\nabla \times \underline{B})_z - J_z \quad -\frac{i\omega}{\nu} J_z = \sigma_0 E_z - J_z \quad (6.5)$$

Then, eliminating the current, the parallel electric field can be related to the curl of the magnetic field by⁴

$$\left(1 - \frac{\omega^2 - i\nu\omega}{\omega_P^2}\right) E_z = \frac{c^2}{\omega_P^2} (\nu - i\omega) (\nabla \times \underline{B})_z \quad (6.6)$$

- 851 In Equation (6.6), $\frac{c}{\omega_P}$ is the electron inertial length. While the speed of light and the
 852 plasma frequency each depend on ϵ_0 , their ratio does not. This allows an estimation of
 853 how much the model should be affected by an artificially-large electric constant (and
 854 thus an artificially-small plasma frequency). So long as $\frac{\omega^2 - i\nu\omega}{\omega_P^2}$ remains small compared
 855 to unity, the model should behave faithfully.
- 856 For waves with periods of a minute or so, even perhaps-implausibly large Boris factors
 857 are allowed; for example, increasing ϵ_0 by a factor of 10^6 gives $\left|\frac{\omega^2 + i\omega\nu}{\omega_P^2}\right| \lesssim 0.01$.

858 6.2 Parallel Currents and Electric Fields

- 859 As discussed in Section 4.4, parallel electric fields in this regime are expected to be six
 860 or more orders of magnitude smaller than the perpendicular electric fields. Numerical
 861 results show general agreement: in Figure 6.2, the parallel electric field appears com-
 862 parable to its perpendicular counterparts only after its been scaled up by six orders of
 863 magnitude.
- 864 As such, the inclusion of electron inertial effects does not appreciably impact the simu-
 865 lation's gross behavior; in Faraday's law, $\nabla \times \underline{E}$ is essentially unaffected. Side by side

⁴From Equation (4.4), $c^2 \equiv \frac{1}{\mu_0\epsilon_0}$ and $\sigma_0 \equiv \frac{ne^2}{m_e\nu}$ and $\omega_P^2 \equiv \frac{ne^2}{m_e\epsilon_0}$.

Electric Field Snapshots: Quiet Day, 10mHz Current, $m = 16$

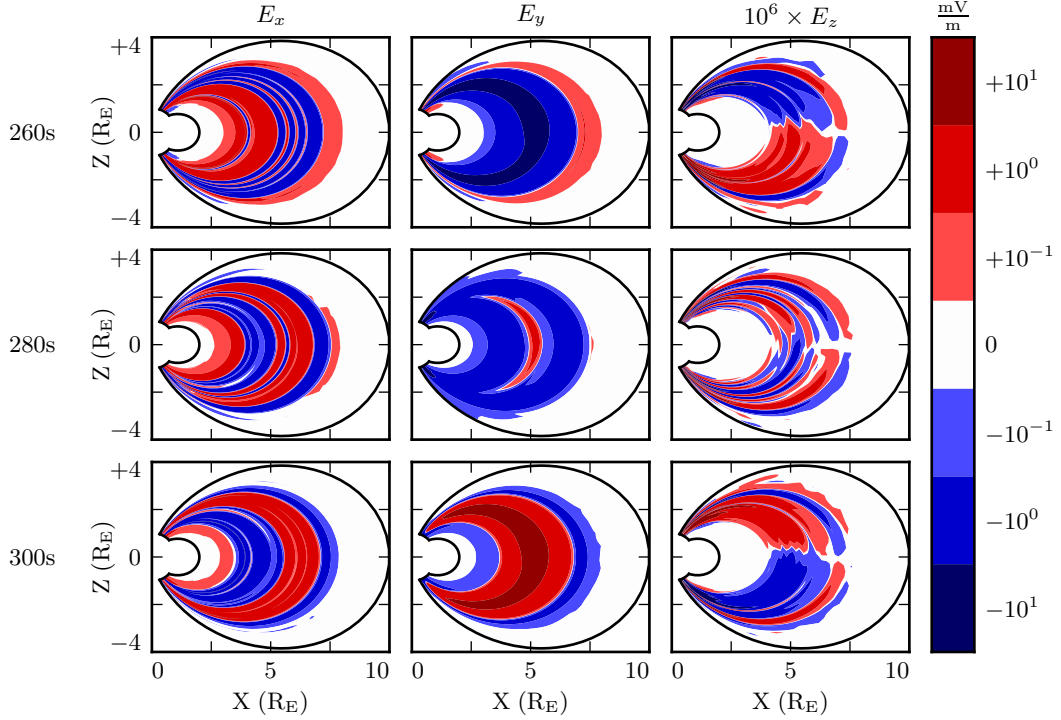


Figure 6.2: Parallel electric fields are smaller than perpendicular electric fields by about six orders of magnitude. As a result, parallel electric fields do not contribute significantly to $\nabla \times \underline{E}$ in Faraday's law.

866 snapshots of the magnetic fields in runs carried out with and without electron inertial
 867 effects are not visibly distinguishable⁵ (not shown).

868 Even if there is no significant feedback through Faraday's law, it's informative to con-
 869 sider the structures that arise in parallel currents and electric fields driven by pertur-
 870 bations in the ring current. For example, in Figure 6.2, the parallel electric field per-
 871 turbation (with maxima near the ionosphere) exhibits the opposite harmonic structure
 872 to the perpendicular electric field components (which peak near the equator).

⁵In a sense, this is reassuring. It ensures that the present section does not cast doubt on the results presented in Chapter 7, where electron inertial effects are neglected.

Current and Poynting Flux at 100km: Quiet Day , 16mHz Current

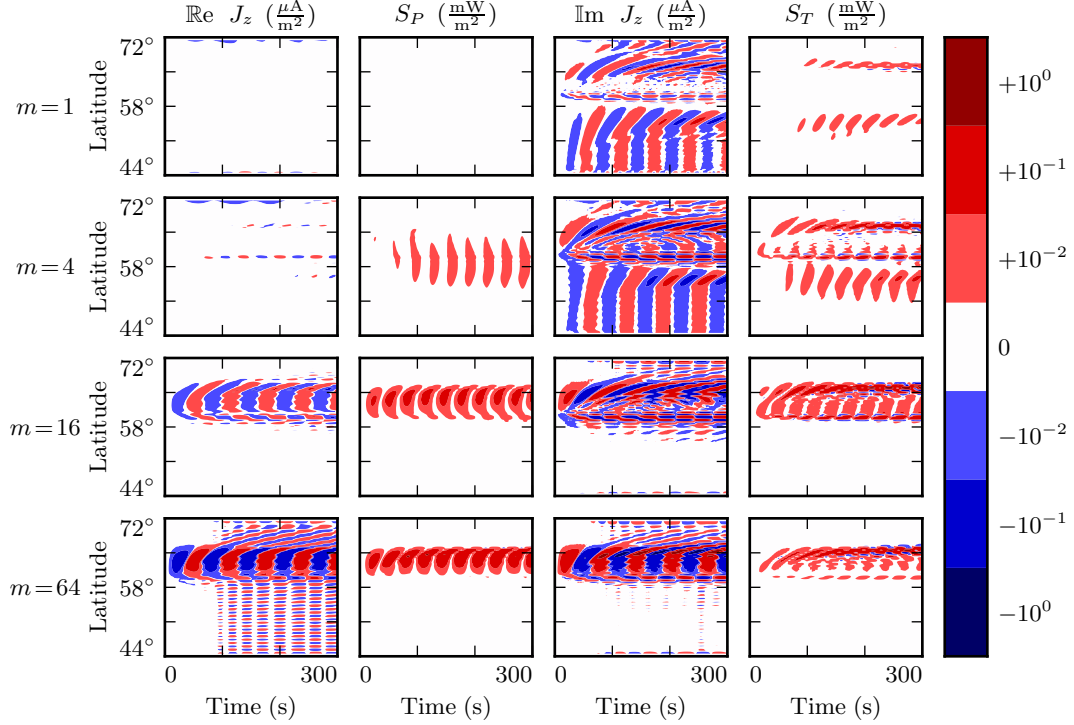


Figure 6.3: Four runs are shown above, one per row, with azimuthal modenumbers of 1, 4, 16, and 64. Columns show slices at 100 km of the real parallel current, poloidal Poynting flux, imaginary current, and toroidal Poynting flux respectively. The similarity visible across columns suggests that the real parallel current follows the poloidal Poynting flux, while the imaginary parallel current follows the toroidal Poynting flux (the toroidal fields are imaginary). At least, this is the case in regions of significant Hall conductivity.

873 At low altitude, the Hall conductivity muddles the poloidal and toroidal electric fields.
 874 In this region, as shown in Figure 6.3, parallel currents coincide with strong Poynting
 875 flux. The imaginary component of the current lines up with the toroidal Poynting flux
 876 (which comes from imaginary E_x and imaginary B_y^*), while the real current lines up
 877 with the poloidal Poynting flux (E_y and B_x^* are real)⁶.

⁶As mentioned in Chapter 5, poloidal field components are in practice overwhelmingly real, indicating that they coincide azimuthally with the (real) driving. Toroidal components are overwhelmingly imaginary, which corresponds to an azimuthal offset.

878 Four runs are shown in Figure 6.3, one per row, with azimuthal modenumbers 1, 4, 16,
879 and 64. The first and third columns show the real and imaginary components of the
880 parallel current respectively, in units of $\mu\text{A}/\text{m}^2$, sliced at an altitude of 100 km, the edge
881 of the simulation domain. The second and fourth columns are the poloidal and toroidal
882 Poynting flux respectively, in units of mW/m^2 . Latitude is shown on the vertical axis,
883 and time on the horizontal axis.

884 At higher altitude, where the Hall conductivity is small, parallel current is associated
885 only with the toroidal mode. Figure 6.4 shows data from the same runs as Figure 6.3,
886 arranged in the same way, but the values are taken at an altitude of 1000 km instead of
887 100 km.

888 In Figure 6.4, as in Figure 6.3, the imaginary component of the parallel current (third
889 column) coincides more or less with the toroidal Poynting flux (fourth column). How-
890 ever, the real component of the parallel current (first column) is vanishingly small, even
891 when the poloidal Poynting flux (second column) is strong.

892 **TODO:** Is this expected? Tikhonchuk[98] looks specifically at the toroidal mode when
893 considering shear Alfvén waves. Does the poloidal mode count as compressional even
894 when it's guided? In his 2001 paper, Lysak[62] talks about how circularly-polarized
895 waves might be interesting. That would be a superposition of the poloidal and toroidal
896 modes, right? In that paper, he's looking at modes with frequencies of 1 Hz or so, in
897 the context of the IAR. Lysak and Song's 2003 paper[63] looks at the toroidal mode,
898 also in the IAR (?).

899 Notably, the Poynting flux waveforms are rectified — they primarily carry energy Earth-
900 ward. The current, on the other hand, alternates between upward and downward flow.
901 This effect presumably arises because the current is a linear quantity while the Poynting
902 flux is quadratic: the electric and magnetic fields that make it up oscillate in phase, so
903 their product is positive even when they are negative.

904 The magnitude of the parallel current tops out over $1 \mu\text{A}/\text{m}^2$, just shy of the up-to-tens
905 of $\mu\text{A}/\text{m}^2$ inferred from ground observations and seen in situ[9, 47, 85].

Current and Poynting Flux at 1000km: Quiet Day , 16mHz Current

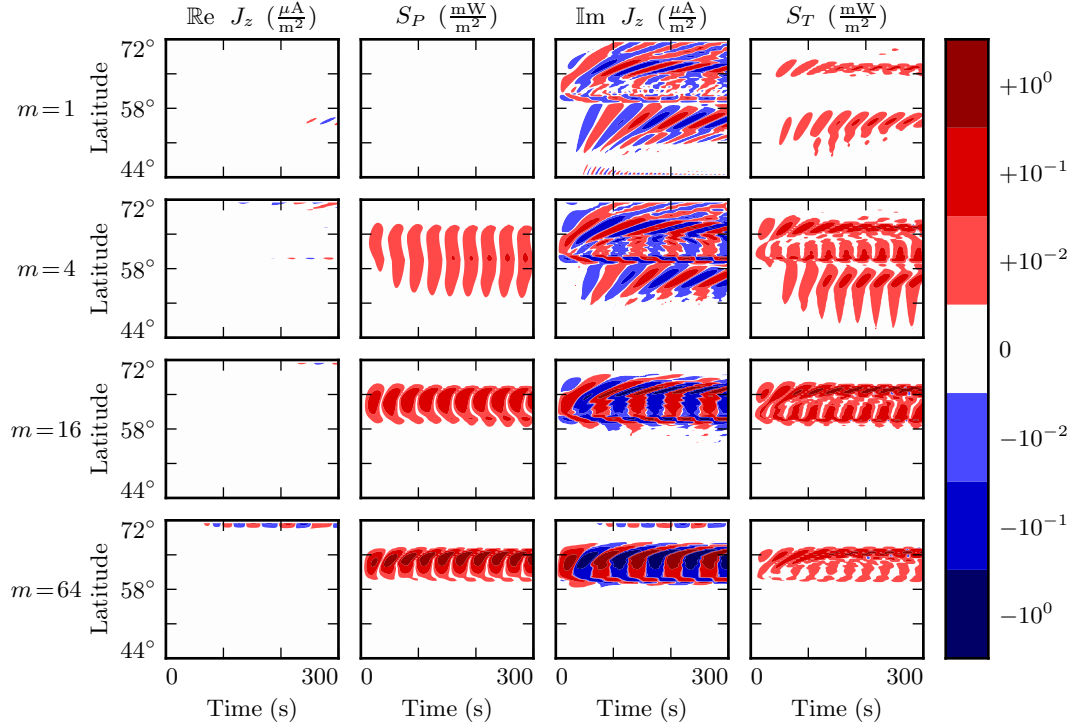


Figure 6.4: The above figure shows the same runs as Figure 6.3, except that the slices are taken at an altitude of 1000 km instead of 100 km. Morphological similarities are still evident between the imaginary parallel current and the toroidal Poynting flux. However, without the Hall conductivity to couple the modes, the poloidal mode does not appear to carry significant current along the field line.

It's also possible to consider the effect of parallel currents and electric fields on the ionosphere's energy budget, per Poynting's theorem:

$$\frac{\partial}{\partial t} u = -\nabla \cdot \underline{E} - \underline{J} \cdot \underline{E} \quad (6.7)$$

906 As shown in Figure 6.5, little energy transfer in the ionosphere is mediated by perpendicular components of the Poynting flux. The parallel component of $\underline{J} \cdot \underline{E}$ is comparably
 907 unimportant. The energy deposited in the ionosphere by the Poynting flux matches
 908 closely with the energy lost to Joule dissipation — as it should, to conserve energy
 909

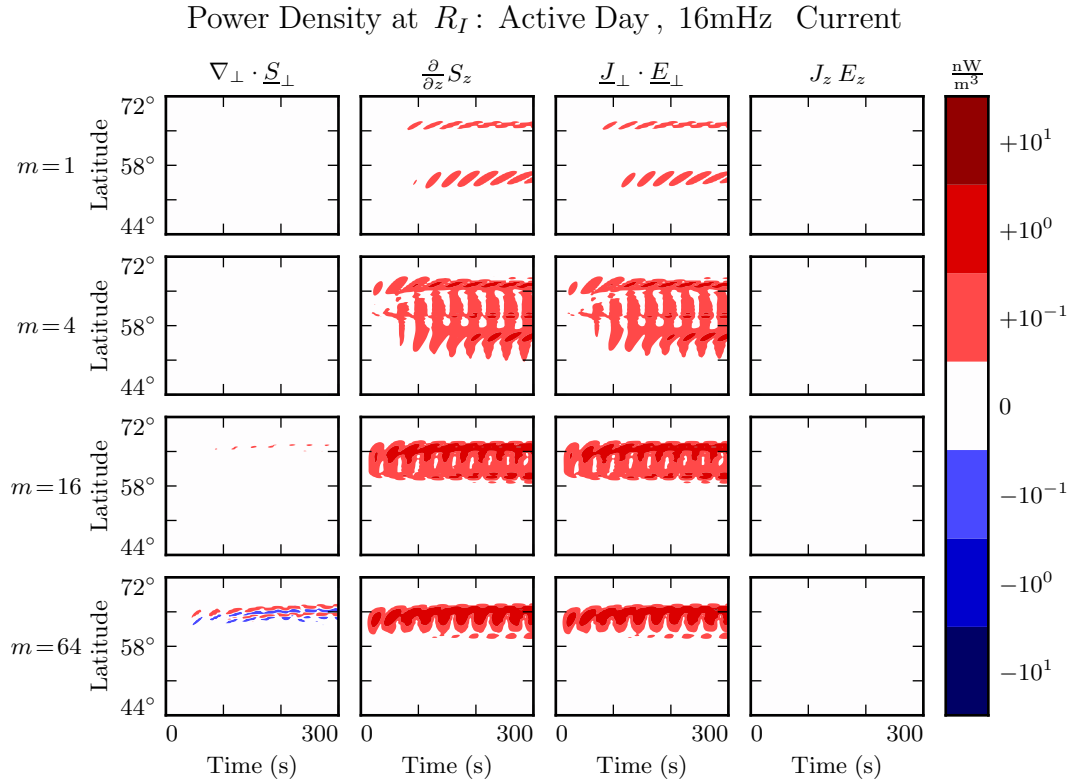


Figure 6.5: While field-aligned currents can be of significant size, they are not particularly good at depositing energy in the ionosphere. Energy deposited by the Poynting flux matches closely with Joule dissipation from the perpendicular currents, while $J_z E_z$ is smaller by several orders of magnitude.

910 — but according to the model, parallel currents and electric fields do not contribute
 911 significantly.

912 6.3 Inertial Length Scales

913 It's not quite fair to compare the parallel and perpendicular contributions to $\nabla \times \underline{E}$ as
 914 is done in Section 6.2. Perpendicular electric fields are on the order of 1 mV/m, with
 915 wavelengths on the order of 10^5 km; they cause magnetic fields to change at a rate of

916 around 0.1 nT/s. Parallel electric fields, closer to 10^{-6} mV/m, would need to vary over
 917 length scales of 0.1 km to match with that.

918 Such scales are believable. The characteristic length scale of the plasma oscillation is
 919 the electron inertial length, $\frac{c}{\omega_P}$, which is on the order of 1 km in the auroral ionosphere
 920 and 0.1 km in the low-altitude plasmasphere. However, Tuna's usual grid doesn't resolve
 921 structures so fine; its resolution bottoms out closer to 10 km. That is, with the inclusion
 922 of electron inertial effects, Tuna's grid is too coarse to resolve all of the waves expected
 923 to be present. The model is prone to instability as a result.

924 Figure 6.6 shows a run with perpendicular resolution smaller than the electron inertial
 925 length, side by side with an analogous run on the usual grid. In order to carry out
 926 the inertial-scale run, several concessions were made to computational cost. The run
 927 simulates only a duration of 100 s (other figures in the present chapter, and those in
 928 Chapter 7, show 300 s), and the grid covers only the auroral latitudes from $L = 5$ to
 929 $L = 7$.

Parallel Electric Fields: Quiet Day, 100s of 16mHz Current, $m = 16$

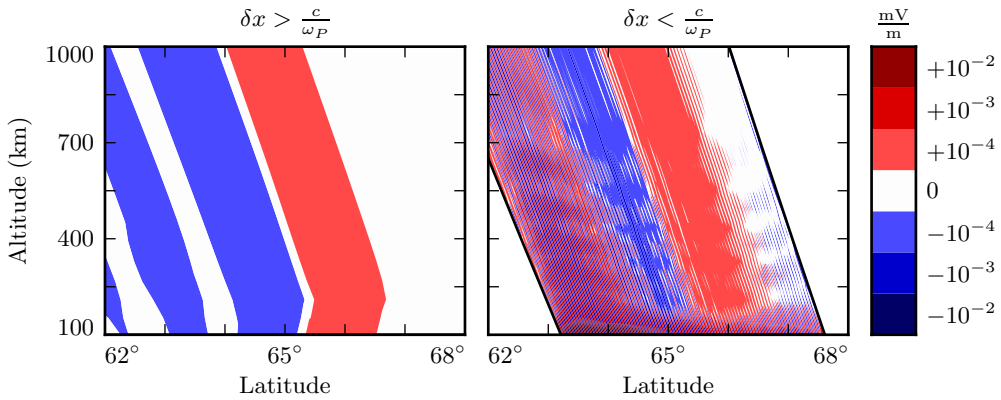


Figure 6.6: The parallel electric field develops significant structure when the perpendicular grid resolution is smaller than the electron inertial length. Unfortunately, such runs are prohibitively expensive. The subplot on the right — which still fails to resolve wave structure properly — represents a 100-fold increase in computational time.

930 Even so, the run presents a significant computational expense. Spread over 16 cores, a
931 100s run on Tuna’s usual grid takes well under an hour. The inertial-scale run barely
932 finished in 96 hours, the cutoff at the Minnesota Supercomputing Institute⁷.
933 The snapshot shown in Figure 6.6 uses a perpendicular grid resolution of 0.7 km at the
934 Earthward edge, which just satisfies the Nyquist rate for the minimum inertial length
935 of 1.7 km. It’s still too coarse. There is clearly some small-scale structure developing in
936 the ionosphere, but it’s not well resolved. The large number of “wiggles” portends an
937 imminent crash.

938 6.4 Discussion

939 The present chapter is a proof of concept: the addition of electron inertial effects to
940 Tuna presents a promising first-principles-based approach to the investigation of parallel
941 currents and electric fields associated with field line resonances. Electric fields arise
942 which are consistent in magnitude with those predicted by the dispersion relation, and
943 parallel currents fall within an order of magnitude or so of observed values, even when
944 inertial length scales are not properly resolved.
945 Results in Section 6.2 suggest a disparity between poloidal and toroidal FLRs in terms of
946 the parallel current response. At low altitude, where the two modes are directly coupled
947 by the Hall conductivity, both seem to be accompanied by parallel currents. However, in
948 regions of low Hall conductivity, parallel currents appear to preferentially accompany
949 toroidal waves. The cause is unclear, and a topic worthy of future investigation.
950 Future work in this vein may also consider the scales and structures that arise in regions
951 of parallel current. For example, one might consider the relationship between the dy-
952 namic height-integrated potentials and the accompanying parallel currents, specifically
953 with respect to the Knight Relation[52]. Inertial effects could furthermore be accom-
954 panied by test particles, in order to gauge the properties of particle precipitation that
955 could accompany global Alfvénic potential structures.

⁷Runtime goes as the inverse square of grid resolution. Not only does finer resolution require more grid cells, but it also gives rise to proportionally smaller crossing times, imposing a smaller time step.

956 Unfortunately, simulations are prone to instability when inertial length scales are not
957 properly resolved. And, at least at present, resolving those scales poses a prohibitive
958 computational expense. For this reason, the consideration of inertial effects is limited to
959 the present chapter; results in Chapter 7 make use of the core version of Tuna presented
960 in Chapter 5, which does not include the effects of electron inertia.

961 Notably, the addition or omission of parallel currents and electric fields does not appear
962 to significantly alter the behavior of perpendicular electric fields or magnetic fields.
963 Because the parallel electric fields are relatively small, $\nabla \times \underline{E}$ is essentially unaffected
964 by their inclusion.

965 **Chapter 7**

966 **Numerical Results**

967 A primary motivation for the development of Tuna is the fact that FLRs vary in interesting ways as a function of azimuthal modenumber, and that existing numerical models
968 are limited in their ability to examine such behaviors. The present chapter discusses
969 the core results that have so far been obtained.
970

971 **7.1 Modenumber and Compression**

972 It's well known that the poloidal FLR mode is compressional at low modenumber,
973 but guided at high modenumber. However, the relationship is not well quantified.
974 Theoretical work has historically been concerned with the limits $m \rightarrow 0$ and $m \rightarrow$
975 ∞ [16, 81], and only a handful of satellite observations have explicitly considered an
976 event's azimuthal modenumber[19, 73, 93]. Using results from Tuna, the present section
977 examines the strength of the poloidal wave's compressional component at an ensemble
978 of finite modenumbers.

979 Figures 7.1 and 7.2 show magnetic field snapshots taken from a pair of runs. The first
980 uses a small azimuthal modenumber, and the second uses a large one. The runs are
981 otherwise identical: both simulations use the quiet dayside ionospheric profile, and both
982 are driven at 22 mHz.

983 The differences between the two runs are striking. At low modenumber, wave activity
984 is visible throughout the simulation domain. Structure in the poloidal magnetic field is
985 only vaguely governed by the dipole geometry, and the compressional magnetic field is
986 comparably strong to the two perpendicular components.

987 In contrast, at high modenumber, the poloidal magnetic field is localized to the L -shells
988 where the driving is delivered: $4 \lesssim L \lesssim 6$. The compressional field is weaker than
989 the poloidal field by at least an order of magnitude. A third-harmonic poloidal mode
990 is visible at the outer boundary — its magnitude is just barely large enough to be
991 visible on the logarithmic scale. The gap between $L \sim 5$ (where 22 mHz matches a first-
992 harmonic FLR) and $L \sim 10$ (where 22 mHz matches a third-harmonic FLR) speaks to
993 the evanescence of non-guided waves above the compressional Alfvén cutoff frequency¹.

994 In both the low- m and high- m runs, toroidal activity is more or less coincident with
995 poloidal activity — as is to be expected, since the driving is purely poloidal, and the
996 poloidal mode rotates to the toroidal mode over time. It is further notable that the
997 toroidal mode is sharply guided. Particularly in Figure 7.2, strong, narrow, toroidal
998 FLRs of opposite phase can be seen oscillating very close to one another. Strong poloidal
999 waves, in contrast, are smeared in L .

1000 Snapshots are not shown for runs carried out using the other ionospheric profiles (active
1001 day, quiet night, and active night). The morphology of their waves is qualitatively
1002 similar. The differences between the profiles is considered in Sections 7.2 to 7.4.

1003 Figure 7.3 quantifies the compressional component of the poloidal mode as a function of
1004 modenumber. Each subplot corresponds to a different run of Tuna — the runs shown in
1005 Figures 7.1 and 7.2 are in the rightmost column, second from the top and second from the
1006 bottom respectively. The red line indicates the ratio between the RMS compressional
1007 magnetic field and the RMS poloidal magnetic field; both averages are taken over the
1008 entire simulation “volume” each time step. Mean values are shown in black.

¹See Section 4.4.

1009 At $m = 1$, the compressional and poloidal magnetic fields are comparable in magnitude.
1010 As m increases, however, the compressional component quickly falls off. The compres-
1011 sional component is half the strength of the poloidal component at $m \sim 5$, and a quarter
1012 by $m \sim 10$.

1013 A slight frequency dependence is apparent across each row in Figure 7.3. Compressional
1014 coupling falls off slower for waves at higher frequency. This is because higher-frequency
1015 waves are that much closer to the cutoff frequency (described in Section 4.4), and so
1016 their propagation across L -shells is that much less evanescent.

1017 Similarly, poloidal waves are more prone to compression on the nightside. Due to the
1018 higher Alfvén speed on the nightside, driving is delivered at $L \sim 6$ instead of $L \sim 5$. The
1019 cutoff frequency depends inversely on radial distance. For nightside runs (not shown),
1020 $\left| \frac{B_z}{B_x} \right|$ falls to 50% at $m \sim 8$ and to 25% at $m \sim 16$.

1021 Notably, the waves considered in the present work are fundamental harmonics. The
1022 compressional behavior of the poloidal mode may vary for the (more-common) second
1023 harmonic: Radoski suggests that the asymptotic value of $\left| \frac{B_z}{B_x} \right|$ is inversely proportional
1024 to the harmonic number[81].

Magnetic Field Snapshots: Quiet Day , 22mHz Current, $m = 2$

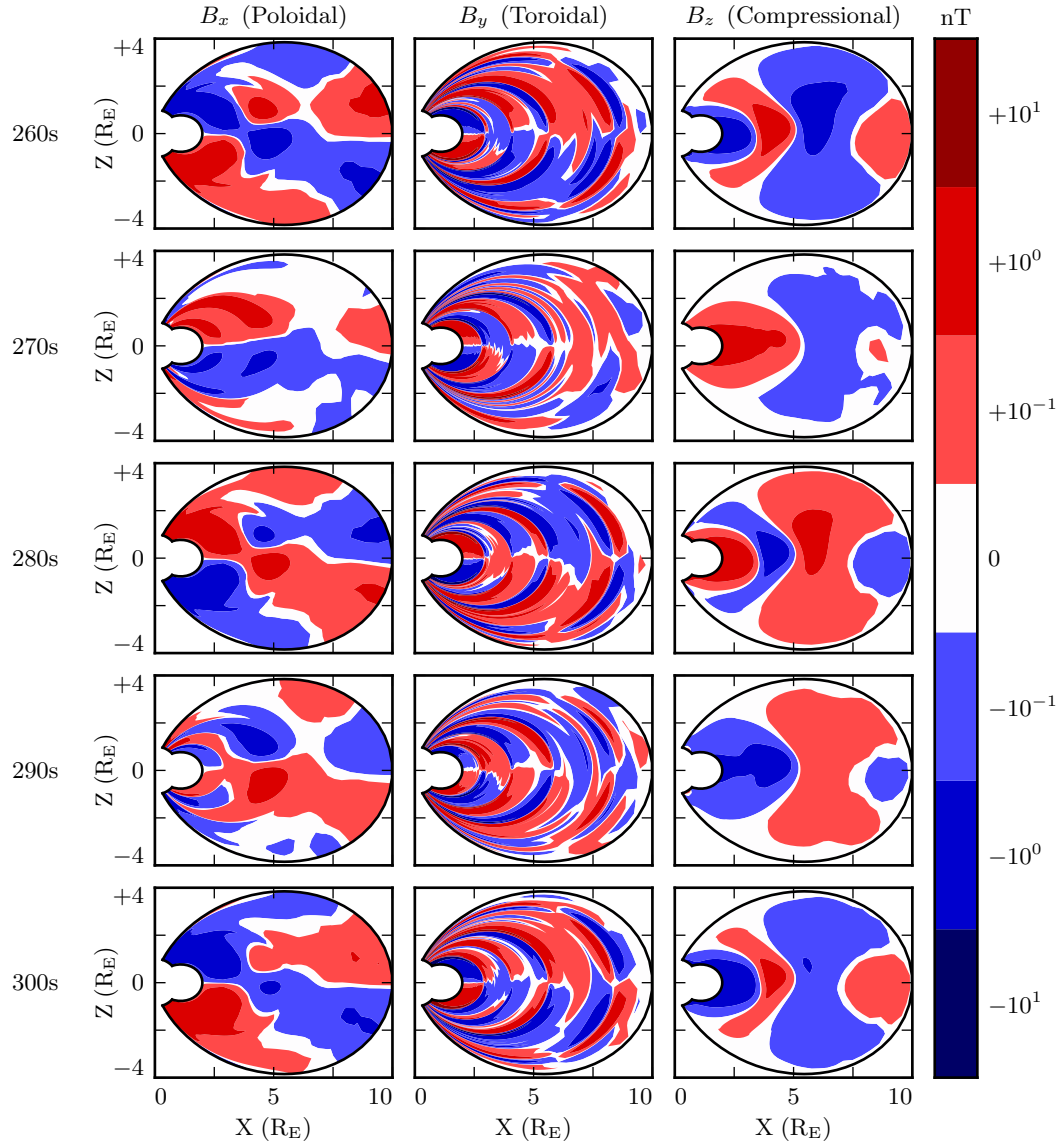


Figure 7.1: Each row in the above figure is a snapshot in time. The three columns show the simulated poloidal, toroidal, and compressional magnetic field. Due to the run's low azimuthal modenumber, the poloidal mode has a significant compressional component. This is visible both in the fact that B_z is comparable in size to B_x , and in that structure in B_x is only vaguely guided by the geometry of the magnetic field. Toroidal waves, in contrast, are sharply guided.

Magnetic Field Snapshots: Quiet Day , 22mHz Current, $m = 32$

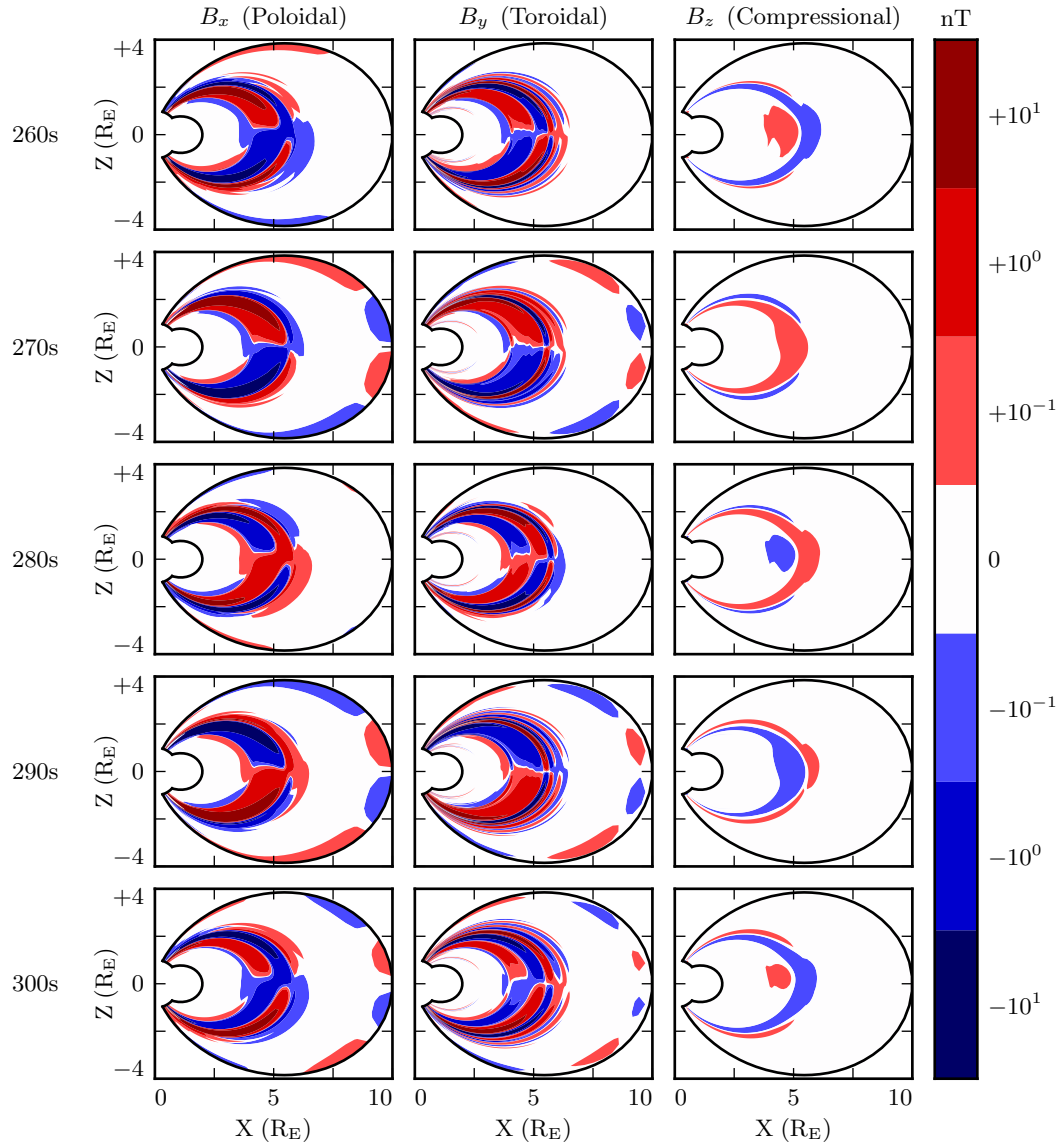


Figure 7.2: The above figure is analogous to Figure 7.1, but the runs use a larger azimuthal modenumber. The change has a dramatic effect. The poloidal wave is concentrated much more sharply in L , and its compressional component is weakener by an order of magnitude. Regardless of modenumber, toroidal waves exist at a range of L shells similar to poloidal waves, and show sharp definition across L -shells.

Compressional Coupling to the Poloidal Mode: Quiet Day

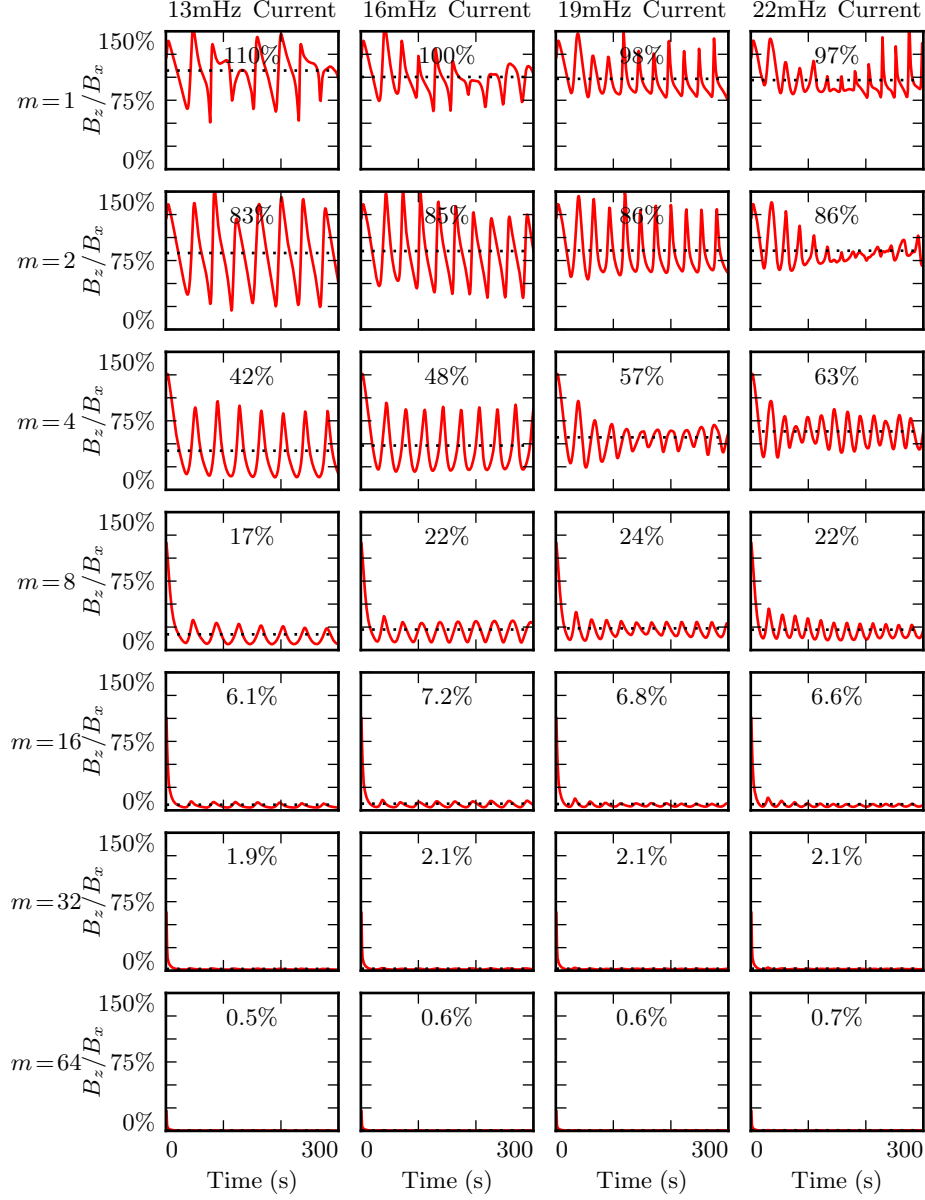


Figure 7.3: Each subplot above corresponds to a different run; the runs shown in Figures 7.1 and 7.2 are in the rightmost column, second from the top and second from the bottom respectively. Red lines indicate the ratio between the RMS compressional and poloidal magnetic fields. Mean values are shown in black. The compressional field is comparable to the poloidal field at $m = 1$, but falls quickly.

1025 **7.2 Resonance and Rotation on the Dayside**

1026 In his 1974 paper, Radoski argues that a poloidally-polarized wave should asymptotically
1027 rotate to the toroidal polarization[81] as a result of the curved derivative in the meridional plane. The question of finite poloidal lifetimes is considered further in a 1995
1028 paper by Mann and Wright[67]. Their numerical work used a straightened field line,
1029 with an Alfvén speed gradient in the “radial” direction. They also found a rotation over
1030 time from poloidal to toroidal polarization, with the characteristic time proportional to
1031 the azimuthal modenumber.
1032

1033 The present section builds on the aforementioned results by relaxing several of their non-
1034 physical assumptions. Tuna’s geometry is more realistic than Radoski’s half-cylinder or
1035 the box model used by Mann and Wright. Previous work has considered the evolution
1036 of an initial condition, while the simulations shown below include driving delivered
1037 over time. In addition, Tuna features a finite, height-resolved ionospheric conductivity
1038 profile, rather than the perfectly-reflecting boundaries used in the past.

Each subplot in Figure 7.4 is analogous to Figure 3 in Mann and Wright’s paper[67]. Blue lines show the total energy in the poloidal mode as a function of time. Red lines show toroidal energy. Runs are organized analogous to those in Figure 7.3: drive frequency is constant down each column, and azimuthal modenumber is constant across each row. Axis bounds are held constant across all subplots. The poloidal and toroidal energy are computed by integrating over the electromagnetic energy density, per Poynting’s theorem:

$$U_P = \int \frac{dV}{2\mu_0} \left(B_x^2 + \frac{1}{v_A^2} E_y^2 \right) \quad U_T = \int \frac{dV}{2\mu_0} \left(B_y^2 + \frac{1}{v_A^2} E_x^2 \right) \quad (7.1)$$

1039 Where the differential volume dV is computed using the Jacobian² to account for Tuna’s
1040 unusual geometry. The integral is evaluated in u^1 and u^3 but not u^2 (Tuna’s missing
1041 half-dimension), which gives energy in units of gigajoule per radian. More than anything
1042 else, this serves as a reminder that Pc4 pulsations are localized in MLT.

²See Section 5.1.

1043 The 28 runs shown in Figure 7.4 use an ionospheric profile corresponding to the dayside
1044 during times of low solar activity, where the conductivity is relatively high. The active
1045 and quiet dayside profiles are briefly contrasted in Section 7.4; for the most part, the
1046 focus of the present work is on the difference between the dayside and the nightside
1047 (Section 7.3). Differences between the two dayside profiles are small in comparison.

1048 The fact that red (toroidal) lines appear at all in Figure 7.4 speaks to a net rotation
1049 of energy from the poloidal mode to the toroidal. As discussed in Section 5.3, Tuna's
1050 driving is delivered purely into the poloidal electric field (reflecting a perturbation in
1051 the magnitude of the ring current).

1052 As expected, the rotation from poloidal to toroidal is slowest at large azimuthal mode-
1053 numbers. The toroidal energy overtakes the poloidal energy within a single drive period
1054 at $m = 4$; at $m = 64$, the most of the energy is in the poloidal mode for ~ 10 periods.
1055 However, the relationship between azimuthal modenumber and rotation timescale is
1056 not linear, as was suggested by Mann and Wright. Instead, in a practical setting, the
1057 rotation is fastest at $m \sim 4$.

1058 This is explained by the compressional character of the poloidal mode. At very low
1059 modenumber, energy in the poloidal mode moves readily across L -shells. A significant
1060 fraction of that energy is lost to the outer boundary before rotating to the toroidal
1061 mode. At high modenumber — as discussed in Section 7.1 — compressional propagation
1062 is evanescent, so all energy in the poloidal mode must ultimately rotate to the toroidal
1063 mode or be lost to Joule dissipation.

1064 Joule dissipation is a major player in the system's energy economy. However, due to the
1065 highly conductive dayside ionosphere, dissipation timescales are in the tens of Pc4 wave
1066 periods. Energy loss through Joule dissipation asymptotically balances energy input
1067 from driving, but most of that energy is not lost until after it has rotated from the
1068 poloidal mode to the toroidal. As such, in most runs shown in Figure 7.4, the energy
1069 content of the toroidal mode asymptotically exceeds that of the poloidal mode.

1070 The asymptotic energy content of the system also depends on how well the drive fre-
1071 quency matches the local eigenfrequency. If the two do not match, energy is lost to
1072 destructive interference between the standing wave and the driving.

1073 In principle, energy moves between the poloidal and toroidal modes due to their direct
1074 coupling through the ionospheric Hall conductivity. In practice, this effect is small.
1075 When the runs shown in Figure 7.4 are repeated with the Hall conductivity set to zero,
1076 the resulting energy curves are not visibly different.

1077 The low- m runs at 19 mHz merit additional discussion. These runs accumulate energy
1078 over a large number of wave periods, while the low- m waves at 13 mHz, 16 mHz, and
1079 22 mHz do not. This effect is likely nonphysical. At 19 mHz, a third-harmonic resonance
1080 forms very close to the outer boundary. The resonance is likely enhanced by nonphysical
1081 reflections against the simulation’s boundary conditions.

1082 The presence of individual harmonics can be seen in the contours shown in Figures 7.5
1083 and 7.6. These figures show the same runs as Figure 7.4, arranged in the same way on
1084 the page. However, instead of showing the total energy integrated over the simulation
1085 domain, the energy densities are averaged over the volume of each flux tube individually.
1086 Figure 7.5 shows contours of poloidal energy density and Figure 7.6 shows toroidal
1087 energy density.

1088 The top few rows of Figure 7.5 confirm that the poloidal mode’s compressional nature is
1089 to blame for its failure to accumulate energy at low modenumber. Waves move so readily
1090 across field lines that no visible amount of energy builds up at $L \sim 5$, the location of the
1091 driving. Some energy moves inward, and is trapped by the peak in Alfvén speed just
1092 inside the plasmapause, while the rest moves to the outer boundary. The time spent
1093 moving across field lines counts against the poloidal mode’s finite lifetime, inhibiting
1094 the buildup of poloidal energy density even at L -shells where the wave matches the local
1095 eigenfrequency.

1096 As m increases, the energy distribution becomes more concentrated in L , though indi-
1097 vidual features remain fairly broad. At $m = 8$, runs at 13 mHz and 16 mHz are inclined
1098 to build up energy just inside the plasmapause, while those at 19 mHz and 22 mHz res-
1099 onate just outside the plasmapause; in all four cases, the energy is spread over a range
1100 of at least 1 in L .

1101 The peak energy density in the bottom-right run (22 mHz driving, $m = 64$) is by far the
1102 largest of any run in Figure 7.5. The azimuthal modenumber is large, so the poloidal

1103 mode is purely guided; energy is not smeared across multiple L -shells. And, crucially, the
1104 frequency of the driving matches closely with the Alfvén frequency at $L \sim 5$. Other runs
1105 on the bottom row are also guided, but they reach lower asymptotic energy densities
1106 because of a mismatch between the drive frequency and the local eigenfrequency —
1107 resulting in destructive interference between the standing wave and its driver.

1108 The eigenfrequencies in the magnetosphere are significantly affected by the location of
1109 the plasmapause. When the runs in Figure 7.5 are repeated with the plasmapause at
1110 $L = 5$ instead of $L = 4$, the strongest resonance at $L \sim 5$ drops from 22 mHz to 16 mHz
1111 (not shown).

1112 Whereas the poloidal contours are smeared over a swath of L -shells (though the high- m
1113 runs less so), the toroidal contours in Figure 7.6 appear only where the wave frequency
1114 matches the local eigenfrequency. A horizontal line drawn through the Alfvén speed
1115 frequency profiles (recall Figure 3.1) intersects the profile up to three times: once as
1116 the Alfvén frequency drops through the Pc4 range from its low-latitude peak, again as
1117 the Alfvén frequency rises sharply at the plasmapause, and a third time as the Alfvén
1118 frequency drops asymptotically. Toroidal waves can be seen resonating at all three of
1119 these locations in the $m = 4$, 22 mHz run in Figure 7.6, along with a third harmonic at
1120 large L . This is consistent with observations: toroidal resonances are noted for having
1121 frequencies which depend strongly on L , in contrast to the poloidal mode's less-strict
1122 relationship between frequency and location.

1123 In only one of the runs shown in Figure 7.5 does the poloidal mode attain an energy
1124 density on the order of 10^{-1} nJ/m³. On the other hand, the toroidal mode reaches
1125 $\sim 10^{-1}$ nJ/m³ in six of the runs in Figure 7.6. That is, the poloidal mode only exhibits
1126 a high energy density on the dayside only when conditions are ideal; the toroidal mode
1127 isn't nearly so particular.

Poloidal (Blue) and Toroidal (Red) Energy: Quiet Day

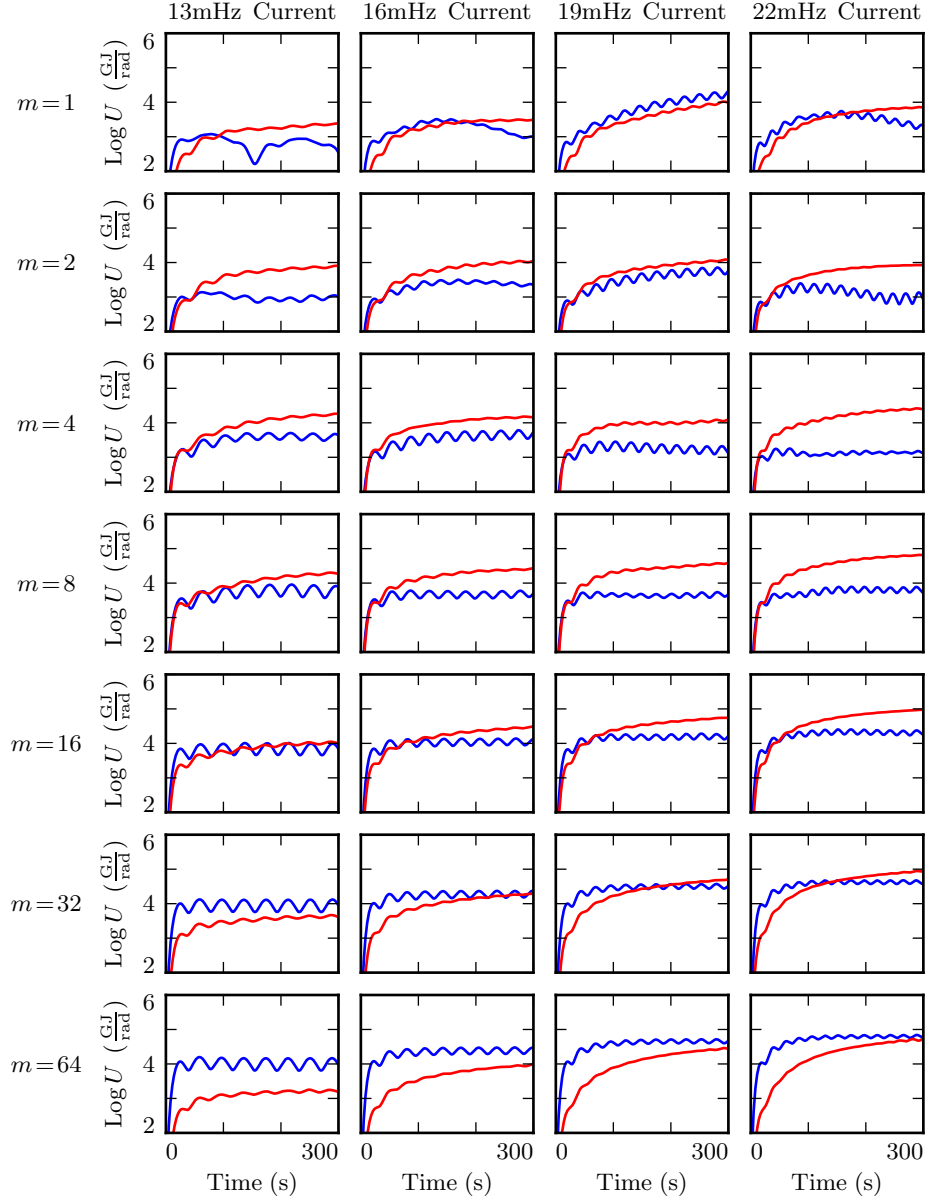


Figure 7.4: Each subplot above shows the poloidal (blue) and toroidal (red) energy for a simulation as a function of time. Each row contains four simulations, each with the same azimuthal modenumber; the seven rows in each column share a drive frequency. Driving is purely poloidal, but energy rotates asymptotically to the toroidal mode, and rotation is slowest at high modenumber.

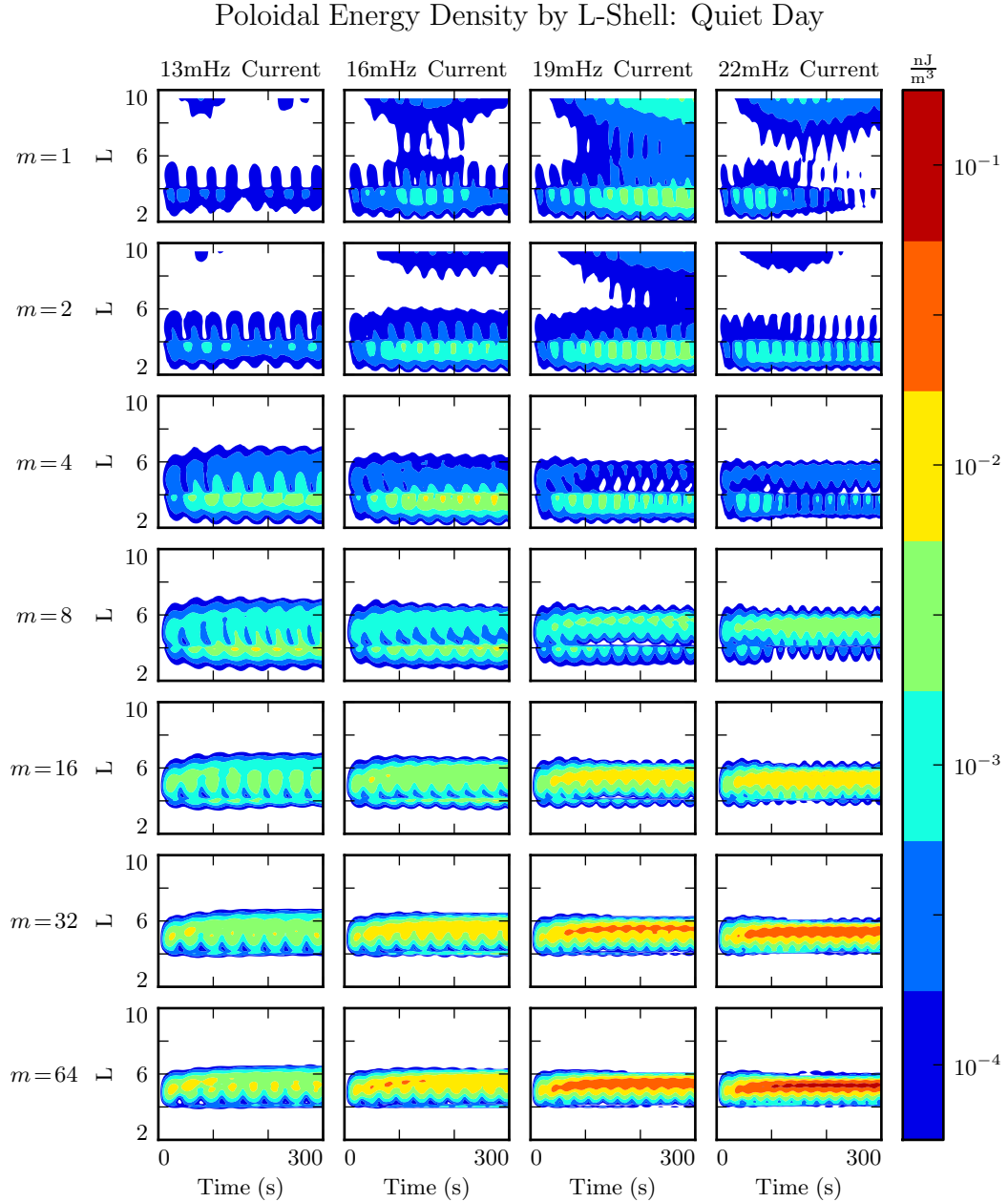


Figure 7.5: At low modenumber (top rows), the compressional nature of the poloidal mode allows energy to escape the simulation. At high modenumber (lower rows), the poloidal mode is guided; energy is trapped at the L -shell where it's injected, and rotation to the toroidal mode is slow — ideal conditions for resonance. But energy buildup is lackluster except where the drive frequency matches the local eigenfrequency (best in the rightmost row).

Toroidal Energy Density by L-Shell: Quiet Day

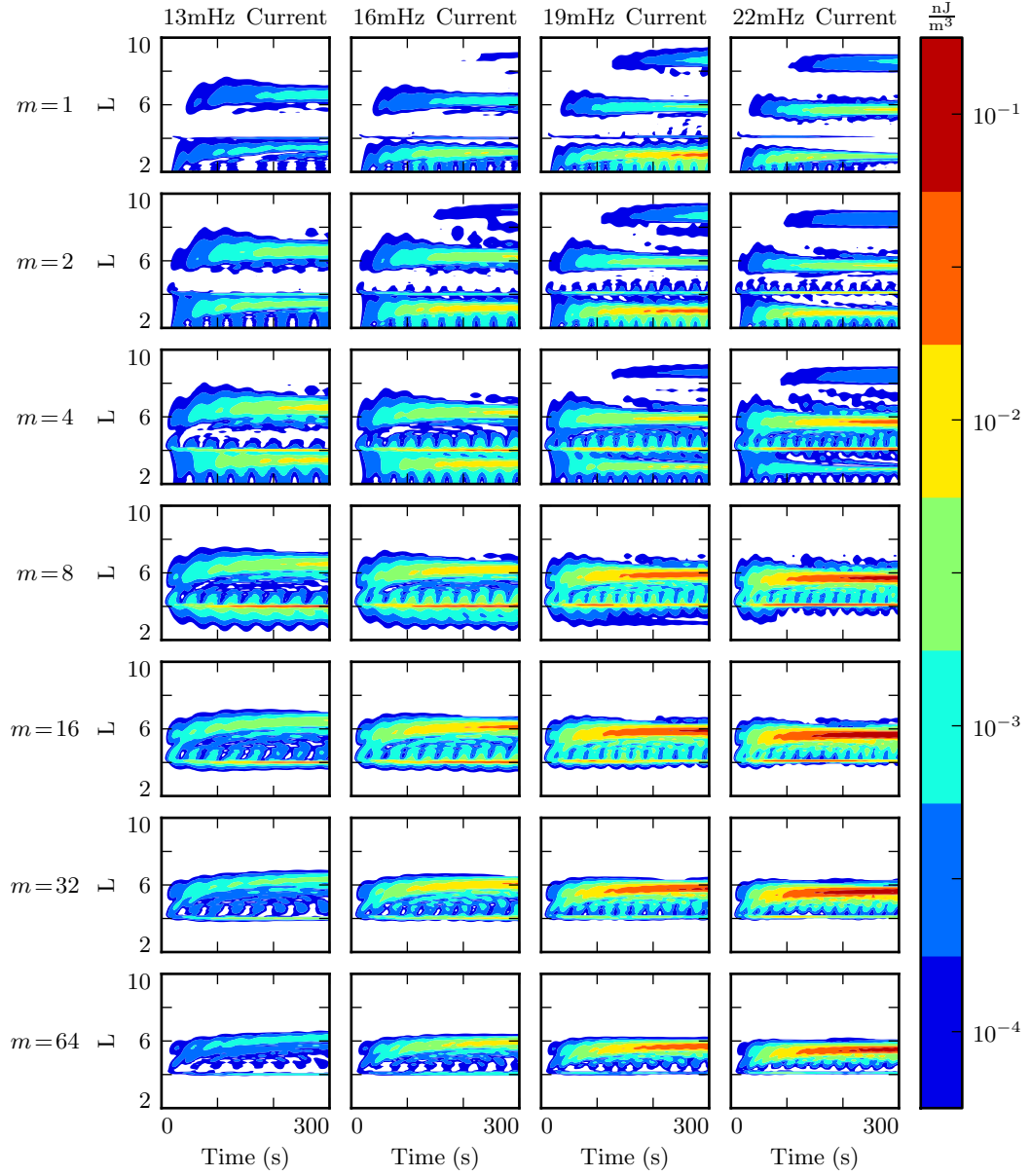


Figure 7.6: Whereas the poloidal mode is smeared in L due to its compressional nature, the toroidal mode is focused at L shells where it's resonant. In general, when the conductivity is high, the toroidal mode also exhibits a higher asymptotic energy density than the poloidal mode (Figure 7.5).

1128 **7.3 Resonance and Rotation on the Nightside**

1129 Compared to the dayside ionosphere employed in Section 7.2, the nightside exhibits two
1130 major differences. The ionospheric conductivity is lower, and the Alfvén speed is higher.
1131 Runs in the present section specifically use Tuna’s ionospheric profile corresponding to
1132 the nightside during quiet solar conditions. Behavior on the active nightside is qualita-
1133 tively similar, though less drastic, since the conductivity on the active nightside is not
1134 so low. The two nightside profiles are briefly compared in Section 7.4, but for the most
1135 part the present work is concerned with the behavior of the nightside compared to that
1136 on the dayside.

1137 Other than the change in ionospheric profile, Figures 7.7 to 7.9 are analogous to Fig-
1138 ures 7.4 to 7.6. Each subplot corresponds to a different 300 s run of Tuna. Drive
1139 frequency is constant down each column, and azimuthal modenumber is constant across
1140 each row.

1141 The low conductivity on the nightside gives rise to strong Joule dissipation. Waves are
1142 damped out in just a few bounces, so asymptotic energy values are reached quickly.
1143 No combination of frequency and modenumber gives rise to the accumulation of energy
1144 over multiple drive periods.

1145 As on the dayside, rotation of energy from the poloidal to toroidal mode is fastest at
1146 $m \sim 4$. Unlike the dayside, however, dissipation on the nightside is fast compared to
1147 the rotation of energy to the toroidal mode. Toroidal energy does not asymptotically
1148 exceed the poloidal energy by a significant margin in any run. At $m = 64$, where the
1149 rotation timescale is slowest, no more than 10 % of the energy in the poloidal mode
1150 rotates to the toroidal mode before being lost.

1151 **TODO:** The damping on the quiet nightside is so severe that basically nothing resonates
1152 anywhere. Should we show the active nightside instead?

1153 **TODO:** Timescale is probably about like the dayside, about one period at low m and
1154 order of ten periods at high m .

Poloidal (Blue) and Toroidal (Red) Energy: Quiet Night

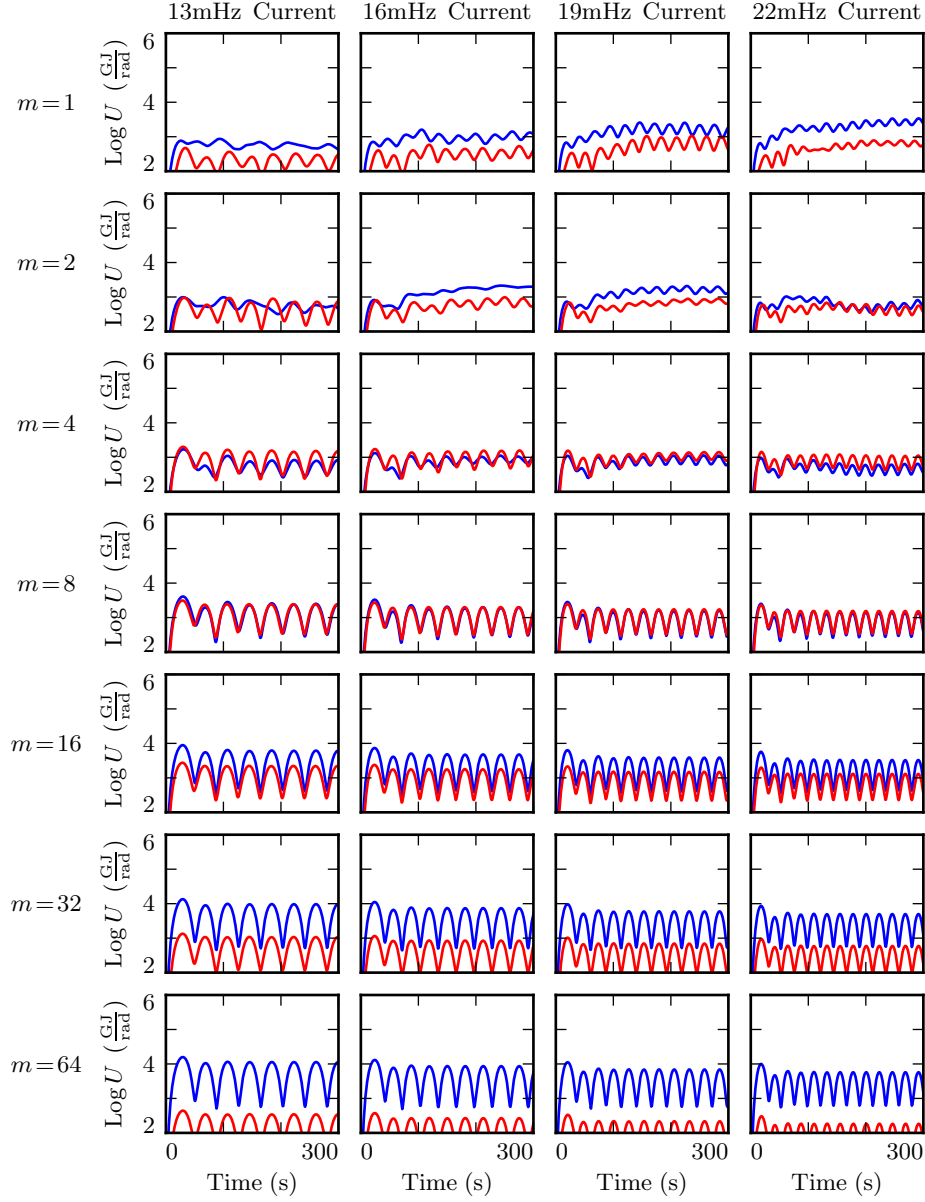


Figure 7.7: The energy content of each FLR on the nightside resembles that of a damped, driven oscillator. Energy is periodically added to the system, but most is lost too fast to rotate to the toroidal mode, particularly at high modenumber. There is no significant buildup of energy over multiple periods. Runs at $m = 1$ (top row) are an apparent exception, likely due to a nonphysical interaction with the boundary.

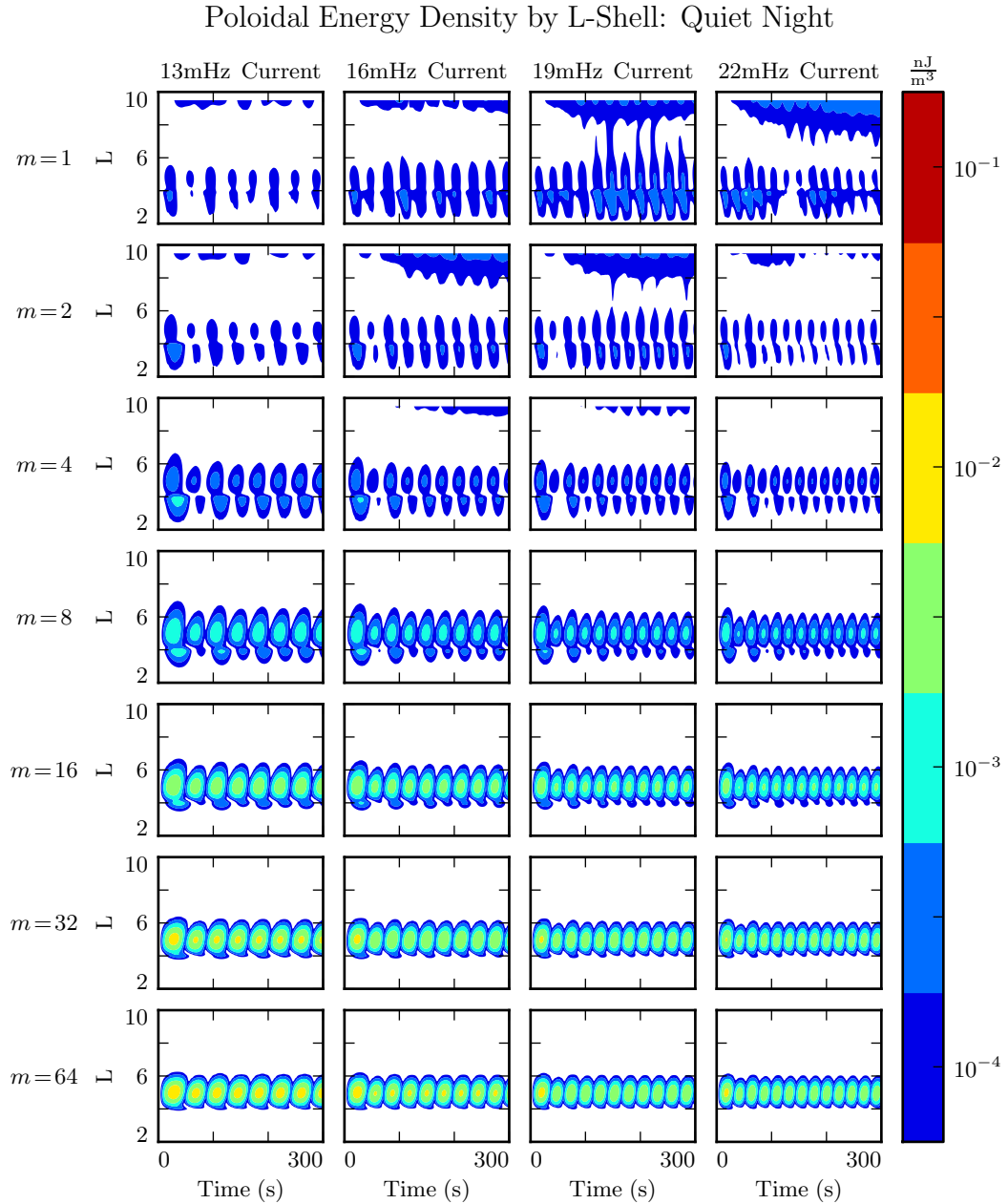


Figure 7.8: As on the dayside (Figure 7.8), low-modenumber poloidal waves (top rows) readily propagate across L -shells and escape the simulation domain. Energy density builds up most effectively at high modenumbers, where the poloidal mode is guided, and poloidal-to-toroidal rotation is slow. Even in this case, however, dissipation is fast enough to prevent energy from accumulating over multiple drive periods.

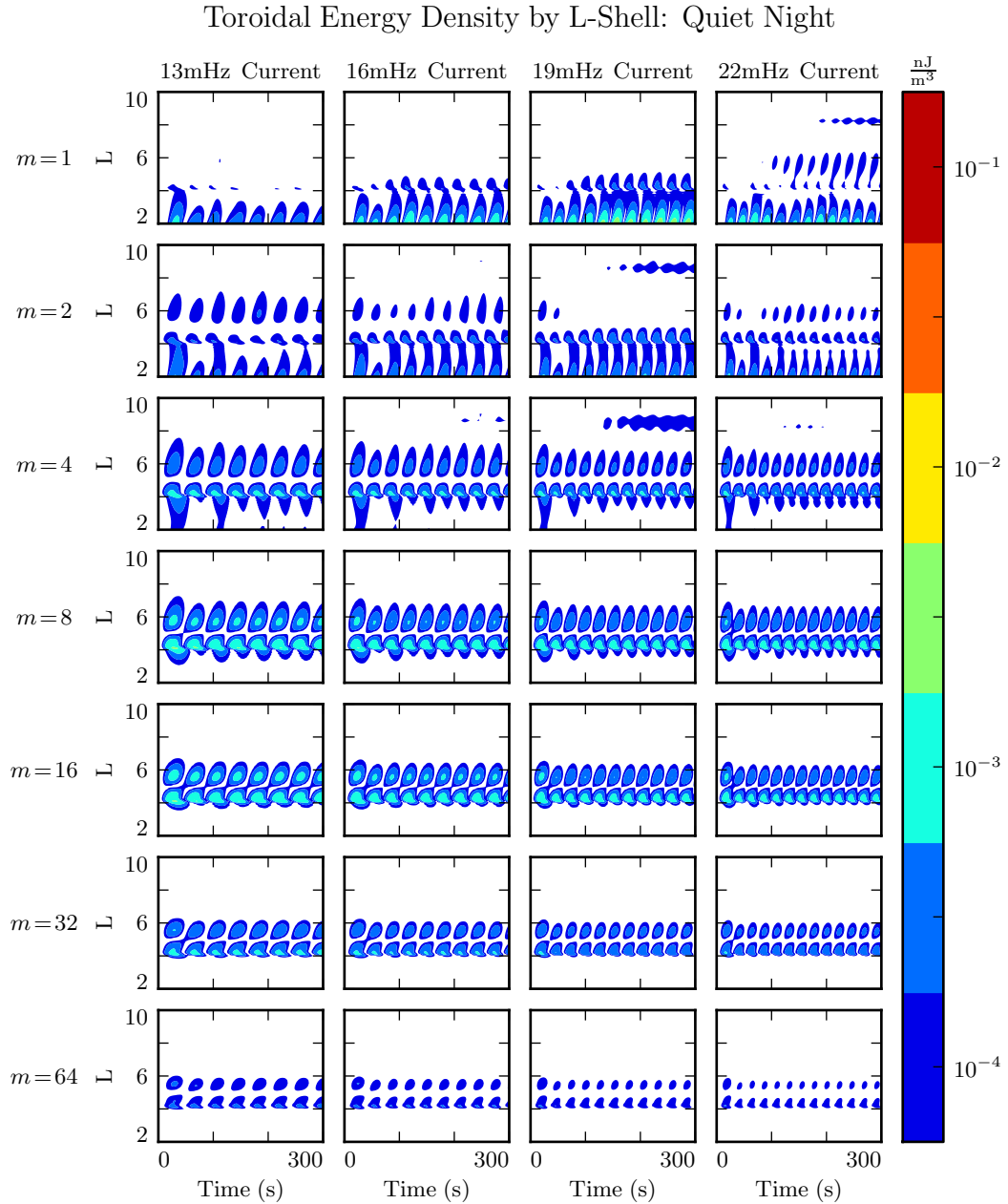


Figure 7.9: On the dayside (Figure 7.9), most energy rotates asymptotically to the toroidal mode. On the night side, the same is not true, since the poloidal mode quickly loses energy to Joule dissipation. At high modenumber, where the poloidal-to-toroidal rotation timescale is in the tens of wave periods, almost all of the energy is dissipated from the poloidal mode rather than rotating to the toroidal mode.

1155 **7.4 Ground Signatures and Giant Pulsations**

1156 While the majority of the action is in space, the majority of FLR observations have
1157 historically been ground-based. The present section explores the same simulations dis-
1158 cussed in Sections 7.2 and 7.3, but in terms of their ground signatures rather than their
1159 broad energy distributions.

1160 As in the figures shown in Sections 7.2 and 7.3, each row in Figures 7.10 and 7.11 shows
1161 runs at a different modenumber. The columns are magnetic field contours; the vertical
1162 axis is latitude, and the horizontal axis is time. The four columns are components of
1163 the magnetic field signatures at the ground: the north-south magnetic field (first and
1164 third columns) and the east-west magnetic field (second and fourth columns). The pair
1165 on the left show a simulation carried out using the active ionospheric profile, and the
1166 pair on the right show a simulation using the quiet profile.

1167 Notably, the magnetic polarization of a low frequency Alfvén wave is rotated by $\sim 90^\circ$ as
1168 it passes through the ionosphere[42]. The east-west field on the ground (B_ϕ) corresponds
1169 to the poloidal polarization in space, and the north-south field on the ground (B_θ)
1170 corresponds to the toroidal mode.

1171 The most striking feature of Figures 7.10 and 7.11 is the modenumber dependence.
1172 As modenumber increases, the magnetic field signatures become sharply localized in
1173 latitude. At high m , ground signatures are concentrated between 60° and 70° , peaking
1174 near 65° , roughly coincident with the foot point of the $L = 5$ field line.

1175 **TODO:** Is it weird that we see no ducting from the ionosphere? Does the ionosphere
1176 duct ULF waves in the θ direction, or just in ϕ ?

1177 At low modenumber, magnetic signatures are weak on the ground because the waves
1178 in space are also weak. At high modenumber, waves in space are strong, but so is
1179 the attenuation of magnetic signatures by the ionosphere³. The “sweet spot” at which
1180 magnetic ground signatures are maximized falls at $m = 16$ to $m = 32$.

1181 Tuna shows stronger ground signatures on the dayside than on the nightside, more or
1182 less in proportion with the difference in magnitude in space. Energy on the dayside

³See Equation (3.3).

1183 (which depends on field magnitude squared) peaks an order of magnitude larger than
1184 that on the nightside. Peak ground signatures on the dayside are larger by a factor of
1185 five: 45 nT compared to 10 nT. On both the dayside and the nightside, peak ground
1186 signatures are in B_ϕ , the east-west magnetic field component; both are also at $m = 16$,
1187 and both are seen in runs using the ionospheric profile for quiet solar activity.

1188 It's further notable that the ground signatures — particularly those on the nightside
1189 — exhibit a change in chirality based on latitude. At low latitude, B_θ leads B_ϕ , which
1190 creates a counterclockwise signature on the ground (in the northern hemisphere). At
1191 high latitude, the phase is reversed, resulting in a clockwise ground signature.

1192 These results match well with observations of giant pulsations, which tend to be east-
1193 west polarized, have a latitude-dependent chirality, and are most often observed near
1194 66° , with azimuthal modenumbers of 16 to 35, at the bottom of the solar cycle[96]. Pgs
1195 are most commonly observed pre-dawn, but dawn and dusk ionospheric profiles are not
1196 implemented for Tuna at present.

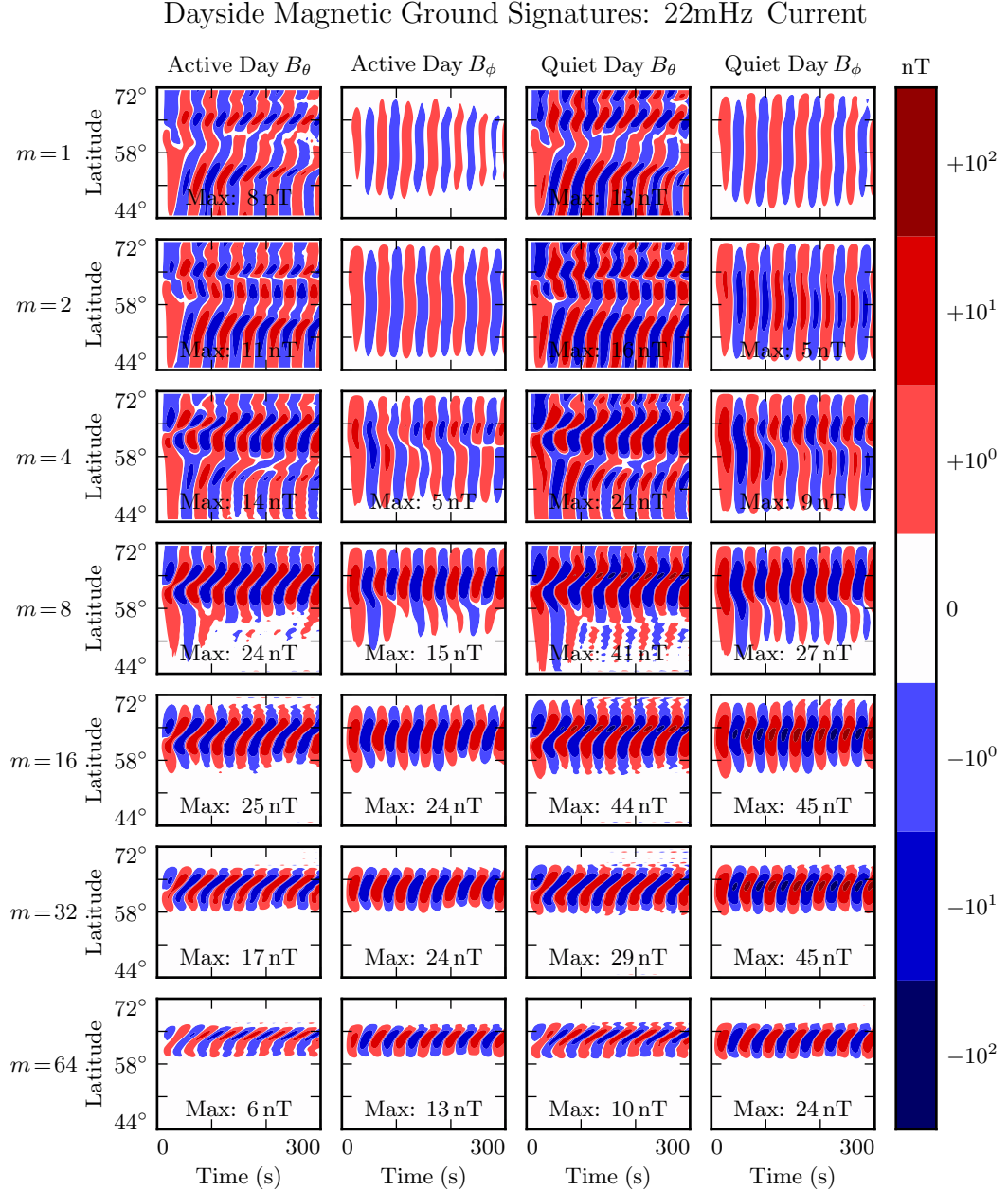


Figure 7.10: The magnetic ground signatures are shown for fourteen runs, two per row. Azimuthal modenumber is constant across each row. Polarization and ionospheric profile vary by column, per the headers. Ground signatures at low modenumber are not particularly strong because the waves in space are weak, while those at high modenumber are attenuated by the atmosphere. The “sweet spot” seems to fall around $m = 16$ to $m = 32$. Peak amplitudes above 3 nT are marked.

Nightside Magnetic Ground Signatures: 13mHz Current

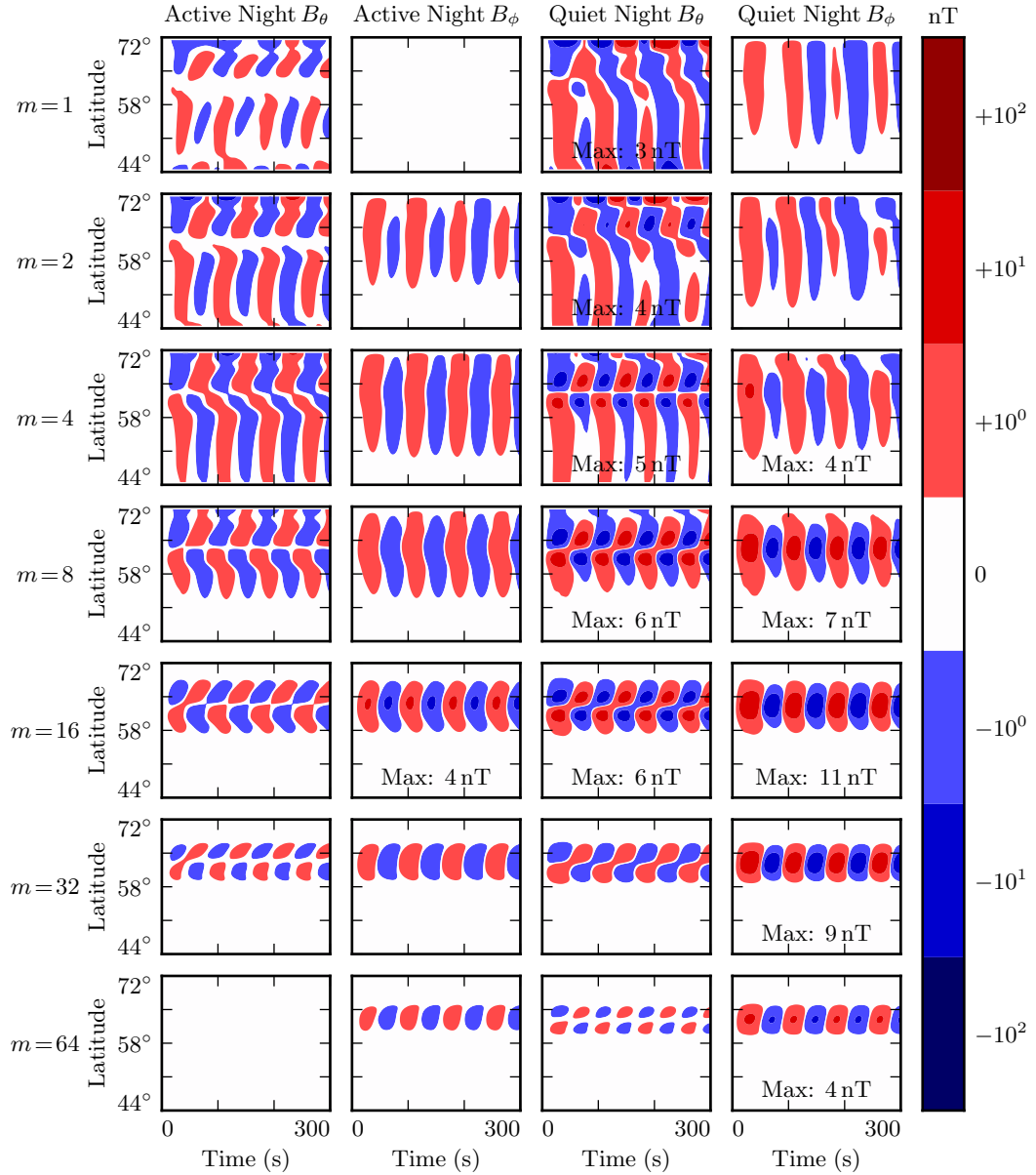


Figure 7.11: Nightside ground signatures are less strongly peaked than those on the dayside, but qualitative features are the same: the strongest signals are in B_ϕ , peaked over just a few degrees in latitude, at a modenumber of 16 or 32, under quiet ionospheric conditions.

1197 **7.5 Discussion**

1198 **TODO:** Make this section read nicely.

- 1199 Poloidal FLRs rotate to the toroidal mode over time. Toroidal modes do not appear to
1200 rotate back to the poloidal mode. When m is small, the rotation is comparable to an
1201 oscillation period; when m is large, rotation timescales are comparable to ten periods,
1202 sometimes more.
- 1203 On the dayside, little damping takes place over rotation timescales, so the toroidal mode
1204 asymptotically exceeds the toroidal mode. The exception is waves with low modenumber,
1205 where poloidal waves can escape by propagating across field lines. An evaluation
1206 of what happens then — whether they bounce back off the magnetopause, for example
1207 — is beyond the scope of the present work.
- 1208 On the nightside, the conductivity of the ionosphere is low enough that damping
1209 timescales become comparable to oscillation timescales. Waves are weaker, since they
1210 are unable to accumulate energy over as many periods. High- m toroidal waves are
1211 particularly weak, since the dissipation timescale is faster than the poloidal-to-toroidal
1212 rotation timescale.
- 1213 Waves resonate best when the frequency of the driving matches the local eigenfrequency
1214 where it's delivered. The eigenfrequency is significantly affected by the size of the
1215 plasmasphere.
- 1216 The poloidal mode, due to its compressional character, exhibits an energy profile which
1217 is smeared in L . The toroidal mode, on the other hand, forms sharp resonances where the
1218 drive frequency matches the local eigenfrequency. This may explain why the observed
1219 frequencies of poloidal waves depend weakly on L , while the frequencies of toroidal
1220 waves are strongly dependent on L .
- 1221 At low m , ground signatures are weak because waves in space are weak because energy
1222 can easily escape through the simulation's outer boundary. At large m , ground signatures
1223 are attenuated by the ionosphere. The “sweet spot” in azimuthal modenumber at
1224 which ground signatures are strongest is around 16 to 32. Furthermore, ground signatures
1225 are strongest when ionospheric profiles corresponding to solar minimum are used.

1226 Driving in the poloidal electric field gives rise to primarily ground signatures polarized
1227 primarily in the east-west direction at the ground. And, when the frequency of the
1228 driving does not match the local eigenfrequency, the high- m resonates weakly in place,
1229 rather than tunneling across field lines to resonate strongly somewhere else.

1230 These findings imply, awkwardly, that the morphology of giant pulsations may reveal
1231 relatively little about their origins. One can consider a hypothetical magnetosphere
1232 subject to constant driving: broadband in frequency, broadband in modenumber, just
1233 outside the plasmapause. Low- m poloidal waves will quickly rotate to the toroidal mode
1234 (and/or propagate away). High- m waves will resonate in place, accumulating energy
1235 over time, and giving rise to “multiharmonic toroidal waves”[92]; Fourier components
1236 that do not match the local eigenfrequency will quickly asymptote. Waves with very high
1237 modenumbers will be attenuated by the ionosphere. The response on the ground will be
1238 significantly stronger during quiet solar conditions. In other words, the measurements
1239 on the ground will look very much like a giant pulsation.

1240 **TODO:** Notably, the present work offers no explanation as to Pgs’ distinctive distribu-
1241 tion in MLT!

₁₂₄₂ **Chapter 8**

₁₂₄₃ **Van Allen Probe Observations**

₁₂₄₄ The results presented in Chapter 7 are interesting on their own, but become particularly
₁₂₄₅ valuable when combined with observational data. Unfortunately, only a small number
₁₂₄₆ of studies to date have explored how Pc4 observation rate is affected by the harmonic
₁₂₄₇ and polarization structure of those waves.

₁₂₄₈ While Pc4 pulsations have previously been studied in terms of both harmonic[5, 16, 28,
₁₂₄₉ 45, 86, 95] and polarization[3, 18, 19, 54, 58], little work has considered both at the
₁₂₅₀ same time. This has largely been due to observational constraints. The classification of
₁₂₅₁ a wave’s harmonic is best carried out by computing the phase offset of the magnetic and
₁₂₅₂ electric field waveforms, simultaneous in situ measurements of which have only recently
₁₂₅₃ become available as part of the THEMIS[4] and Van Allen Probe[89] missions. The
₁₂₅₄ Van Allen Probes (launched in 2012) are particularly well-suited to the study of Pc4
₁₂₅₅ pulsations as their apogee of $L \sim 6$ coincides closely with eigenfrequencies in the Pc4
₁₂₅₆ range.

₁₂₅₇ The present chapter uses data from the Van Allen Probes’ EFW instrument[106] to
₁₂₅₈ survey the occurrence rate of FLRs in the Pc4 range as a function of harmonic parity
₁₂₅₉ and polarization, as well as magnitude, frequency, and phase. The tools used to perform
₁₂₆₀ the present analysis — SPEDAS and the SPICE kernel — are publicly available. They,
₁₂₆₁ along with the Python routines used to download, filter, and plot the data, can be found
₁₂₆₂ in a Git repository at <https://github.com/chizarlicious/RBSP>.

1263 TODO: Set this up, along with Tuna, at https://github.com/chizarlicious/UMN_Space-Physics.

1265 8.1 Sampling Bias and Event Selection

1266 The present analysis makes use of Van Allen Probe data from October 2012 to August
1267 2015 — the entire range available at the time of writing. Between the two probes, that's
1268 just over 2000 days of observation.

1269 For the purposes of Pc4 pulsations, it's reasonable to consider the two probes to be
1270 independent observers. Nearly all Pc4 events occur near apogee ($L \gtrsim 5$), at which
1271 point the two probes are several hours apart in MLT. Pc4 events are typically not large
1272 enough to be seen by both probes simultaneously, and not long enough in duration to
1273 be seen by two probes passing through the same region of space several hours apart.

1274 TODO: Quantify how often an event is seen by both probes?

1275 Electric and magnetic field waveforms are collected using the probes' EFW and EMFISIS
1276 instruments respectively. Values are cleaned up by averaging over the ten-second spin
1277 period. Three-dimensional electric field data is then obtained using the $\underline{E} \cdot \underline{B} = 0$
1278 assumption. Notably, this assumption is taken only when the probe's spin plane is
1279 offset from the magnetic field by at least 15° . The rest of the data — about half — is
1280 discarded, which introduces a sampling bias against the flanks.

1281 A further bias is introduced by the probes' non-integer number of precessions around
1282 Earth. As of July 2014, apogee had precessed once around Earth[18]. The present work
1283 considers roughly one and a half precessions; the nightside has been sampled at apogee
1284 twice as often as the dayside.

1285 The spatial distribution of usable data — that is, data for which three-dimensional
1286 electric and magnetic fields are available — is shown in Figure 8.1. Bins are unitary in
1287 L and in MLT. Distribution in magnetic latitude is not shown; the Van Allen Probes
1288 are localized to within $\sim 10^\circ$ of the equatorial plane.

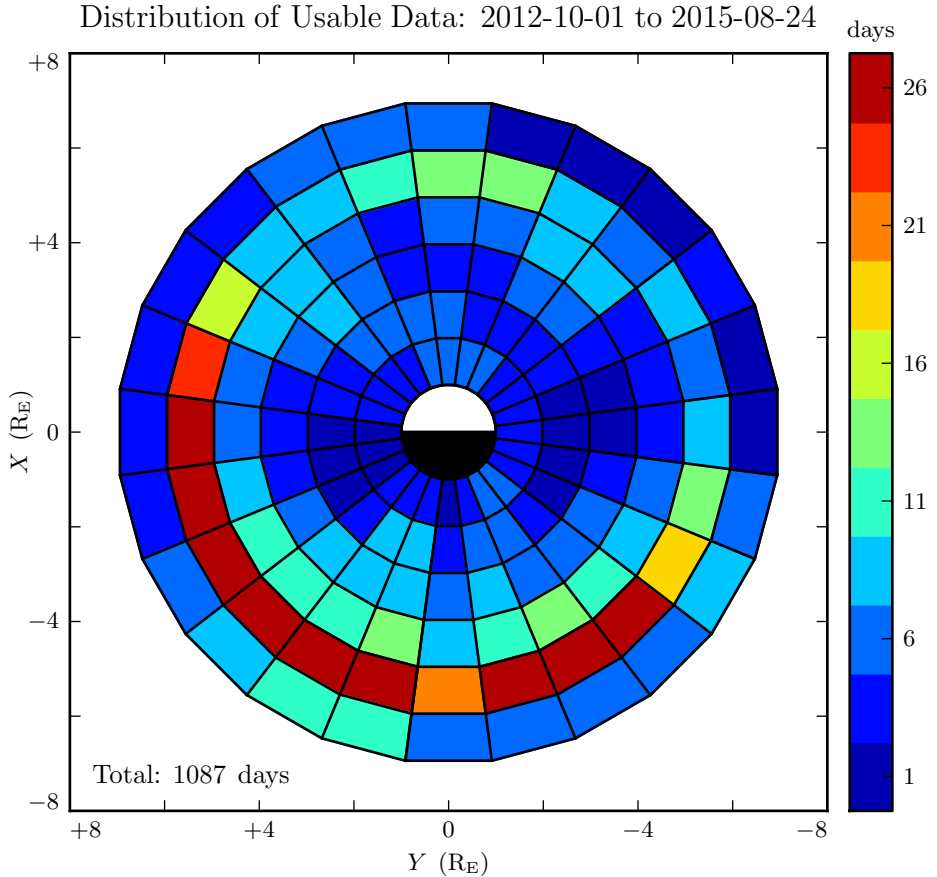


Figure 8.1: Three-dimensional electric field values are computed by assuming $\underline{E} \cdot \underline{B} = 0$. Data is discarded whenever the magnetic field falls within 15° of the spin plane, which introduces a bias against the flanks. Furthermore, the probes have completed one and a half precessions around Earth; the dayside has been sampled once at apogee, and the nightside twice.

1289 Field measurements are transformed from GSE coordinates into the same dipole coordi-
 1290 nates used in Chapters 5 and 7. The z axis (parallel to the background magnetic field)
 1291 is estimated using a ten-minute running average of the magnetic field measurements.
 1292 The y axis is set parallel to $\hat{z} \times \underline{r}$, where \underline{r} is the probe's geocentric position vector.
 1293 The x axis is then defined per $\hat{x} \equiv \hat{y} \times \hat{z}$. This scheme guarantees that the axes are
 1294 right-handed and pairwise orthogonal[58].

1295 The \sim 1000 days of usable data are considered half an hour at a time, which gives a fre-
 1296 quency resolution of \sim 0.5 mHz in the discrete Fourier transform. Spectra are computed
 1297 for all six field components: \tilde{B}_x , \tilde{B}_y , \tilde{B}_z , \tilde{E}_x , \tilde{E}_y , and \tilde{E}_z . The background magnetic
 1298 field is subtracted before transforming the magnetic field components, leaving only the
 1299 perturbation along each axis¹. Each waveform is also shifted vertically so that its mean
 1300 over the thirty minute event is zero.

Frequency-domain Poynting flux is computed from the electric and magnetic field transforms. A factor of L^3 compensates the compression of the flux tube, so that the resulting values are effective at the ionosphere. Poloidal and toroidal Poynting flux, respectively, are given by:

$$\tilde{S}_P \equiv -\frac{L^3}{\mu_0} \tilde{E}_y \tilde{B}_x^* \quad \tilde{S}_T \equiv \frac{L^3}{\mu_0} \tilde{E}_x \tilde{B}_y^* \quad (8.1)$$

1301 The poloidal and toroidal channels are independently checked for Pc4 waves. For each
 1302 channel, a Gaussian profile is fit to the magnitude of the Poynting flux, $|\tilde{S}(\omega)|$. If the
 1303 fit fails to converge, or if the peak of the Gaussian does not fall within 5 mHz of the
 1304 peak value of \tilde{S} , the event is discarded. Events are also discarded if their frequencies
 1305 fall outside the Pc4 frequency range (7 mHz to 25 mHz) or if their amplitudes fall below
 1306 10^{-2} mW/m² (out of consideration for instrument sensitivity).

1307 Events are discarded if their parity is ambiguous. The electric field and the magnetic
 1308 field must be coherent at a level of 0.9 or better (judged at the discrete Fourier transform
 1309 point closest to the peak of the Gaussian fit). Any event within 3° of the magnetic
 1310 equator is also not used; as discussed in Chapter 3, in order to distinguish an odd mode
 1311 from an even mode, it's necessary to know whether the observation is made north or
 1312 south of the equator.

1313 **TODO:** How much time do the probes spend within 3° of the magnetic equator?

1314 A visual inspection of events shows that those with broad “peaks” in their spectra
 1315 are typically not peaked at all — they are noisy spectra with several spectral features
 1316 grouped just closely enough to trick the fitting routine. A threshold is set at a FWHM

¹As in Chapters 5 and 7, B_x , refers not to the full magnetic field in the x direction, but to the perturbation in the x direction from the zeroth-order magnetic field. The same is true for B_y and B_z .

1317 of 3 mHz (equally, a standard deviation of 1.27 mHz). Any event with a Gaussian fit
1318 broader than that is discarded.

1319 Notably, events are not filtered on their phase — that is, on the division of their energy
1320 between standing and traveling waves. This is the topic of Section 8.5.

1321 **TODO: Are we biased in terms of DST? What's the distribution look like for the good**
1322 **data and for the bad data?**

1323 8.2 Events by Mode

1324 The filters described in Section 8.1 yield 762 Pc4 events, the spatial distribution of
1325 which is shown in Figure 8.2. In each bin, the event count is normalized to the amount
1326 of usable data, per Figure 8.1. Bins shown in white contain zero events. The rate in
1327 the bottom corner is an overall mean, weighing each bin equally.

1328 Consistent with previous work, Pc4 events peak on the dayside and are rarely observed
1329 at $L < 4$. Nearly 30 % of the usable data shown in Figure 8.1 is taken at $L < 4$, yet
1330 only 16 of the 762 events appear there.

1331 On the other hand, the present work runs contrary to Dai's 2015 result in terms of Pc4
1332 event rates with respect to the plasmapause (not shown). His analysis found (poloidal)
1333 Pc4 pulsations to be comparably common inside and outside the plasmapause[18]. In
1334 the present work, only 40 of the 762 events (5 %) fall inside the plasmasphere, despite
1335 the fact that 40 % of the available data falls within the plasmasphere. The disparity is
1336 not likely due to a difference in sampling — Dai's work, like the present work, uses data
1337 from the Van Allen Probes mission. Rather, the difference is likely due to disagreement
1338 in how the plasmapause is defined. Dai identifies the plasmapause by the maximum
1339 gradient in electron number density, while the present work takes an electron density of
1340 100 /cm^3 to mark the plasmapause².

1341 The same events in Figure 8.1 are shown again in Figure 8.3, partitioned by polarization
1342 and parity.

²Per ongoing work by Thaller.

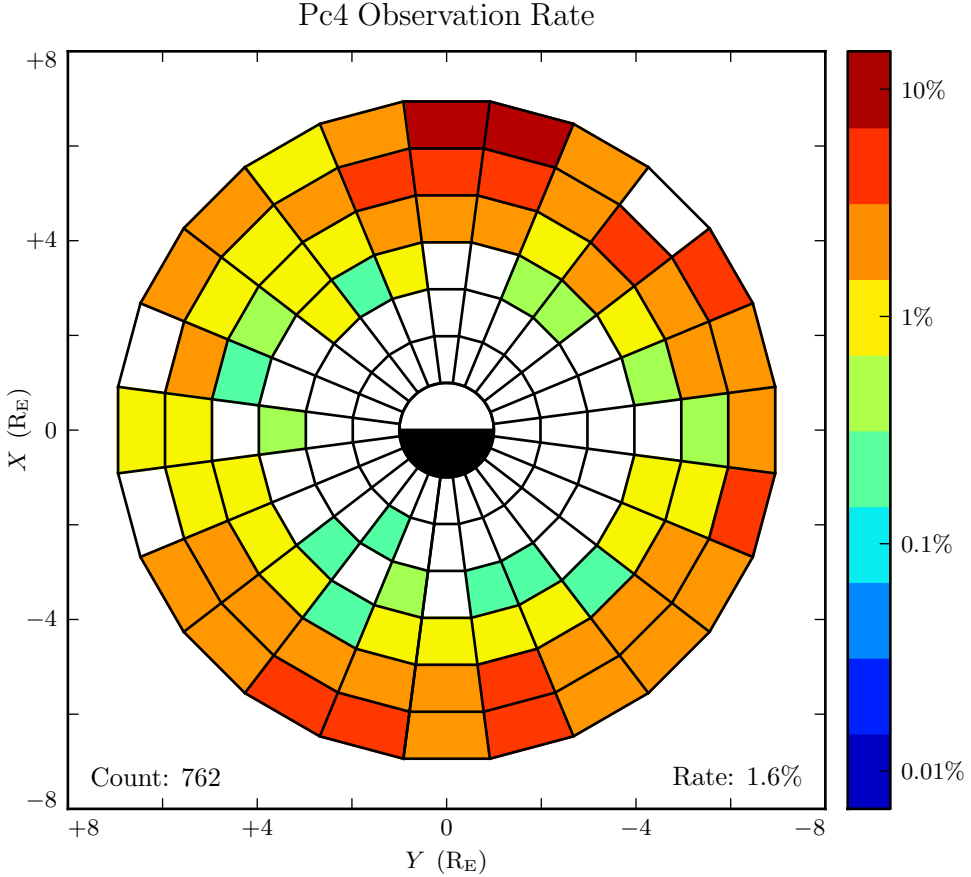


Figure 8.2: The above figure shows the spatial distribution of all 762 observed Pc4 events. Counts are normalized by the amount of usable data in each bin. The value in the bottom-right corner is the mean of the rate in each bin; it's an estimate of how often Pc4 events would be observed if the sampling were distributed uniformly in space. Events where the poloidal and toroidal channel trigger simultaneously ($\sim 10\%$ of cases) are counted as only a single event. Bins shown in white contain zero events.

1343 The distribution of even poloidal events in Figure 8.3 is consistent with that reported
 1344 by Dai[18]: the observation rate is peaked at noon, and smeared across the dusk side.
 1345 Notably, Dai's work focused on even poloidal waves. While he did not explicitly remove
 1346 odd events from his sample, he did introduce a threshold in the magnetic field. This
 1347 threshold is preferentially satisfied by even waves (which have a magnetic field antinode
 1348 near the equator) compared to odd waves (which have a magnetic field node). Dai

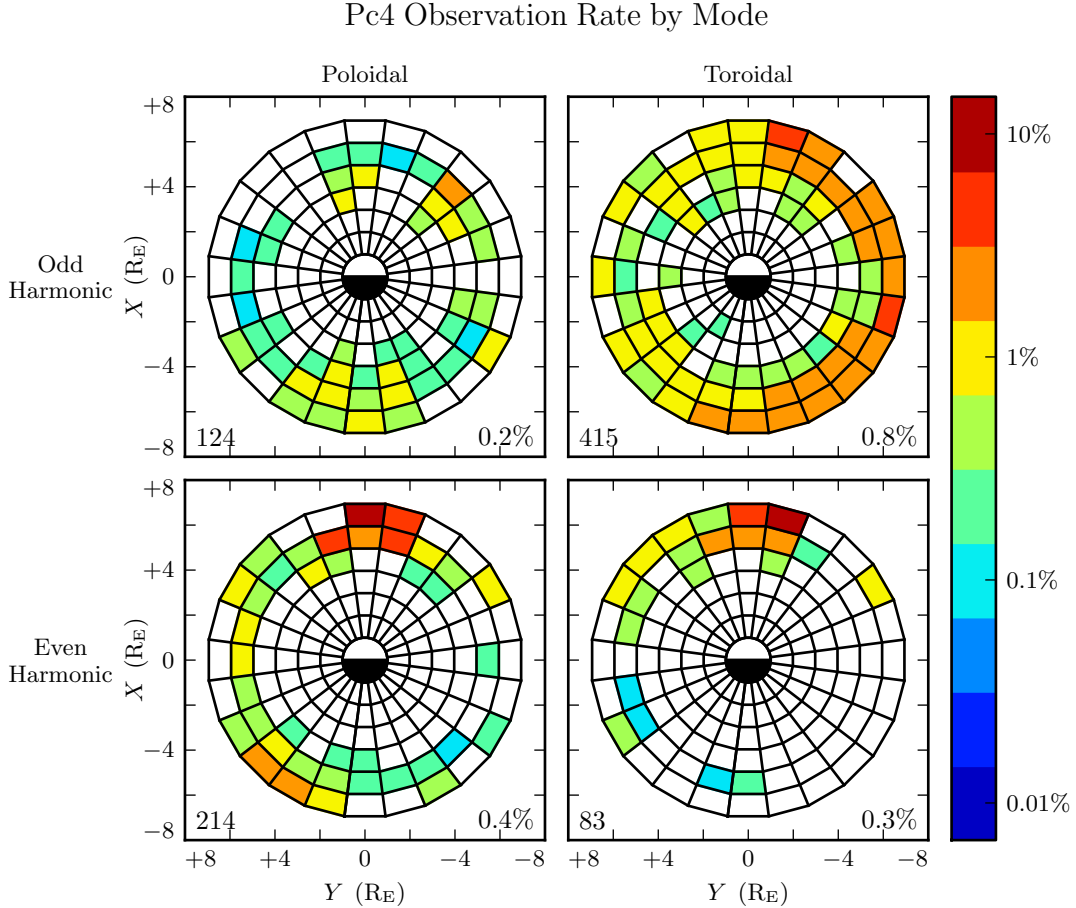


Figure 8.3: The above figure shows the spatial distribution for the same 762 events shown in Figure 8.2, partitioned by polarization and parity. The selection criteria described in Section 8.1 ensure that both properties are known for all events. Event counts are normalized by the time spent by the amount of usable data in each bin. Counts shown in the bottom-left corners do not sum to 762 because some events trigger on both the poloidal channel and the toroidal channel. Bins shown in white contain zero events.

1349 characterized the parity of only a quarter of his events; among those, he found even
1350 harmonics to outnumber odd harmonics ten-to-one.

1351 In fact — to the degree that they can be straightforwardly compared — the distributions
1352 in Figure 8.3 also show agreement with work by Anderson[3] (using AMPTE/CCE),

1353 Kokubun[54] (using ATS6), Liu[58] (using THEMIS), and Motoba[73] (using GOES).
1354 Toroidal events dominate overall, and are primarily seen on the morning side. Poloidal
1355 events are spread broadly in MLT, with a peak near noon and distinctive odd harmonics
1356 in the early morning.

1357 Crucially, the present work can offer insight into how previous results fit together. Unlike
1358 events considered in previous works, those shown in Figure 8.3 have all been categorized
1359 in terms of both polarization and parity. And, perhaps more importantly, the selection
1360 process has not introduced a bias with respect to polarization or parity (at least not an
1361 obvious one).

1362 The even events shown in Figure 8.3 show good agreement with the numerical results
1363 in Chapter 7. The distributions are qualitatively similar, as might be expected if even
1364 poloidal waves served as a source for even toroidal waves. Even poloidal waves are more
1365 prevalent, suggesting a typical event duration comparable to the poloidal-to-toroidal
1366 rotation timescale. And even toroidal events are skewed dayward compared to even
1367 poloidal events, suggesting that poloidal-to-toroidal rotation is inhibited by increased
1368 Joule dissipation on the nightside.

1369 The same can be said to some extent for the odd events in Figure 8.3, though the trends
1370 are less strong. Odd poloidal and odd toroidal events are both scarce on the dusk flank.
1371 On the dawn flank, poloidal events skew nightward, while toroidal events are spread
1372 broadly — that is, they are skewed dayward compared to the poloidal events. However,
1373 it's unclear why odd toroidal events outnumber odd poloidal events to such a degree.

1374 Not only does Figure 8.3 show that toroidal events outnumber poloidal events, but it
1375 also shows that toroidal events are predominantly odd harmonics — as opposed to the
1376 primarily-even poloidal events.

1377 This may suggest that odd poloidal waves are more likely than even ones to be driven
1378 at low modenumber (allowing a prompt rotation of that energy to the toroidal mode).
1379 One might expect low- m poloidal modes to be driven by a broad, sudden change in solar
1380 wind dynamic pressure, for instance. The relative scarcity of odd poloidal observations
1381 on the dayside may indicate a short-lived source. At low m , energy rotates to the

1382 toroidal mode on the order of a wave period; without an ongoing source, there would
1383 be no poloidal wave to observe.

1384 TODO: Actually, it looks like odd poloidal waves are split about half-and-half around
1385 $\left| \frac{B_z}{B_x} \right| = 0.2$. Compressional odd modes are more common near midnight. Noncompres-
1386 sional ones are mostly in the morning. Even poloidal events are skewed toward low m .
1387 This is probably worth showing.

1388 TODO: Odd poloidal events are skewed nightward compared to odd toroidal events.
1389 This is not surprising. Per Chapter 7, nightside poloidal events are less likely to give
1390 rise to toroidal events than those on the dayside. Even events too, actually. The toroidal
1391 distribution looks like the poloidal distribution, but skewed dayward.

1392 This would furthermore be consistent with even modes' apparent dearth of ground
1393 signatures[96]. If even harmonics tend to be produced at higher modenumbers than odd
1394 ones, even harmonics would be expected to produce ground signatures less often³.

1395 Even poloidal modes and even toroidal modes exhibit similar distributions in space:
1396 both are peaked at noon and smeared across the dusk flank, with little activity on the
1397 dawn side. This is further support for the even poloidal wave as a significant source for
1398 the even toroidal mode.

1399 TODO: People have talked about this. Is there a conventional explanation for dawn-
1400 dusk asymmetry?

1401 TODO: What else do we want to say here? Or does the rest of the commentary belong
1402 in the later sections? Note that plots in future sections are lower resolution, to make
1403 sure that the number of bins remains much smaller than the number of events.

1404 TODO: How does this relate to the numerical results in Chapter 7?

1405 In Figure 8.3, events are partitioned by parity and polarization, yielding 124 odd poloidal
1406 events, 214 even poloidal events, 415 odd toroidal events, and 83 even toroidal events
1407 — a total of 836 events. The total is greater than 762 because in $\sim 10\%$ of events, the
1408 poloidal and toroidal channels trigger independently. Such cases are marked as a single
1409 event in Figure 8.2, but the toroidal and poloidal events are both shown in Figure 8.3.

³See Equation (3.3).

1410 Double-triggering can be taken as a vague proxy for event quality. When the channels
 1411 both trigger independently, the two events almost always (71 of 74 events) exhibit the
 1412 same parity. This suggests a poloidal wave with sufficient power, and a sufficient narrow
 1413 spectral peak, that it can still be seen after much of its energy has rotated to the toroidal
 1414 mode.

Rate of Double Events by Parity and Storm Index

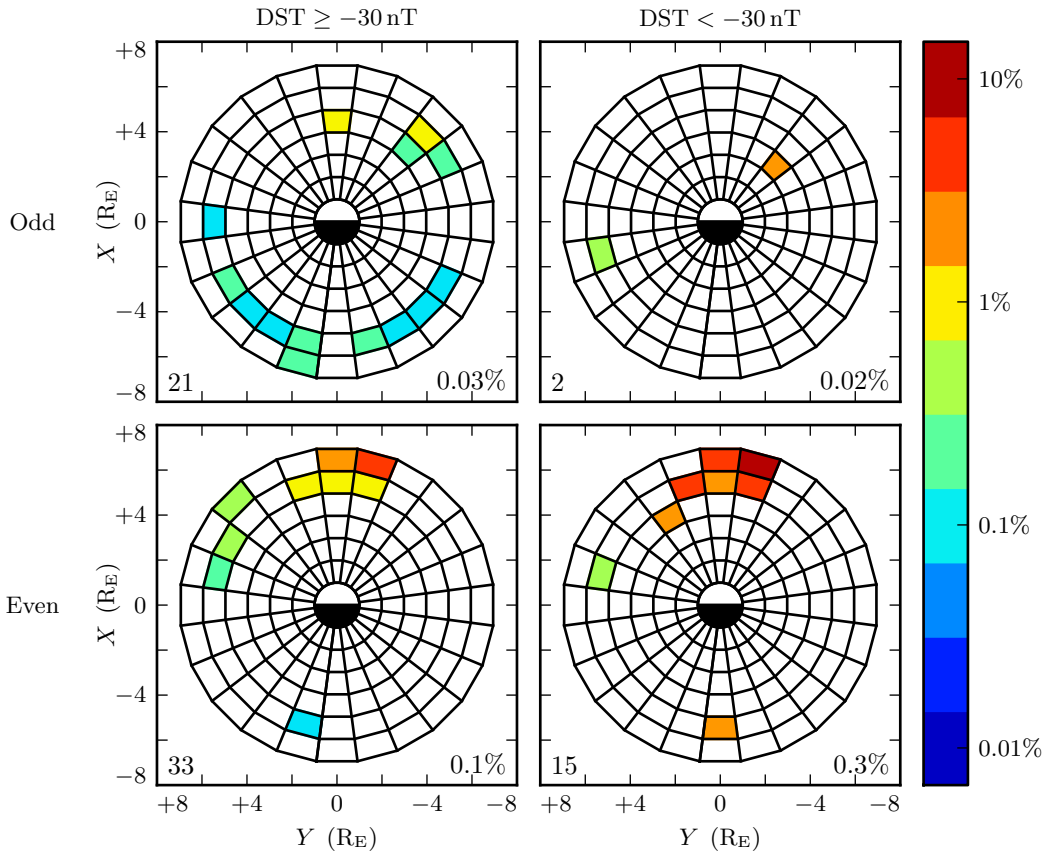


Figure 8.4: A double event is a simultaneous triggering of the poloidal and toroidal channels on the same probe. In such cases, the two channels almost always exhibit the same parity. Double events serve as a vague proxy for event quality — a poloidal event with sufficient strength and clarity to be seen even after much of its energy has rotated to the toroidal mode. Odd double events are spread broadly; even events are concentrated near noon, and become more common during geomagnetically active times.

1415 The spatial distribution of double events is shown in Figure 8.4. The left column shows
1416 events observed with $DST \geq -30$ nT, normalized by the amount of usable data at
1417 $DST \geq -30$ nT. The right column shows events at $DST < -30$ nT, normalized by the
1418 amount of data with $DST < -30$ nT.

1419 Odd double-triggering events are spread broadly in MLT. They rarely occur twice on
1420 the same day; the 23 events shown take place over 20 different dates. Odd double events
1421 occur at similar rates regardless of DST.

1422 Even-harmonic double-triggering events, on the other hand, are mostly seen near noon,
1423 and are significantly more common during geomagnetically active times. Even events
1424 are also more concentrated than odd ones. The 48 even-harmonic double-events shown
1425 in the bottom row of Figure 8.4 are spread over 20 days, and 35 of them are spread over
1426 just 7 days. This clustering — where the poloidal and toroidal channel both trigger for
1427 five to ten half-hour events in the same day — is prevalent regardless of DST.

1428 8.3 Events by Amplitude

1429 One might reasonable be concerned that the spatial distributions presented in Figure 8.3
1430 are dominated by these small events, while Pc4 events large enough to be noteworthy
1431 follow a different distribution entirely. The goal of the present section is to address that
1432 concern.

1433 The distribution of event magnitudes is presented in Figure 8.5, graded based on the
1434 peak of the Gaussian fit of each event's Poynting flux, $|\tilde{S}(\omega)|$. Mean and median
1435 values are listed for each mode. Most events are small, with Poynting flux well below
1436 0.1 mW/m^2 when mapped to the ionosphere. Only a handful of events — 3 out of 762
1437 — exceed 1 mW/m^2 , typically taken to be the threshold at which visible auroral arcs
1438 form. One such event is shown in Figure 8.6.

1439 **TODO:** Say something about this event? Not really clear what purpose is served by this
1440 example, actually. As a matter of curiosity, the apparent wave activity in the toroidal
1441 channel did not pass the event selection trigger because the electric and magnetic wave-
1442 forms are not coherent.

Amplitude Distribution of Pc4 Events by Mode

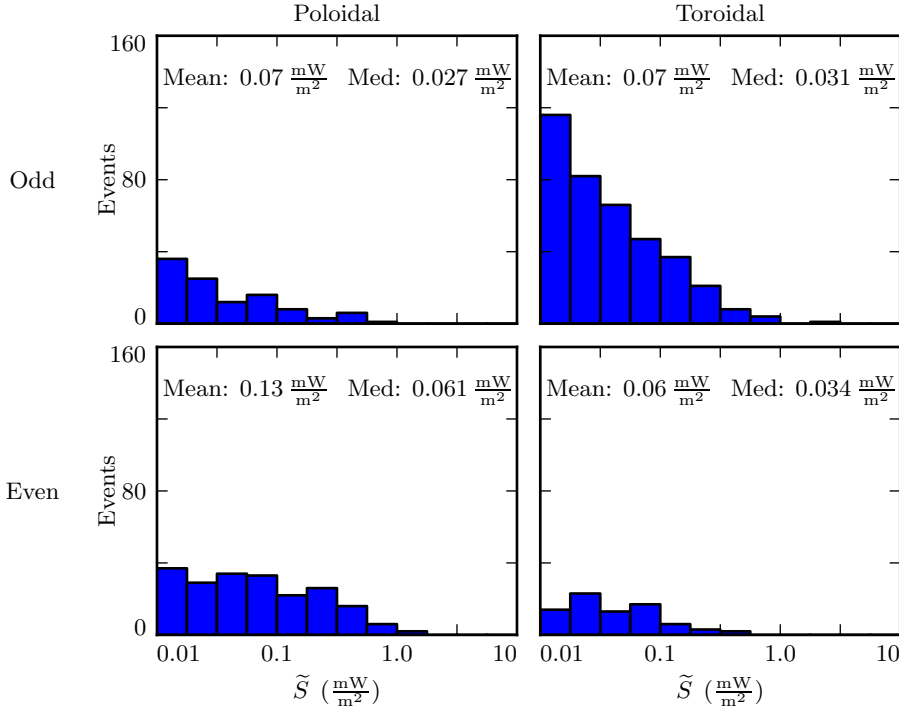


Figure 8.5: Amplitude distribution is shown for Pc4 events by parity and polarization, based on the peak of the spectrum's Gaussian fit. Odd poloidal events, odd toroidal events, and even toroidal events fall off sharply with increasing amplitude, while the even poloidal events are distributed more broadly — the mean and median of the even poloidal distribution is twice as large as that of the others.

1443 Perhaps the most notable feature of Figure 8.5 is the relative uniformity of the distri-
1444 bution of even poloidal events. If a higher magnitude threshold is imposed, as shown in
1445 Figure 8.7, the proportion of even poloidal events rises.

1446 The spatial bins in Figure 8.7 are larger than those in Section 8.2; this change reflects
1447 an effort to keep the number of events large compared to the number of bins, even when
1448 considering relatively small subsets of the data. The larger bins — two hours wide in
1449 MLT and divided at $L = 5$ radially — are also used in Sections 8.4 and 8.5. All of the
1450 large-binned bullseye plots also share a common logarithmic color bar.

1451 All else being equal, one might expect the amplitude distribution of even toroidal modes
1452 to mimic that of even poloidal modes, since poloidal waves asymptotically rotate to
1453 toroidal waves. However, this does not seem to be the case. The mean and median
1454 magnitudes are more or less consistent for even toroidal modes, odd toroidal modes,
1455 and odd poloidal modes, while even poloidal modes are twice as large by those metrics.
1456 This would seem to imply that large even poloidal modes have disproportionately high
1457 modenumbers, and thus deliver energy to the toroidal mode less efficiently. This expla-
1458 nation is also unsatisfying, however; Figure 8.7 shows that even poloidal and toroidal
1459 modes both become more concentrated near noon at high amplitude, suggesting a com-
1460 mon origin.

Waveforms and Spectra: Odd Poloidal Wave

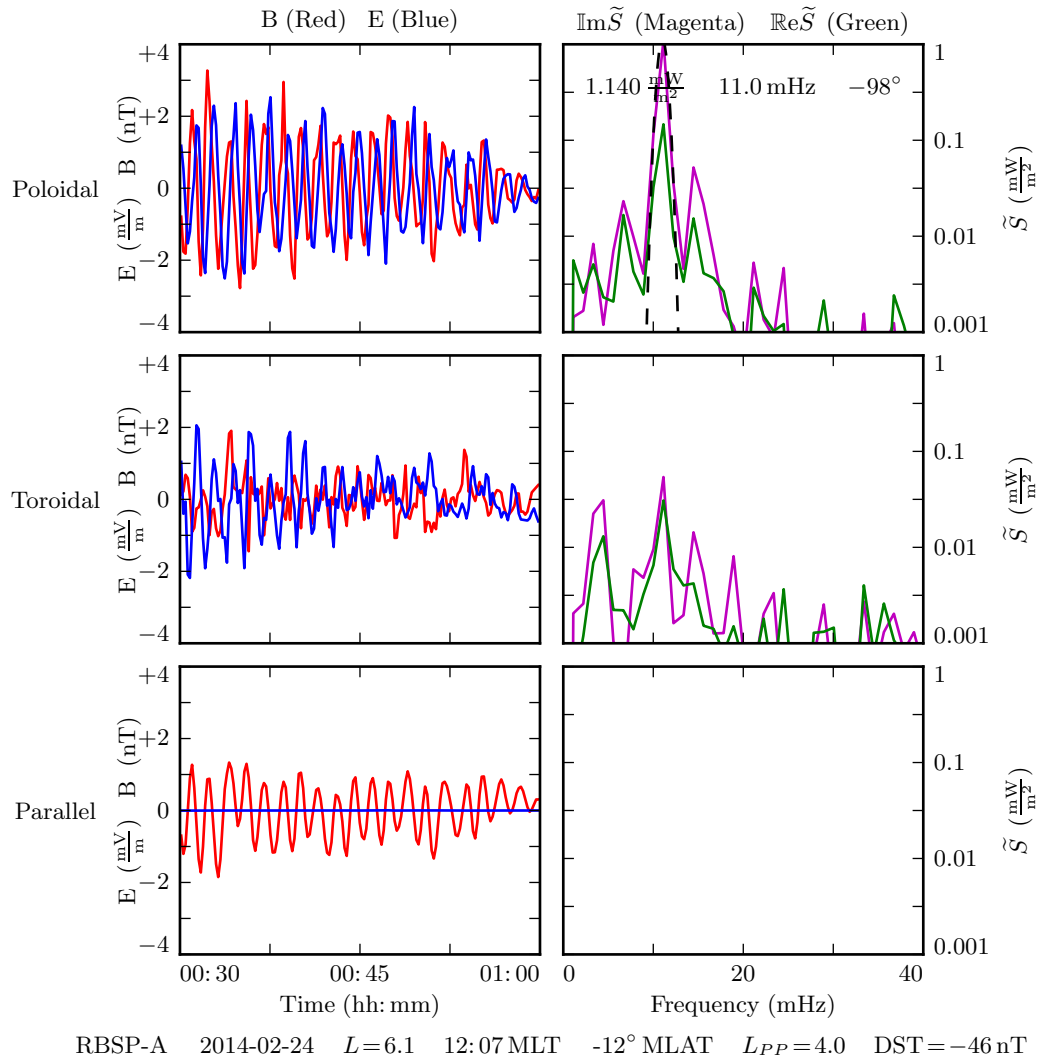


Figure 8.6: **TODO:** ...

Distribution of Pc4 Events by Mode and Amplitude

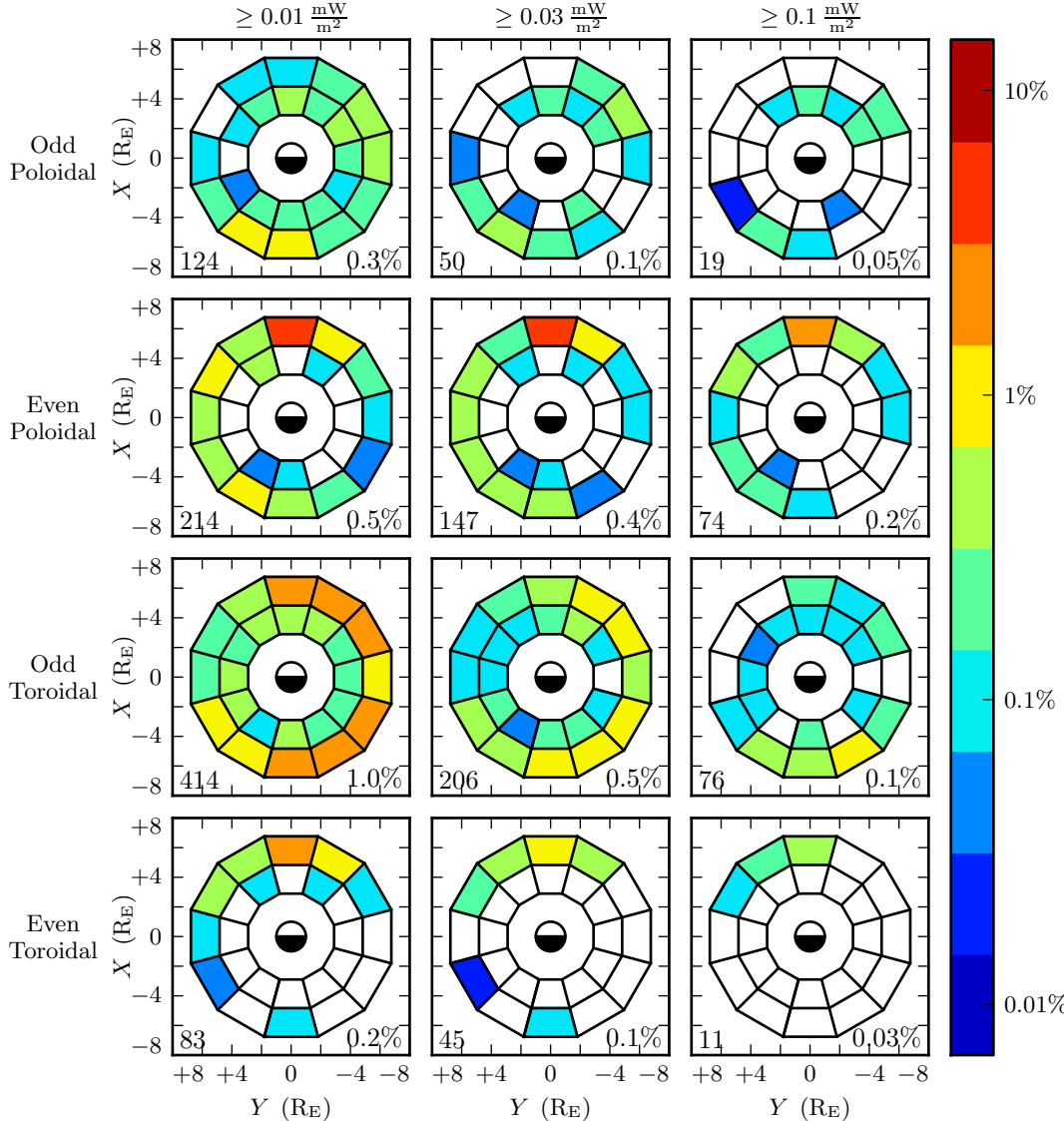


Figure 8.7: The above figure shows the distribution of Pc4 event observations by mode. Event magnitude cutoff is constant down each column, and increases from left to right. Stronger even events appear to become more concentrated on the dayside as the amplitude increases. Even poloidal events also become significantly more numerous relative to the other three modes, from 26 % at a cutoff of 0.01 mW/m^2 to 41 % at 0.1 mW/m^2 .

1461 8.4 Events by Frequency

1462 The difference in magnetospheric conditions between the dayside and the nightside
1463 suggest that different eigenfrequencies should arise between dayside and nightside res-
1464 onances at the same L -shell. In fact, this phenomenon has been observed directly;
1465 the frequencies of azimuthally-drifting FLRs have been shown to change over time[73].
1466 The effect is attributed to the difference in mass loading (and thus Alfvén speed) as a
1467 function of MLT.

1468 This effect was furthermore apparent in the numerical results shown in Chapter 7, where
1469 Alfvén speeds on the dayside (based on empirical profiles) gave rise to significantly higher
1470 eigenfrequencies than those on the nightside.

1471 In Figure 8.8, events at 11 mHz to 17 mHz (center column) do seem to be shifted night-
1472 ward compared to those at 7 mHz to 11 mHz (left column), but the effect is far more
1473 pronounced than what is suggested by Sections 7.2 and 7.3.

1474 **TODO:** We should show the runs driven at $L \sim 5$ across the board. Dayside and
1475 nightside. That way we can make a fair comparison.

1476 As might be expected, even events are more prevalent than first-harmonic-dominated
1477 odd events higher in the Pc4 range. Events at 7 mHz to 11 mHz (left column) outnumber
1478 those at 17 mHz to 25 mHz (right column) ten-to-one or more for odd events. Among
1479 even events, the comparison is closer to three-to-one.

1480 The spatial distribution of odd toroidal events above 17 mHz warrants specific consid-
1481 eration. Whereas odd toroidal events overall show an overwhelming preference for the
1482 morning side, those at the top of the Pc4 frequency band instead appear from noon
1483 to dusk. It's possible that this distribution is a consequence of the small number of
1484 events (25). More likely, however, is that these are third-harmonic events, and that
1485 their source more closely resembles the source for second-harmonic waves than it does
1486 first-harmonics.

1487 **TODO:** Have people looked at third harmonics?

1488 The frequency distribution for each mode is shown in Figure 8.9. The most distinctive
1489 feature, certainly, is the frequency peak in the odd toroidal mode near 9 mHz. This is
1490 in line with the idea that toroidal waves exhibit frequencies that depend sharply on L ,
1491 as discussed in Chapter 7. While the Van Allen Probes' orbits do cover a large range of
1492 L -shells, their observations (and thus the selected events) are concentrated near apogee
1493 at $L \sim 6$.

1494 TODO: Maybe put the Gaussian fit back on top of these distributions? The distributions
1495 are not particularly Gaussian, but it gives a quantitative estimate of the spread.

Distribution of Pc4 Events by Mode and Frequency

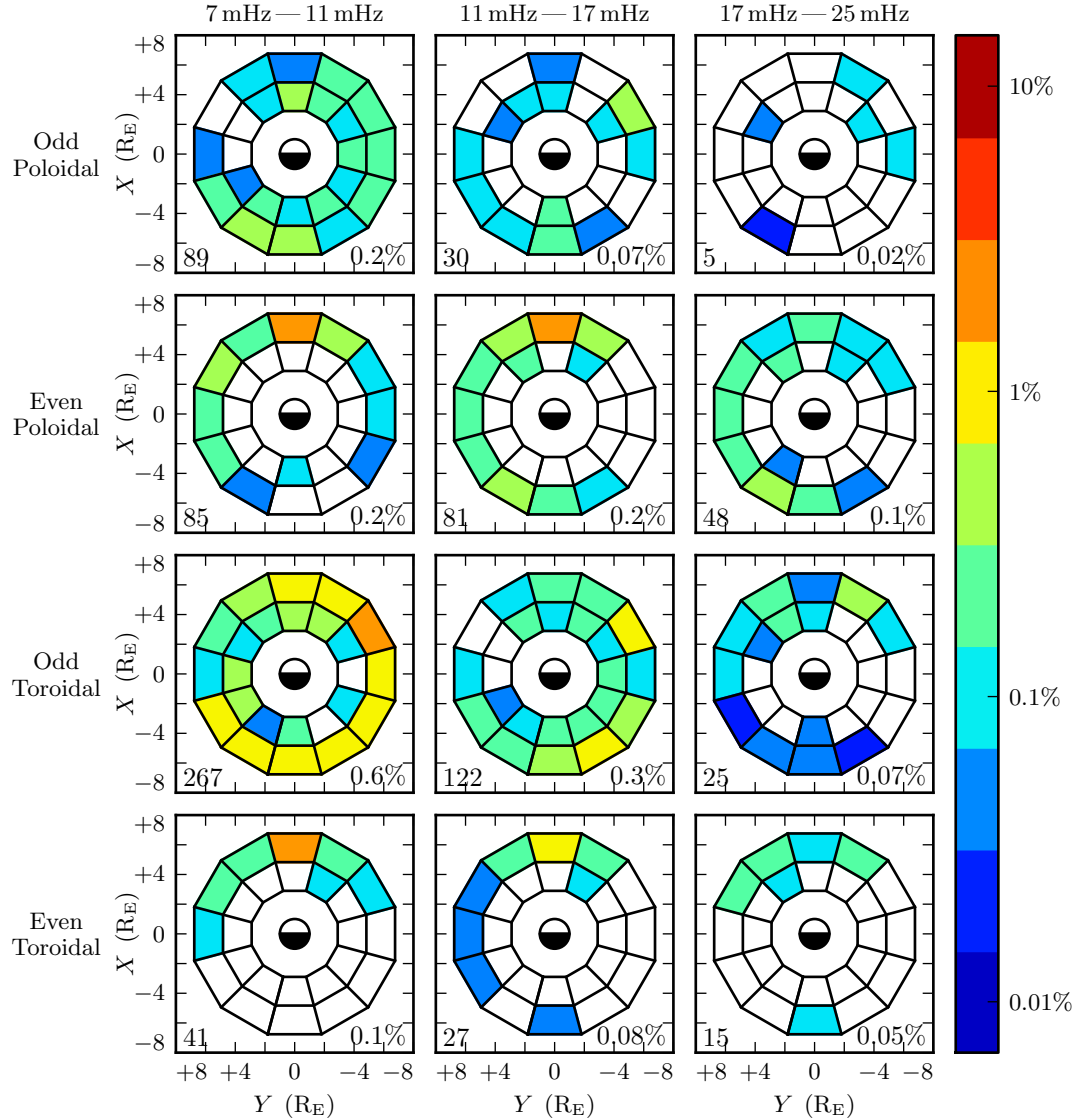


Figure 8.8: Event distributions above are shown in terms of mode (row) as well as event frequency (column). Mid-frequency Pc4 events are shifted somewhat nightward compared to low-frequency Pc4 events, as might be expected from the dayside's faster Alfvén speed. At the top of the Pc4 band, the distribution of odd toroidal events takes on a decidedly different character; this is likely because they are third harmonics rather than first harmonics.

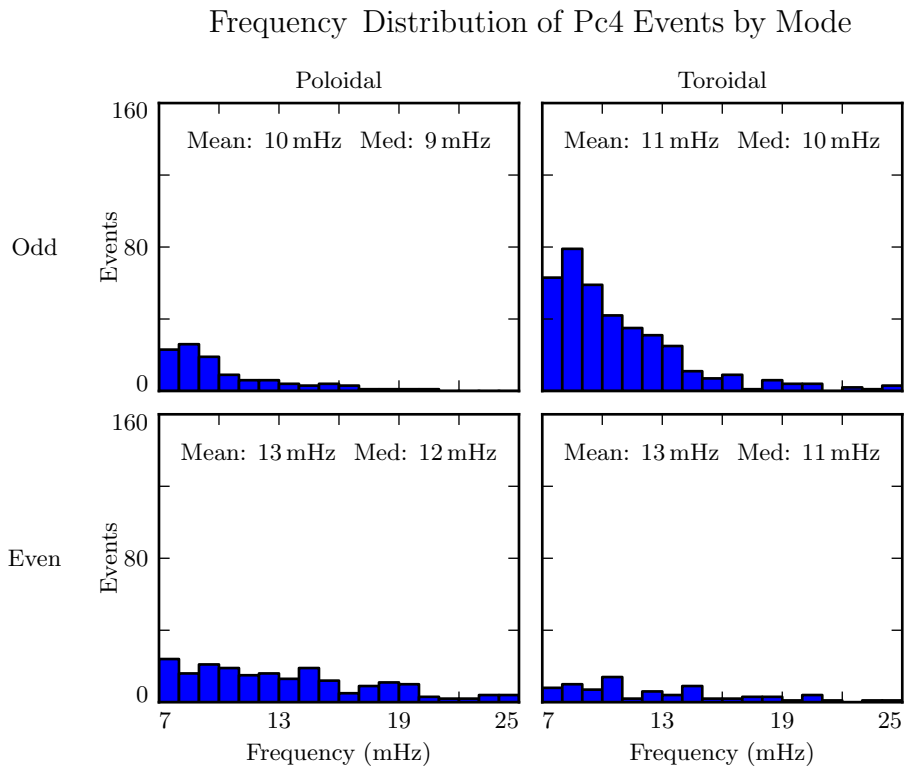


Figure 8.9: Frequency distributions are shown for all events, divided by harmonic and polarization. Odd toroidal events exhibit a particularly sharp peak in frequency, which is consistent with the toroidal mode's strong correlation with the local eigenfrequency. Poloidal modes appear more spread out in frequency, which is also consistent with past observations and with the numerical results in Chapter 7.

1496 8.5 Events by Phase

1497 The phase of a wave — that is, the phase offset between a wave's electric and magnetic
1498 fields — indicates how its energy is partitioned between the standing and traveling
1499 wave modes. An ideal standing wave has a phase of $\pm 90^\circ$, and thus its Poynting flux is
1500 completely imaginary. A traveling wave, on the other hand, has electric and magnetic
1501 fields in phase (or in antiphase), and is associated with a net movement of energy,
1502 usually toward the ionosphere.

1503 Wave phase is a topic of significant interest, since it allows an estimate to be made of
1504 the wave's lifetime. And, because phase can only be determined using simultaneous
1505 electric and magnetic field measurements, it has only recently become observable.

1506 **TODO: Do people really care about phase, or is it just John?**

The energy per unit volume, and the rate at which energy is carried out of that volume
by Poynting flux, are respectively given by:

$$U = \frac{R^3}{2\mu_0} B^2 \quad \frac{\partial}{\partial t} U = \frac{R^2}{\mu_0} EB \cos \varphi \quad (8.2)$$

1507 Where B , E , and R are the characteristic magnetic field magnitude, electric field mag-
1508 nitude, and length scale. The phase, $\varphi \equiv \arctan \frac{\text{Im}S}{\text{Re}S}$, enters because only real Poynting
1509 flux carries energy.

The ratio of the two quantities in Equation (8.2) gives a characteristic timescale over
which energy leaves the system

$$\tau \equiv \frac{BR}{2E \cos \varphi} \quad (8.3)$$

1510 In the present case, magnetic fields are on the order of 1 nT and electric fields are on
1511 the order of 1 mV/m. A reasonable scale length might be 10^4 km, the distance traversed
1512 by the probe over the course of a half-hour event (notably, back-to-back events are
1513 unusual).

1514 At a phase of 80° , this timescale is comparable to a $Pc4$ wave period. At 135° , where
1515 energy is divided evenly between the standing and traveling wave, the timescale is only
1516 7 seconds. A wave with a phase so far from 90° would quickly vanish unless it were
1517 constantly being replenished.

1518 An example of just such an event is shown in Figure 8.10. The left column shows
1519 electric and magnetic field waveforms in blue and red respectively. The right shows
1520 the corresponding spectra: imaginary Poynting flux in magenta (corresponding to the
1521 strength of the standing wave) and real Poynting flux in green (for the traveling wave).
1522 The black line is a Gaussian fit to the magnitude of the Poynting flux.

1523 The poloidal channel shows a mostly-standing wave, with a phase of 79° . The coherent
1524 activity in the compressional magnetic field implies a low azimuthal modenumber, and
1525 thus a fast rotation of energy from the poloidal mode to the toroidal mode. It's likely
1526 the rotation of energy from the poloidal mode contributes significantly to the toroidal
1527 mode's lifetime; the toroidal wave's phase is 130° , so its energy should be carried away
1528 quickly by Poynting flux.

1529 The selection process described in Section 8.1 does not explicitly consider phase. How-
1530 ever, the discrete Fourier transform is performed over a half-hour time span. An event
1531 with a comparatively short lifetime would be unlikely to register. It's unsurprising to
1532 see the events in Figure 8.11 tightly clustered near 90° .

1533 It's further notable in Figure 8.11 that the odd events are more spread out in phase
1534 than the even events. Near the equator, odd modes have an electric field antinode and
1535 a magnetic field node; per Equation (8.3), an odd mode's lifetime should be longer than
1536 that of an even mode with the same phase. Figure 8.11 uses the absolute value of each
1537 event's phase, as does Figure 8.12.

1538 Unlike amplitude (Section 8.3) and frequency (Section 8.4), events of different phase do
1539 not seem to exhibit different spatial distributions, as shown in Figure 8.12. Comparisons
1540 are limited by the small event counts in several of the subplots; however, coarsely
1541 speaking, events with phases of 75° and worse (left column) show spatial distributions
1542 more or less in proportion with events phased 85° or better (right column).

Waveforms and Spectra: Odd Poloidal Wave and Odd Toroidal Wave

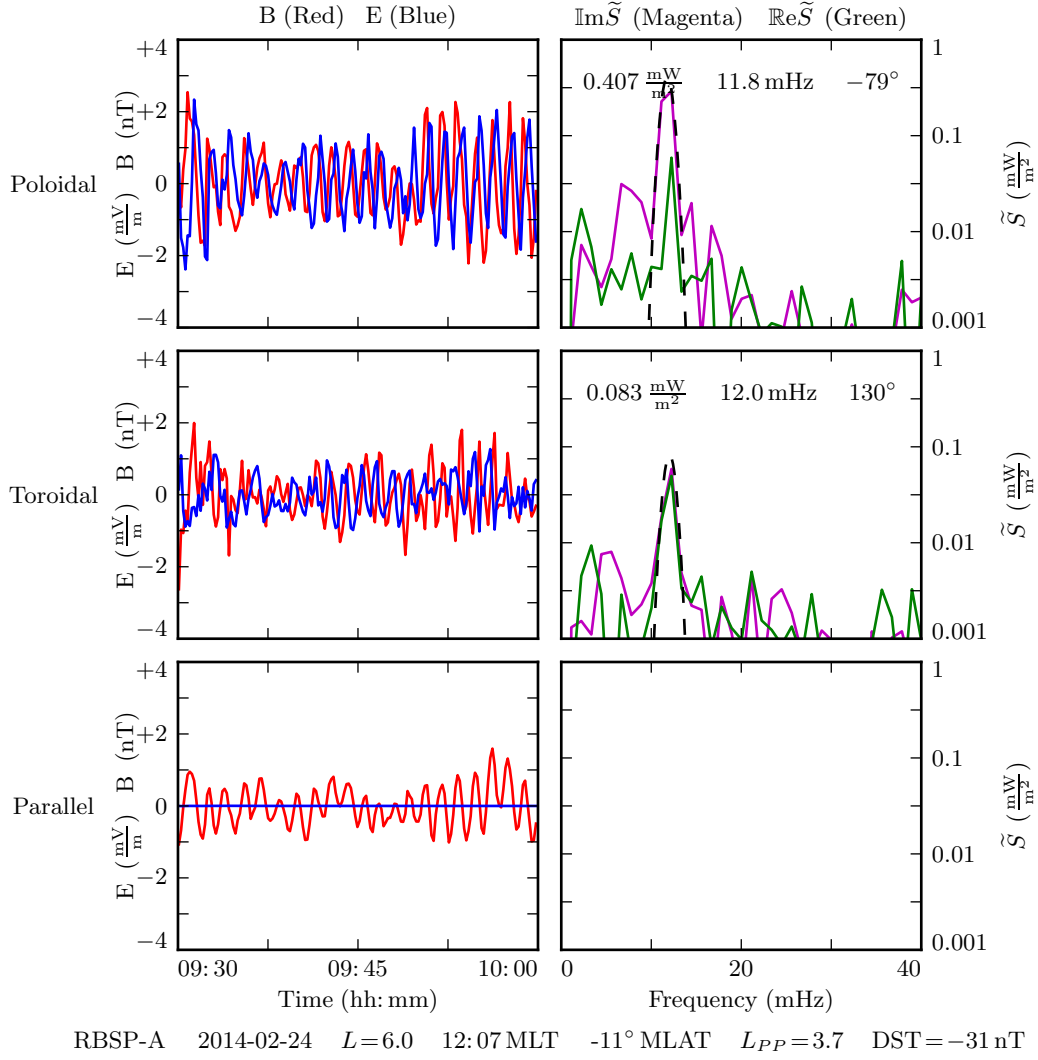


Figure 8.10: The above is a double event, where the poloidal and toroidal channels have been independently selected as events. The poloidal channel shows a wave with most of its energy in the standing wave (phase of 79°). The toroidal mode has a significant traveling component (phase of 130°). The compressional activity implies a low modenumber, which would cause energy to rotate quickly from the poloidal mode to the toroidal mode — evidently at a sufficient rate to replenish the losses due to the traveling mode's real Poynting flux.

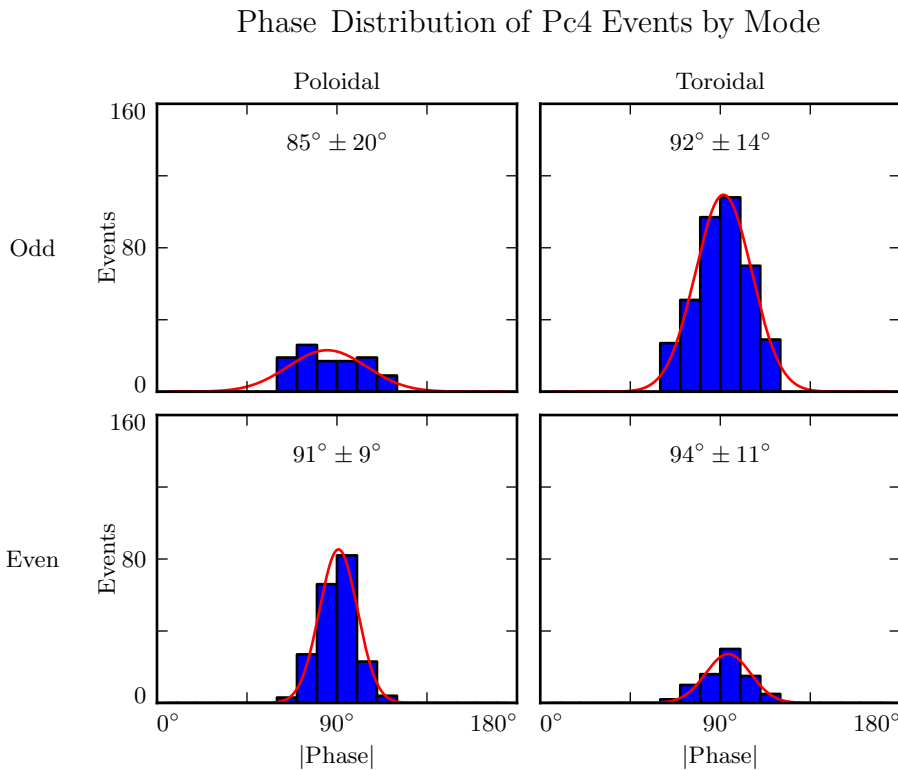


Figure 8.11: The (absolute) phase of the selected Pc4 events is shown above. All modes show phase distributions peaked around 90° . This reflects the fact that a significant traveling wave component quickly carries energy away from an FLR. Odd events are spread more broadly in phase than even events. This is consistent with the odd modes' electric field antinode near the equator, where events are observed; the characteristic loss timescale depends on $\frac{B}{E}$ per Equation (8.3).

Distribution of Pc4 Events by Mode and Phase

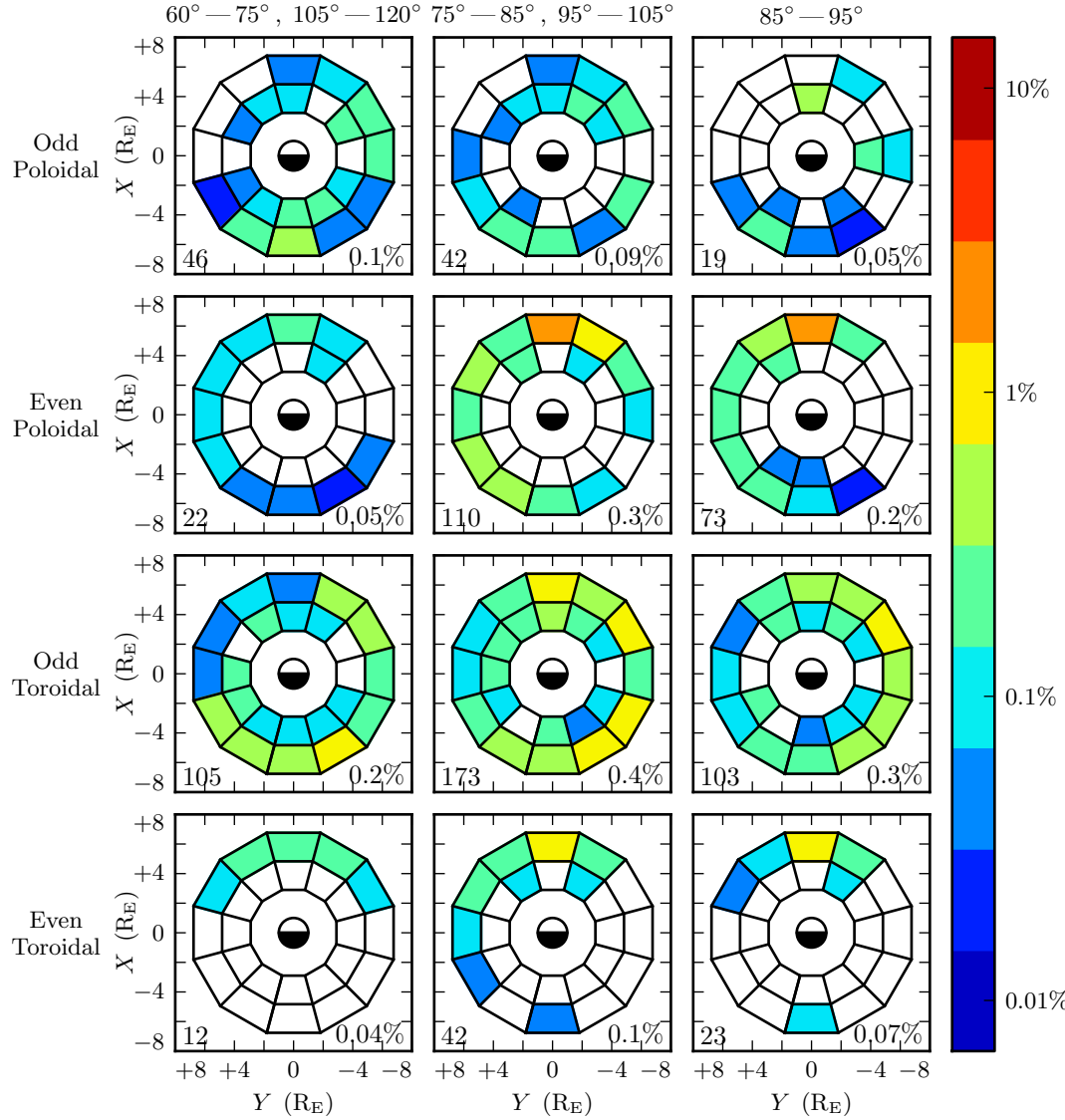


Figure 8.12: The observation rate of events is shown above, divided by (absolute) phase as well as mode. The closer a phase to 90° , the more of an event's energy is in the standing wave, rather than the traveling wave. The spatial distribution of events is more or less consistent between waves with phases very close to 90° and those with a significant traveling wave component.

1543 **8.6 Discussion**

1544 TODO: Odd poloidal events and odd toroidal events are distributed similarly in space.
1545 Even poloidal events and even toroidal events too. Toroidal events are skewed dayward
1546 compared to poloidal events, which makes sense, since on the nightside poloidal-to-
1547 toroidal rotation timescales are comparable to dissipation timescales.

1548 TODO: Poloidal events are mostly even. Toroidal events are mostly odd. Maybe this
1549 indicates a different preference in modenumber?

1550 TODO: Even poloidal events are skewed toward high amplitude compared to the other
1551 modes. Stronger even poloidal events are also skewed dayward.

1552 TODO: Odd toroidal events near the top of the Pc4 frequency range exhibit qualitatively
1553 different behavior from the other odd toroidal modes. They are probably third harmon-
1554 ics. Maybe third harmonics have a source mechanism more like second harmonics than
1555 like first.

1556 TODO: Most events have (absolute) phase in the range 80° to 100° , indicating that
1557 most of the energy is in the standing wave. Odd events are spread a bit more broadly
1558 in phase. This makes sense, since they ahve an electric field antinode near the equator
1559 (where measurements are made) which makes them less susceptible to energy loss from
1560 the traveling wave.

1561 **Chapter 9**

1562 **Conclusion**

1563 **9.1 Summary of Results**

1564 TODO: Code development... Chapters 5 and 6

1565 TODO: Make the Git repository public, and link to it.

1566 TODO: Numerical results... Chapter 7

1567 TODO: Re-summarize the Discussion sections, I guess.

1568 TODO: Observational results... Chapter 8

1569 TODO: Link to the Git repository.

1570 **9.2 Future Work**

1571 TODO: Code development.

1572 Arbitrary deformation of grid. Get $\hat{e}_i = \frac{\partial}{\partial u^i} \underline{x}$, then $g_{ij} = \hat{e}_i \cdot \hat{e}_j$, then invert the metric
1573 tensor for contravariant components.

1574 MPI. Time to compute vs time to broadcast. This might make sense for inertial length
1575 scales.

1576 Better ionospheric profiles. Distinction between the dawn and dusk flanks. Maybe even
1577 update the conductivity based on energy deposition — precipitation causes ionization!

1578 IRI ionosphere model. Solar illumination effects.

1579 **TODO: Numerical work.**

1580 More complicated driving. Higher harmonics, non-sinusoidal waveforms. Maybe even
1581 drive based on events?

1582 Look at the phase of waves in Tuna. How much is standing/traveling?

1583 **TODO: Analysis of RBSP data.**

1584 Basically just do everything over again, twice as well, once the probes have finished
1585 sampling the dayside again.

1586 References

- 1587 [1] S.-I. Akasofu. The development of the auroral substorm. *Planetary and Space*
1588 *Science*, 12(4):273–282, 1964.
- 1589 [2] H. Alfvén. On the cosmogony of the solar system III. *Stockholms Observatoriums*
1590 *Annaler*, 14:9.1–9.29, 1946.
- 1591 [3] B. J. Anderson, M. J. Engebretson, S. P. Rounds, L. J. Zanetti, and T. A. Potemra.
1592 A statistical study of Pc 3-5 pulsations observed by the AMPTE/CCE magnetic
1593 fields experiment, 1. occurrence distributions. *J. Geophys. Res.*, 95(A7):10495,
1594 1990.
- 1595 [4] V. Angelopoulos. The THEMIS mission. *Space Science Reviews*, 141(1-4):5–34,
1596 2008.
- 1597 [5] C. W. Arthur and R. L. McPherron. The statistical character of Pc 4 magnetic
1598 pulsations at synchronous orbit. *J. Geophys. Res.*, 86(A3):1325, 1981.
- 1599 [6] K. Birkeland. Expédition norvégienne de 1899-1900 pour l'étude des aurores
1600 boréales. *Mat. Naturvidensk. Kl.*, KI(I), 1901.
- 1601 [7] J. P. Boris. A physically motivated solution of the Alfvén problem. *NRL Memo-*
1602 *randum Report*, 2167, 1970.
- 1603 [8] A. Brekke, T. Feder, and S. Berger. Pc4 giant pulsations recorded in Tromsø,
1604 1929-1985. *Journal of Atmospheric and Terrestrial Physics*, 49(10):1027–1032,
1605 1987.

- 1606 [9] C. W. Carlson, R. F. Pfaff, and J. G. Watzin. The fast auroral Snapshot (FAST)
1607 mission. *Geophys. Res. Lett.*, 25(12):2013–2016, 1998.
- 1608 [10] A. A. Chan, M. Xia, and L. Chen. Anisotropic alfvén-balloon modes in Earth’s
1609 magnetosphere. *J. Geophys. Res. Space Physics*, 99(A9):17351–17366, 1994.
- 1610 [11] L. Chen and A. Hasegawa. A theory of long-period magnetic pulsations: 1. steady
1611 state excitation of field line resonance. *J. Geophys. Res.*, 79(7):1024–1032, 1974.
- 1612 [12] L. Chen and A. Hasegawa. Kinetic theory of geomagnetic pulsations: 1. internal
1613 excitations by energetic particles. *J. Geophys. Res.*, 96(A2):1503, 1991.
- 1614 [13] L. Chen, R. White, C. Cheng, F. Romanelli, J. Weiland, R. Hay, J. V. Dam,
1615 D. Barnes, M. Rosenbluth, and S. Tsai. Theory and simulation of fishbone-type
1616 instabilities in beam-heated tokamaks. Technical report, 1984.
- 1617 [14] C. Z. Cheng and Q. Qian. Theory of ballooning-mirror instabilities for anisotropic
1618 pressure plasmas in the magnetosphere. *J. Geophys. Res.*, 99(A6):11193, 1994.
- 1619 [15] G. Chisham and D. Orr. Statistical studies of giant pulsations (pgs): Harmonic
1620 mode. *Planetary and Space Science*, 39(7):999–1006, 1991.
- 1621 [16] W. D. Cummings, R. J. O’Sullivan, and P. J. Coleman. Standing Alfvén waves in
1622 the magnetosphere. *J. Geophys. Res.*, 74(3):778–793, 1969.
- 1623 [17] L. Dai. Collisionless magnetic reconnection via Alfvén eigenmodes. *Phys. Rev.*
1624 *Lett.*, 102(24), 2009.
- 1625 [18] L. Dai, K. Takahashi, R. Lysak, C. Wang, J. R. Wygant, C. Kletzing, J. Bonnell,
1626 C. A. Cattell, C. W. Smith, R. J. MacDowall, S. Thaller, A. Breneman, X. Tang,
1627 X. Tao, and L. Chen. Storm time occurrence and spatial distribution of Pc4
1628 poloidal ULF waves in the inner magnetosphere: A Van Allen Probes statistical
1629 study. *J. Geophys. Res. Space Physics*, 120:4748–4762, 2015.
- 1630 [19] L. Dai, K. Takahashi, J. R. Wygant, L. Chen, J. Bonnell, C. A. Cattell, S. Thaller,
1631 C. Kletzing, C. W. Smith, R. J. MacDowall, D. N. Baker, J. B. Blake, J. Fennell,
1632 S. Claudepierre, H. O. Funsten, G. D. Reeves, and H. E. Spence. Excitation of

- 1633 poloidal standing Alfvén waves through drift resonance wave-particle interaction.
1634 *Geophys. Res. Lett.*, 40:4127–4132, 2013.
- 1635 [20] A. W. Degeling, R. Rankin, and Q.-G. Zong. Modeling radiation belt electron
1636 acceleration by ULF fast mode waves, launched by solar wind dynamic pressure
1637 fluctuations. *J. Geophys. Res. Space Physics*, 119(11):8916–8928, 2014.
- 1638 [21] W. D. D’haeseleer, W. N. G. H. J. D. Callen, and J. L. Shohet. *Flux Coordinates*
1639 and *Magnetic Field Structure*. Springer-Verlag, New York, 1991.
- 1640 [22] J. W. Dungey. The attenuation of Alfvén waves. *J. Geophys. Res.*, 59(3):323–328,
1641 1954.
- 1642 [23] J. W. Dungey. Interplanetary magnetic field and the auroral zones. *Phys. Rev.*
1643 *Lett.*, 6(2):47–48, 1961.
- 1644 [24] A. Einstein. Die grundlage der allgemeinen relativitätstheorie. *Ann. Phys.*,
1645 354:769–822, 1916.
- 1646 [25] S. R. Elkington, M. K. Hudson, and A. A. Chan. Acceleration of relativistic
1647 electrons via drift-resonant interaction with toroidal-mode Pc-5 ULF oscillations.
1648 *Geophys. Res. Lett.*, 26(21):3273–3276, 1999.
- 1649 [26] M. J. Engebretson, D. L. Murr, K. N. Erickson, R. J. Strangeway, D. M. Klumpar,
1650 S. A. Fuselier, L. J. Zanetti, and T. A. Potemra. The spatial extent of radial
1651 magnetic pulsation events observed in the dayside near synchronous orbit. *J.*
1652 *Geophys. Res.*, 97(A9):13741, 1992.
- 1653 [27] M. J. Engebretson, L. J. Zanetti, T. A. Potemra, and M. H. Acuna. Harmonically
1654 structured ulf pulsations observed by the ampte cce magnetic field experiment.
1655 *Geophysical Research Letters*, 13(9):905–908, 1986.
- 1656 [28] M. J. Engebretson, L. J. Zanetti, T. A. Potemra, D. M. Klumpar, R. J. Strange-
1657 way, and M. H. Acuña. Observations of intense ULF pulsation activity near the
1658 geomagnetic equator during quiet times. *J. Geophys. Res.*, 93(A11):12795, 1988.

- 1659 [29] S. Fujita and T. Tamao. Duct propagation of hydromagnetic waves in the upper
1660 ionosphere, 1, electromagnetic field disturbances in high latitudes associated with
1661 localized incidence of a shear Alfvén wave. *J. Geophys. Res.*, 93(A12):14665, 1988.
- 1662 [30] K.-H. Glassmeier. Magnetometer array observations of a giant pulsation event. *J.*
1663 *Geophys.*, 48:127–138, 1980.
- 1664 [31] K.-H. Glassmeier. On the influence of ionospheres with non-uniform conductivity
1665 distribution on hydromagnetic waves. *J. Geophys.*, 54(2):125–137, 1984.
- 1666 [32] K.-H. Glassmeier, S. Buchert, U. Motschmann, A. Korth, and A. Pedersen. Concerning
1667 the generation of geomagnetic giant pulsations by drift-bounce resonance
1668 ring current instabilities. *Ann. Geophysicae*, 17:338–350, 1999.
- 1669 [33] C. Goertz. Kinetic alfvén waves on auroral field lines. *Planetary and Space Science*,
1670 32(11):1387–1392, 1984.
- 1671 [34] C. K. Goertz and R. W. Boswell. Magnetosphere-ionosphere coupling. *J. Geophys.*
1672 *Res.*, 84(A12):7239, 1979.
- 1673 [35] C. A. Green. Giant pulsations in the plasmasphere. *Planetary and Space Science*,
1674 33(10):1155–1168, 1985.
- 1675 [36] J. L. Green and S. Boardsen. Duration and extent of the great auroral storm of
1676 1859. *Advances in Space Research*, 38(2):130–135, 2006.
- 1677 [37] C. Greifinger and P. S. Greifinger. Theory of hydromagnetic propagation in the
1678 ionospheric waveguide. *J. Geophys. Res.*, 73(23):7473–7490, 1968.
- 1679 [38] B. C. Hall. *Lie Groups, Lie Algebras, and Representations*. Graduate Texts in
1680 Mathematics. Springer, New York, second edition, 2015.
- 1681 [39] Y. X. Hao, Q.-G. Zong, Y. F. Wang, X.-Z. Zhou, H. Zhang, S. Y. Fu, Z. Y.
1682 Pu, H. E. Spence, J. B. Blake, J. Bonnell, J. R. Wygant, and C. A. Kletzing.
1683 Interactions of energetic electrons with ULF waves triggered by interplanetary
1684 shock: Van allen probes observations in the magnetotail. *J. Geophys. Res. Space*
1685 *Physics*, 119(10):8262–8273, 2014.

- 1686 [40] L. Harang. *Pulsations in the terrestrial magnetic records at high latitude stations.*
1687 Grondahl, 1942.
- 1688 [41] O. Hillebrand, J. Muench, and R. L. McPherron. Ground-satellite correlative
1689 study of a giant pulsation event. *Journal of Geophysics Zeitschrift Geophysik*,
1690 51:129–140, 1982.
- 1691 [42] W. J. Hughes. The effect of the atmosphere and ionosphere on long period mag-
1692 netospheric micropulsations. *Planet. Space Sci.*, 22:1157–1172, 1974.
- 1693 [43] W. J. Hughes. Magnetospheric ULF waves: A tutorial with a historical perspec-
1694 tive. In M. J. Engebretson, K. Takahashi, and M. Scholer, editors, *Solar Wind*
1695 *Sources of Magnetospheric Ultra-Low-Frequency Waves*, volume 81 of *Geophys.*
1696 *Monogr.*, pages 1–12. American Geophysical Union, Washington, DC, 1994.
- 1697 [44] W. J. Hughes and D. J. Southwood. The screening of micropulsation signals by
1698 the atmosphere and ionosphere. *J. Geophys. Res.*, 81(19):3234–3240, 1976.
- 1699 [45] W. J. Hughes, D. J. Southwood, B. Mauk, R. L. McPherron, and J. N. Barfield.
1700 Alfvén waves generated by an inverted plasma energy distribution. *Nature*,
1701 275(5675):43–45, 1978.
- 1702 [46] J. A. Jacobs, Y. Kato, S. Matsushita, and V. A. Troitskaya. Classification of
1703 geomagnetic micropulsations. *J. Geophys. Res.*, 69(1):180–181, 1964.
- 1704 [47] T. Karlsson and G. T. Marklund. A statistical study of intense low-altitude electric
1705 fields observed by freja. *Geophys. Res. Lett.*, 23(9):1005–1008, 1996.
- 1706 [48] Y. Kato and T. Tsutomu. Hydromagnetic oscillations in a conducting medium
1707 with hall conduct-ivity under the uniform magnetic field. *Science reports of the*
1708 *Tohoku University. Ser. 5, Geophysics*, 7(3):147–164, 1956.
- 1709 [49] M. C. Kelley. *The Earth’s Ionosphere*. Academic Press, San Diego, second edition,
1710 1989.
- 1711 [50] R. L. Kessel. Solar wind excitation of pc5 fluctuations in the magnetosphere and
1712 on the ground. *J. Geophys. Res.*, 113(A4), 2008.

- 1713 [51] D. Y. Klimushkin, P. N. Mager, and K.-H. Glassmeier. Toroidal and poloidal
1714 Alfvén waves with arbitrary azimuthal wavenumbers in a finite pressure plasma
1715 in the earth's magnetosphere. *Annales Geophysicae*, 22(1):267–287, 2004.
- 1716 [52] S. Knight. Parallel electric fields. *Planetary and Space Science*, 21:741–750, 1973.
- 1717 [53] S. Kokubun. Observations of Pc pulsations in the magnetosphere: Satellite-ground
1718 correlation. *J. Geomagn. Geoelec*, 32(Supplement2):SII17–SII39, 1980.
- 1719 [54] S. Kokubun, K. N. Erickson, T. A. Fritz, and R. L. McPherron. Local time asym-
1720 metry of Pc 4-5 pulsations and associated particle modulations at synchronous
1721 orbit. *J. Geophys. Res.*, 94(A6):6607–6625, 1989.
- 1722 [55] D.-H. Lee and K. Kim. Compressional MHD waves in the magnetosphere: A new
1723 approach. *J. Geophys. Res.*, 104(A6):12379–12385, 1999.
- 1724 [56] A. S. Leonovich and V. A. Mazur. Structure of magnetosonic eigenoscillations of
1725 an axisymmetric magnetosphere. *J. Geophys. Res.*, 105(A12):27707–27715, 2000.
- 1726 [57] W. Liu, J. B. Cao, X. Li, T. E. Sarris, Q.-G. Zong, M. Hartinger, K. Takahashi,
1727 H. Zhang, Q. Q. Shi, and V. Angelopoulos. Poloidal ULF wave observed in the
1728 plasmasphere boundary layer. *J. Geophys. Res. Space Physics*, 118(7):4298–4307,
1729 2013.
- 1730 [58] W. Liu, T. E. Sarris, X. Li, S. R. Elkington, R. Ergun, V. Angelopoulos, J. Bonnell,
1731 and K. H. Glassmeier. Electric and magnetic field observations of Pc4 and Pc5
1732 pulsations in the inner magnetosphere: A statistical study. *J. Geophys. Res.*,
1733 114(A12), 2009.
- 1734 [59] W. Liu, T. E. Sarris, X. Li, Q.-G. Zong, R. Ergun, V. Angelopoulos, and K. H.
1735 Glassmeier. Spatial structure and temporal evolution of a dayside poloidal ULF
1736 wave event. *Geophys. Res. Lett.*, 38(19), 2011.
- 1737 [60] R. L. Lysak. Magnetosphere-ionosphere coupling by Alfvén waves at midlatitudes.
1738 *J. Geophys. Res.*, 109, 2004.
- 1739 [61] R. L. Lysak and D. hun Lee. Response of the dipole magnetosphere to pressure
1740 pulses. *Geophys. Res. Lett.*, 19(9):937–940, 1992.

- 1741 [62] R. L. Lysak and Y. Song. A three-dimensional model of the propagation of Alfvén
1742 waves through the auroral ionosphere: first results. *Adv. Space Res.*, 28:813–822,
1743 2001.
- 1744 [63] R. L. Lysak and Y. Song. Nonlocal kinetic theory of alfvn waves on dipolar field
1745 lines. *Journal of Geophysical Research: Space Physics*, 108(A8), 2003. 1327.
- 1746 [64] R. L. Lysak, C. L. Waters, and M. D. Sciffer. Modeling of the ionospheric Alfvén
1747 resonator in dipolar geometry. *J. Geophys. Res. Space Physics*, 118, 2013.
- 1748 [65] P. N. Mager and D. Y. Klimushkin. Giant pulsations as modes of a transverse
1749 Alfvénic resonator on the plasmapause. *Earth, Planets and Space*, 65(5):397–409,
1750 2013.
- 1751 [66] I. R. Mann, E. A. Lee, S. G. Claudepierre, J. F. Fennell, A. Degeling, I. J. Rae,
1752 D. N. Baker, G. D. Reeves, H. E. Spence, L. G. Ozeke, R. Rankin, D. K. Milling,
1753 A. Kale, R. H. W. Friedel, and F. Honary. Discovery of the action of a geophysical
1754 synchrotron in the Earth’s Van Allen radiation belts. *Nature Communications*, 4,
1755 2013.
- 1756 [67] I. R. Mann and A. N. Wright. Finite lifetimes of ideal poloidal Alfvén waves. *J.
1757 Geophys. Res.*, 100:23677–23686, 1995.
- 1758 [68] I. R. Mann, A. N. Wright, and A. W. Hood. Multiple-timescales analysis of ideal
1759 poloidal Alfvén waves. *J. Geophys. Res.*, 102(A2):2381–2390, 1997.
- 1760 [69] T. Maynard, N. Smith, S. Gonzalez, et al. Solar storm risk to the North American
1761 electric grid. 2013.
- 1762 [70] K. McGuire, R. Goldston, M. Bell, M. Bitter, K. Bol, K. Brau, D. Buchenauer,
1763 T. Crowley, S. Davis, F. Dylla, H. Eubank, H. Fishman, R. Fonck, B. Grek,
1764 R. Grimm, R. Hawryluk, H. Hsuan, R. Hulse, R. Izzo, R. Kaita, S. Kaye, H. Kugel,
1765 D. Johnson, J. Manickam, D. Manos, D. Mansfield, E. Mazzucato, R. McCann,
1766 D. McCune, D. Monticello, R. Motley, D. Mueller, K. Oasa, M. Okabayashi,
1767 K. Owens, W. Park, M. Reusch, N. Sauthoff, G. Schmidt, S. Sesnic, J. Strachan,
1768 C. Surko, R. Slusher, H. Takahashi, F. Tenney, P. Thomas, H. Towner, J. Valley,

- 1769 and R. White. Study of high-beta magnetohydrodynamic modes and fast-ion
1770 losses in PDX. *Phys. Rev. Lett.*, 50(12):891–895, 1983.
- 1771 [71] R. L. McPherron. The role of substorms in the generation of magnetic storms.
1772 *Washington DC American Geophysical Union Geophysical Monograph Series*,
1773 98:131–147, 1997.
- 1774 [72] R. L. McPherron, G. K. Parks, D. S. Colburn, and M. D. Montgomery. Satellite
1775 studies of magnetospheric substorms on august 15, 1968: 2. solar wind and outer
1776 magnetosphere. *J. Geophys. Res.*, 78(16):3054–3061, 1973.
- 1777 [73] T. Motoba, K. Takahashi, J. V. Rodriguez, and C. T. Russell. Giant pulsations on
1778 the afternoonside: Geostationary satellite and ground observations. *J. Geophys.*
1779 *Res. Space Physics*, 120:8350–8367, 2015.
- 1780 [74] NASA. Coordinated data analysis (workshop) web.
- 1781 [75] NASA. Near miss: The solar superstorm of july 2012.
- 1782 [76] M. Nicolet. The collision frequency of electrons in the ionosphere. *Journal of*
1783 *Atmospheric and Terrestrial Physics*, 3(4):200–211, 1953.
- 1784 [77] L. G. Ozeke and I. R. Mann. Energization of radiation belt electrons by ring
1785 current ion driven ULF waves. *J. Geophys. Res.*, 113(A2), 2008.
- 1786 [78] E. M. Poulter, W. Allan, E. Nielsen, and K.-H. Glassmeier. Stare radar observa-
1787 tions of a PG pulsation. *J. Geophys. Res.*, 88(A7):5668, 1983.
- 1788 [79] J. A. Proehl, W. Lotko, I. Kouznetsov, and S. D. Geimer. Ultralow-frequency
1789 magnetohydrodynamics in boundary-constrained geomagnetic flux coordinates.
1790 *J. Geophys. Res.*, 107(A9):1225, 2002.
- 1791 [80] H. R. Radoski. A note on oscillating field lines. *J. Geophys. Res.*, 72(1), 1967.
- 1792 [81] H. R. Radoski. A theory of latitude dependent geomagnetic micropulsations: The
1793 asymptotic fields. *J. Geophys. Res.*, 79, 1974.

- 1794 [82] R. Rankin, J. C. Samson, and V. T. Tikhonchuk. Parallel electric fields in dis-
1795 persive shear alfvén waves in the dipolar magnetosphere. *Geophys. Res. Lett.*,
1796 26(24):3601–3604, 1999.
- 1797 [83] B. Rolf. Giant micropulsations at abisko. *J. Geophys. Res.*, 36(1):9, 1931.
- 1798 [84] G. Rostoker, H.-L. Lam, and J. V. Olson. PC 4 giant pulsations in the morning
1799 sector. *J. Geophys. Res.*, 84(A9):5153, 1979.
- 1800 [85] J. C. Samson, L. L. Cogger, and Q. Pao. Observations of field line resonances,
1801 auroral arcs, and auroral vortex structures. *J. Geophys. Res.*, 101(A8):17373–
1802 17383, 1996.
- 1803 [86] H. J. Singer, W. J. Hughes, and C. T. Russell. Standing hydromagnetic waves
1804 observed by ISEE 1 and 2: Radial extent and harmonic. *J. Geophys. Res.*,
1805 87(A5):3519, 1982.
- 1806 [87] D. J. Southwood. Some features of field line resonances in the magnetosphere.
1807 *Planetary and Space Science*, 22(3):483–491, 1974.
- 1808 [88] D. J. Southwood. A general approach to low-frequency instability in the ring
1809 current plasma. *J. Geophys. Res.*, 81(19):3340–3348, 1976.
- 1810 [89] J. Stratton and N. J. Fox. Radiation belt storm probes (RBSP) mission overview.
1811 In *2012 IEEE Aerospace Conference*. Institute of Electrical & Electronics Engi-
1812 neers (IEEE), 2012.
- 1813 [90] E. Sucksdorff. Giant pulsations recorded at sodankyl during 19141938. *Terrestrial
1814 Magnetism and Atmospheric Electricity*, 44(2):157–170, 1939.
- 1815 [91] K. Takahashi, J. Bonnell, K.-H. Glassmeier, V. Angelopoulos, H. J. Singer, P. J.
1816 Chi, R. E. Denton, Y. Nishimura, D.-H. Lee, M. Nosé, and W. Liu. Multipoint
1817 observation of fast mode waves trapped in the dayside plasmasphere. *J. Geophys.
1818 Res.*, 115(A12), 2010.
- 1819 [92] K. Takahashi, K.-H. Glassmeier, V. Angelopoulos, J. Bonnell, Y. Nishimura, H. J.
1820 Singer, and C. T. Russell. Multisatellite observations of a giant pulsation event.
1821 *J. Geophys. Res.*, 116:A11223, 2011.

- 1822 [93] K. Takahashi, M. D. Hartinger, V. Angelopoulos, K.-H. Glassmeier, and H. J.
1823 Singer. Multispacecraft observations of fundamental poloidal waves without
1824 ground magnetic signatures. *J. Geophys. Res. Space Physics*, 118:4319–4334, 2013.
- 1825 [94] K. Takahashi, R. W. McEntire, A. T. Y. Lui, and T. A. Potemra. Ion flux oscillations
1826 associated with a radially polarized transverse Pc 5 magnetic pulsation. *J.
1827 Geophys. Res.*, 95(A4):3717, 1990.
- 1828 [95] K. Takahashi and R. L. McPherron. Standing hydromagnetic oscillations in the
1829 magnetosphere. *Planetary and Space Science*, 32:1343–1359, 1984.
- 1830 [96] K. Takahashi, N. Sato, J. Warnecke, H. Lühr, H. E. Spence, and Y. Tonegawa.
1831 On the standing wave mode of giant pulsations. *J. Geophys. Res. Space Physics*,
1832 97(A7):10717–10732, 1992.
- 1833 [97] B. J. Thompson and R. L. Lysak. Electron acceleration by inertial alfvén waves.
1834 *J. Geophys. Res.*, 101(A3):5359–5369, 1996.
- 1835 [98] V. T. Tikhonchuk and R. Rankin. Electron kinetic effects in standing shear alfvén
1836 waves in the dipolar magnetosphere. *Physics of Plasmas*, 7(6):2630, 2000.
- 1837 [99] B. T. Tsurutani, W. D. Gonzalez, G. S. Lakhina, and S. Alex. The extreme
1838 magnetic storm of 12 september 1859. *Journal of Geophysical Research: Space
1839 Physics*, 108(A7), 2003. 1268.
- 1840 [100] A. Y. Ukhorskiy. Impact of toroidal ULF waves on the outer radiation belt elec-
1841 trons. *J. Geophys. Res.*, 110(A10), 2005.
- 1842 [101] J. Veldkamp. A giant geomagnetic pulsation. *Journal of Atmospheric and Ter-
1843 restrial Physics*, 17(4):320–324, 1960.
- 1844 [102] J. A. Wanliss and K. M. Showalter. High-resolution global storm index: Dst versus
1845 sym-h. *Journal of Geophysical Research: Space Physics*, 111(A2):n/a–n/a, 2006.
1846 A02202.
- 1847 [103] C. L. Waters, R. L. Lysak, and M. D. Sciffer. On the coupling of fast and shear
1848 Alfvén wave modes by the ionospheric Hall conductance. *Earth Planets Space*,
1849 65:385–396, 2013.

- 1850 [104] C. L. Waters and M. D. Sciffer. Field line resonant frequencies and ionospheric
1851 conductance: Results from a 2-d MHD model. *J. Geophys. Res.*, 113(A5), 2008.
- 1852 [105] D. M. Wright and T. K. Yeoman. High-latitude HF doppler observations of ULF
1853 waves: 2. waves with small spatial scale sizes. *Ann. Geophys.*, 17(7):868–876,
1854 1999.
- 1855 [106] J. R. Wygant, J. W. Bonnell, K. Goetz, R. E. Ergun, F. S. Mozer, S. D. Bale,
1856 M. Ludlam, P. Turin, P. R. Harvey, R. Hochmann, K. Harps, G. Dalton, J. Mc-
1857 Cauley, W. Rachelson, D. Gordon, B. Donakowski, C. Shultz, C. Smith, M. Diaz-
1858 Aguado, J. Fischer, S. Heavner, P. Berg, D. M. Malsapina, M. K. Bolton, M. Hud-
1859 son, R. J. Strangeway, D. N. Baker, X. Li, J. Albert, J. C. Foster, C. C. Chaston,
1860 I. Mann, E. Donovan, C. M. Cully, C. A. Cattell, V. Krasnoselskikh, K. Kersten,
1861 A. Brenneman, and J. B. Tao. The electric field and waves instruments on the
1862 radiation belt storm probes mission. *Space Science Reviews*, 179(1):183–220, 2013.
- 1863 [107] J. R. Wygant, A. Keiling, C. A. Cattell, R. L. Lysak, M. Temerin, F. S. Mozer,
1864 C. A. Kletzing, J. D. Scudder, V. Streltsov, W. Lotko, and C. T. Russell. Evidence
1865 for kinetic alfvn waves and parallel electron energization at 46 re altitudes in the
1866 plasma sheet boundary layer. *Journal of Geophysical Research: Space Physics*,
1867 107(A8):SMP 24–1–SMP 24–15, 2002.
- 1868 [108] K. Yee. Numerical solution of initial boundary value problems involving maxwell's
1869 equations in isotropic media. *IEEE Trans. Antennas Propagat.*, 14(3), 1966.
- 1870 [109] T. K. Yeoman and D. M. Wright. ULF waves with drift resonance and drift-bounce
1871 resonance energy sources as observed in artificially-induced HF radar backscatter.
1872 *Ann. Geophys.*, 19(2):159–170, 2001.
- 1873 [110] Q.-G. Zong, X.-Z. Zhou, X. Li, P. Song, S. Y. Fu, D. N. Baker, Z. Y. Pu, T. A.
1874 Fritz, P. Daly, A. Balogh, and H. Réme. Ultralow frequency modulation of ener-
1875 getic particles in the dayside magnetosphere. *Geophys. Res. Lett.*, 34(12), 2007.
- 1876 [111] Q.-G. Zong, X.-Z. Zhou, Y. F. Wang, X. Li, P. Song, D. N. Baker, T. A. Fritz,
1877 P. W. Daly, M. Dunlop, and A. Pedersen. Energetic electron response to ULF

1878 waves induced by interplanetary shocks in the outer radiation belt. *J. Geophys.*
1879 *Res.*, 114(A10), 2009.